

LITHOS

New evidence for Late Cretaceous plume-related seamounts in the Middle East sector of the Neo-Tethys: Constraints from geochemistry, petrology, and mineral chemistry of the magmatic rocks from the western Durkan Complex (Makran Accretionary Prism, SE Iran)

--Manuscript Draft--

Manuscript Number:	LITHOS9752R2
Article Type:	Regular Article
Keywords:	ophiolite; Petrology; Clinopyroxene chemistry; Seamount; Makran Accretionary Prism; Iran
Corresponding Author:	Emilio Saccani Dipartimento di Fisica e Scienze della Terra Ferrara, ITALY
First Author:	Edoardo Barbero
Order of Authors:	Edoardo Barbero Federica Zaccarini Morteza Delavari Asghar Dolati Emilio Saccani Michele Marroni Luca Pandolfi
Abstract:	<p>The Durkan Complex in the Makran Accretionary Prism (SE Iran) has been interpreted either as a continental margin succession or a Late Cretaceous tectonically disrupted seamount chain. New whole rock and clinopyroxene chemical data for basaltic and metabasaltic rocks of the Durkan Complex allow us to distinguish two main rock groups: a) rocks showing transitional chemical affinity (Group 1) and compositions resembling those of plume-type mid-oceanic ridge basalts; b) rocks with within-plate oceanic island basalt (OIB) compositions showing a clear alkaline affinity (Group 2). Based on whole rock REE contents and clinopyroxene chemistry, alkaline rocks can be further subdivided in two sub-groups, namely, the Group 2a and 2b. Compared to Group 2a, Group 2b rocks show a more pronounced alkaline nature marked by higher whole rock La/Yb and Sm/Dy ratios and higher TiO₂ and Na₂O contents in clinopyroxenes. Trace element and REE petrogenetic models show that the Durkan basaltic rocks were generated from the partial melting of depleted sub-oceanic mantle source that was metasomatized by OIB-type chemical components in a within-plate oceanic setting. The chemical differences in the three rock groups are related to different combinations of partial melting degree, depths of melting, and various extent of enrichment of the mantle sources by OIB-type chemical components, which are related, in turn, to a Late Cretaceous mantle plume activity in the northern Neo-Tethys realm. We suggest that the Durkan Complex formed in a seamount setting and that its different volcano-sedimentary successions record different stages of seamount formation.</p>
Suggested Reviewers:	<p>Carla B. Dimalanta University of the Philippines Diliman cbdimalanta@up.edu.ph Excellent expertise on ophiolites, particularly on ophiolite petrology and tectonics</p> <p>Okay Çimen Munzur University: Munzur Universitesi okaycimen@munzur.edu.tr Excellent expertise on petrology and geochemistry of ophiolitic volcanic rocks, as well as very good knowledge of the geodynamics of the Neo-Tethys in the Middle East.</p> <p>Chakravadhanula Manikyamba</p>

	<p>Professor, National Geophysical Research Institute CSIR cmaningri@gmail.com Excellent expertise on the geochemistry of ophiolitic volcanic rocks, as well as on the geology of the Alpine-Himalayan belts from Meddle East to Pakistan and Tibet</p> <p>Sasan Bagheri University of Sistan and Baluchestan sasan@hamoon.usb.ac.ir Excellent expertise on the geology, petrology, and tectonics of Iranian ophiolites, as well as on Mesozoic-Cenozoic geodynamics of the Neo-Tethys Alternative e-mail: sasan_bagheri@yahoo.com</p>
Opposed Reviewers:	<p>Jean-Pierre Burg ETH-Zürich jean-pierre.burg@erdw.ethz.ch Potential conflict of interest in our research in the Makran</p>

New evidence for Late Cretaceous plume-related seamounts in the Middle East sector of the Neo-Tethys: Constraints from geochemistry, petrology, and mineral chemistry of the magmatic rocks from the western Durkan Complex (Makran Accretionary Prism, SE Iran)

Edoardo Barbero¹, Federica Zaccarini², Morteza Delavari³, Asghar Dolati³, Emilio Saccani¹, Michele Marroni^{4,5}, Luca Pandolfi^{4,5}

1 Dipartimento di Fisica e Scienze della Terra, Università di Ferrara, 44123 Ferrara, Italy;
brbdrd@unife.it (E.B.); sac@unife.it (E.S.)

2 Department of Applied Geological Sciences and Geophysics, University of Leoben, 8700 Leoben, Austria; federica.zaccarini@unileoben.ac.at

3 Faculty of Earth Sciences, Kharazmi University, Tehran 15719-19911, Iran;
delavari@khu.ac.ir (M.D.); dolati@khu.ac.ir (A.D.)

4 Dipartimento di Scienze della Terra, Università di Pisa, 56126 Pisa, Italy;
luca.pandolfi@unipi.it (L.P.); michele.marroni@unipi.it (M.M.)

5 Istituto di Geoscienze e Georisorse, Consiglio Nazionale delle Ricerche (CNR), 56124 Pisa, Italy

Corresponding author:

Dr. Emilio Saccani

E-mail: sac@unife.it

Phone: +39 0532974719



**Università
degli Studi
di Ferrara**

**Dipartimento
di Fisica
e Scienze della Terra**

Via Saragat 1 •
I-44122 Ferrara
Italy

<http://fst.unife.it>

EMILIO SACCANI

Phone. +39 0532 974719

E -mail: sac@unife.it

Ms. Ref. No.: LITHOS9752_R1

Title: New evidence for Late Cretaceous plume-related seamounts in the Middle East sector of the Neo-Tethys: Constraints from geochemistry, petrology, and mineral chemistry of the magmatic rocks from the western Durkan Complex (Makran Accretionary Prism, SE Iran)

Dear Editor,

Thank you very much for your editorial help. We are very sorry for having left several silly grammatical issues in the revised text. We are submitting herein our revised manuscript. We have fixed all the issues you highlighted.

As usual, we upload two versions of the revised manuscript. One version is with changes marked (annotated) in which you can promptly see the changes we made. The other one is with no changes marked (only revised text).

We thank you again for your editorial help and consideration, and look forward to hearing from you soon.

Yours sincerely,

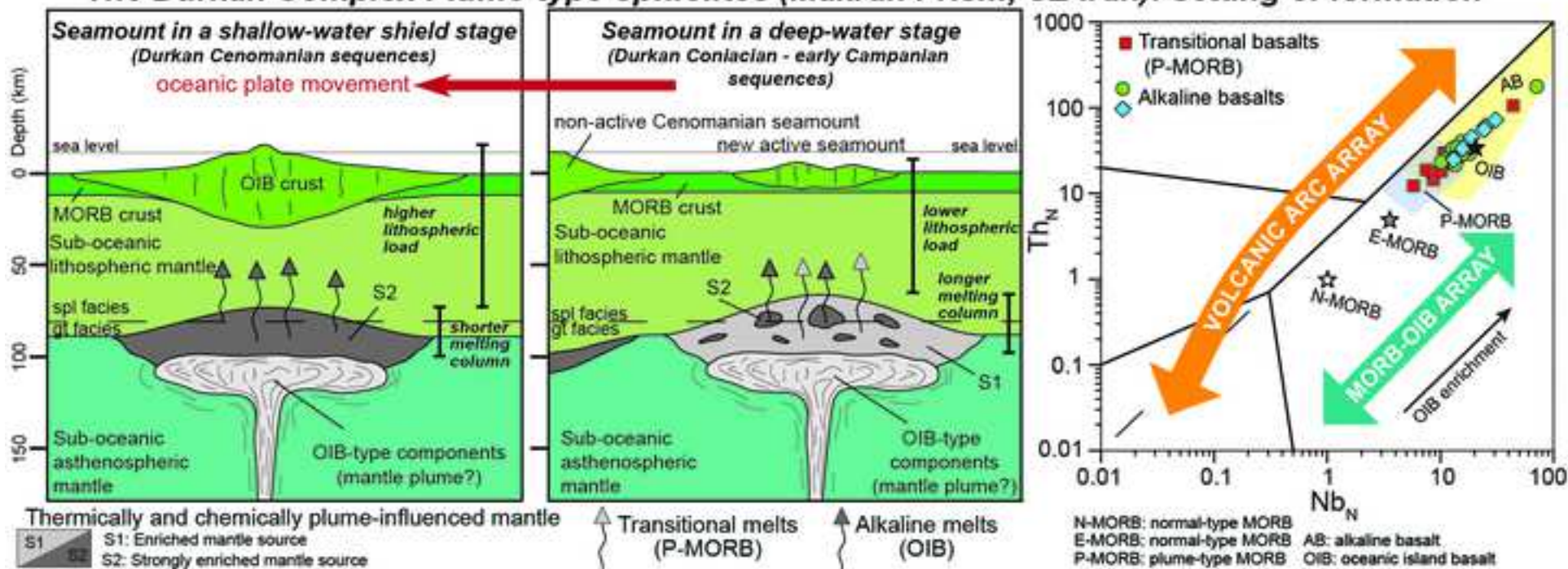
Emilio Saccani

On behalf of the co-authors

Abstract

The Durkan Complex in the Makran Accretionary Prism (SE Iran) has been interpreted either as a continental margin succession or a Late Cretaceous tectonically disrupted seamount chain. New whole rock and clinopyroxene chemical data for basaltic and metabasaltic rocks of the Durkan Complex allow us to distinguish two main rock groups: a) rocks showing transitional chemical affinity (Group 1) and compositions resembling those of plume-type mid-oceanic ridge basalts; b) rocks with within-plate oceanic island basalt (OIB) compositions showing a clear alkaline affinity (Group 2). Based on whole rock REE contents and clinopyroxene chemistry, alkaline rocks can be further subdivided in two sub-groups, namely, the Group 2a and 2b. Compared to Group 2a, Group 2b rocks show a more pronounced alkaline nature marked by higher whole rock La/Yb and Sm/Dy ratios and higher TiO₂ and Na₂O contents in clinopyroxenes. Trace element and REE petrogenetic models show that the Durkan basaltic rocks were generated from the partial melting of depleted sub-oceanic mantle source that was metasomatized by OIB-type chemical components in a within-plate oceanic setting. The chemical differences in the three rock groups are related to different combinations of partial melting degree, depths of melting, and various extent of enrichment of the mantle sources by OIB-type chemical components, which are related, in turn, to a Late Cretaceous mantle plume activity in the northern Neo-Tethys realm. We suggest that the Durkan Complex formed in a seamount setting and that its different volcano-sedimentary successions record different stages of seamount formation.

The Durkan Complex Plume-type ophiolites (Makran Prism, SE Iran): setting of formation



Research Highlights

- The western Durkan Complex consists of different volcano-sedimentary successions
- Basaltic rocks are largely prevailing though trachytes and rhyolites locally occur
- Volcanic rocks show transitional (P-MORB) and alkaline (OIB) geochemistry
- The Durkan volcanic rocks were erupted in different stages of seamounts life
- The Durkan Complex records the existence of seamounts in the Cretaceous Neo-Tethys

[Click here to view linked References](#)

1 New evidence for Late Cretaceous plume-related seamounts in the Middle East sector
2 of the Neo-Tethys: Constraints from geochemistry, petrology, and mineral chemistry of the
3 magmatic rocks from the western Durkan Complex (Makran Accretionary Prism, SE Iran)

4

5

6

7 Edoardo Barbero¹, Federica Zaccarini², Morteza Delavari³, Asghar Dolati³, Emilio
8 Saccani¹, Michele Marroni^{4,5}, Luca Pandolfi^{4,5}

9

10

11 1 Dipartimento di Fisica e Scienze della Terra, Università di Ferrara, 44123 Ferrara,
12 Italy; brbrdrd@unife.it (E.B.); sac@unife.it (E.S.)

13 2 Department of Applied Geological Sciences and Geophysics, University of Leoben,
14 8700 Leoben, Austria; federica.zaccarini@unileoben.ac.at

15 3 Faculty of Earth Sciences, Kharazmi University, Tehran 15719-19911, Iran;
16 delavari@khu.ac.ir (M.D.); dolati@khu.ac.ir (A.D.)

17 4 Dipartimento di Scienze della Terra, Università di Pisa, 56126 Pisa, Italy;
18 luca.pandolfi@unipi.it (L.P.); michele.marroni@unipi.it (M.M.)

19 5 Istituto di Geoscienze e Georisorse, Consiglio Nazionale delle Ricerche (CNR),
20 56124 Pisa, Italy

21

22

23 * Corresponding author: Emilio Saccani (sac@unife.it)

24

25

26 Abstract

27 The Durkan Complex in the Makran Accretionary Prism (SE Iran) has been interpreted
28 either as a continental margin succession or a Late Cretaceous tectonically disrupted
29 seamount chain. New whole rock and clinopyroxene chemical data for basaltic and
30 metabasaltic rocks of the Durkan Complex allow us to distinguish two main rock groups:
31 a) rocks showing transitional chemical affinity (Group 1) and compositions resembling
32 those of plume-type mid-oceanic ridge basalts; b) rocks with within-plate oceanic island
33 basalt (OIB) compositions showing a clear alkaline affinity (Group 2). Based on whole
34 rock REE contents and clinopyroxene chemistry, alkaline rocks can be further subdivided
35 in two sub-groups, namely, the Group 2a and 2b. Compared to Group 2a, Group 2b rocks
36 show a more pronounced alkaline nature marked by higher whole rock La/Yb and Sm/Dy
37 ratios and higher TiO₂ and Na₂O contents in clinopyroxenes. Trace element and REE
38 petrogenetic models show that the Durkan basaltic rocks were generated from the partial
39 melting of depleted sub-oceanic mantle source that was metasomatized by OIB-type
40 chemical components in a within-plate oceanic setting. The chemical differences in the
41 three rock groups are related to different combinations of partial melting degree, depths of
42 melting, and various extent of enrichment of the mantle sources by OIB-type chemical
43 components, which are related, in turn, to a Late Cretaceous mantle plume activity in the
44 northern Neo-Tethys realm. We suggest that the Durkan Complex formed in a seamount
45 setting and that its different volcano-sedimentary successions record different stages of
46 seamount formation.

47

48 **Keywords:** Ophiolite, Geochemistry, Petrology, Clinopyroxene chemistry, Alkaline
49 basalt, Seamount, Makran Accretionary Prism, Iran

50

51

52 1. Introduction

53

54 Ophiolitic basaltic and metabasaltic rocks are widespread within collisional-type and
55 accretionary-type orogenic belts and are of particular importance, as their petrological
56 features are sensitive to different geodynamic settings of formation. Different tectonic
57 environments, such as mid-oceanic ridge, within-plate oceanic island, convergent and rifted
58 margins, are indeed characterized by the occurrence of chemically distinctive types of
59 basaltic rocks (Pearce, 1996; Dilek and Furnes, 2011; Saccani, 2015; Safonova et al., 2016).
60 Among them, basaltic rocks with oceanic island basalt (OIB) chemical affinity are of
61 particular interest as they may represent remnants of deformed oceanic seamounts (Yang et
62 al., 2015, 2019; Wan et al., 2020). Seamounts are largely subducted and their remnants in
63 the accretionary and collisional belts are represented only by blocks in ophiolitic mélanges
64 (e.g., Yang et al., 2019; Safonova et al., 2016) or as coherent slices underplated at different
65 depths (e.g., Isozaki et al., 1990; Bonnet et al., 2020). In addition, recognizing basalts with
66 OIB affinity within accretionary and collisional belts is particularly important as they likely
67 represent the only elements for reconstructing periods of mantle plume activity during Earth
68 history (Safonova and Santosh, 2014; Wan et al., 2020). It follows that detailed petrological
69 studies of basaltic rocks within the accretionary and collisional belts are fundamental for
70 constraining their tectono-magmatic settings of formation and, consequently, for
71 reconstructing the progressive geodynamic history of the paleo-oceanic basins and their
72 related continental margins (Robertson, 2007; Hässig et al., 2013; Safonova, 2017; Saccani
73 et al., 2018; Rolland et al., 2020).

74 The Makran Accretionary Prism (hereafter, simply Makran) in SE Iran and SW
75 Pakistan (Figs. 1a, b) is related to the long-lived geodynamic evolution of the Neo-Tethys
76 Ocean and its northern continental margin, represented by the Lut and Afghan blocks

77 (McCall and Kidd, 1982; Burg et al., 2008; 2013; Burg, 2018; Saccani et al., 2018; Monsef
78 et al., 2018; Barbero et al., 2020a). The Makran consists of several tectono-stratigraphic
79 domains (Fig. 1b) that have been deformed and incorporated in the accretionary prism,
80 starting from the Cretaceous (e.g., Platt et al., 1985; Dolati and Burg., 2013; Burg, 2018;
81 Saccani et al., 2018; Barbero et al., 2020a, b). Among these, the North Makran domain
82 records the pre-Eocene deformation history of the accretionary wedge. It consists of several
83 tectonic units (Fig. 1c) that, in turn, represent distinct tectonic domains, including the Neo-
84 Tethys oceanic lithosphere, seamounts and/or oceanic plateau, as well as arc-forearc-trench
85 domains. The North Makran also includes tectonic units derived from an exotic
86 microcontinental block and its sedimentary cover (McCall and Kidd, 1982; Dorani et al.,
87 2017; Burg, 2018; Monsef et al., 2018; Saccani et al., 2018). The Durkan Complex is one of
88 the major tectonic elements of the North Makran domain (Fig. 1c) and it was described as a
89 highly deformed complex including Early Cretaceous – early Paleocene shallow water
90 succession, abundant volcanic rocks, as well as subordinate tectonic slices of Carboniferous,
91 Permian and Jurassic shallow water sedimentary rocks and Middle - Late Jurassic granitoids
92 (McCall, 1985; Hunziker et al., 2015). It has been classically interpreted as the Permian –
93 Cretaceous disrupted sedimentary cover of the passive margin of a continental basement as
94 old as Paleozoic, whose remnants are now represented by the Bajgan Complex (McCall and
95 Kidd, 1982; McCall, 2002). The Bajgan-Durkan Complexes are collectively thought to
96 represent the remnants of a continental ribbon detached from the Eurasian margin by the
97 Late Jurassic – Early Cretaceous rifting that led to the opening of the North Makran Ocean
98 (McCall and Kidd, 1982; McCall, 2002; Hunziker et al., 2015; Burg, 2018). However,
99 Barbero et al. (2021) showed that the western Durkan Complex consists of tectonic slices
100 including volcano-sedimentary sequences, which represent remnants of a tectonically
101 disrupted Late Cretaceous seamounts chain. This interpretation, which is radically different

102 from the extant interpretation, is based on field investigations and detailed stratigraphic,
103 structural, and biochronological data, as well as preliminary petrographic and geochemical
104 data on volcanic rocks. However, a thorough geochemical and petrological investigations of
105 the volcanic rocks included in the Durkan volcano-sedimentary sequences is necessary for
106 better constraining the tectono-magmatic setting of formation of the Durkan Complex, as
107 well as its significance for the geodynamic evolution of the pre-Eocene Makran
108 Accretionary Prism. Therefore, in this paper, we present new whole-rock, as well as mineral
109 geochemical data on the volcanic and metavolcanics rocks from the Durkan Complex.
110 These data will be discussed in the context of the detailed tectono-stratigraphic results
111 presented by [Barbero et al. \(2021\)](#) with the purpose of adding the final touch to the
112 knowledge of tectono-magmatic setting of formation of this Complex. Finally, these
113 findings will then be discussed for the Late Cretaceous geodynamic evolution of the
114 northern Neo-Tethys realm.

115

116

117 2. Geological setting

118

119 *2.1. General geological setting of the Makran Accretionary Prism*

120

121 The Makran Accretionary Prism is the result of a complex Cretaceous – Present day
122 geodynamic history, which is related to the subduction of the Neo-Tethys oceanic
123 lithosphere below the southern margin of Eurasia ([McCall and Kidd, 1982](#); [Dercourt et al.,
124 1986](#); [Saccani et al., 2018](#); [Burg, 2018](#); [Monsef et al., 2018](#); [Barrier et al., 2018](#); [Barbero et
125 al., 2020a, b](#)). The Makran is an E-W trending active subduction complex, which is laterally
126 separated from the Zagros and the Himalayan collisional systems by N-S trending strike-

127 slip fault zones (Figs. 1a, b) (e.g. Dercourt et al., 1986; Kopp et al., 2000; Burg et al., 2013;
128 Mohammadi et al., 2016; Riaz et al., 2019). The present-day deformation front of the
129 Makran is located offshore in the Oman Sea (Fig. 1a). The onshore Makran is characterized
130 by the tectonic juxtaposition of several tectono-stratigraphic domains (Dolati, 2010; Burg et
131 al., 2013). In the western part of the prism these domains are from the structural top to the
132 bottom (i.e., from the north to the south): 1) the North Makran; 2) the Inner Makran; 3) the
133 Outer Makran; 4) the Coastal Makran (Fig. 1c). The Inner, Outer and Coastal Makran
134 domains represent the Eocene - present day accretionary complex and include Eocene –
135 Pleistocene mainly terrigenous sedimentary successions (e.g., Dolati, 2010; Burg et al.,
136 2013; Burg, 2018). The North Makran domain includes remnants of pre-Eocene
137 accretionary stages and consists of a tectonic stack of oceanic and continental derived units,
138 some of which showing variable degrees of metamorphic imprint (e.g., McCall and Kidd,
139 1982; Burg, 2018). These units include from north to south and from the higher to the
140 lowermost structural position (Fig. 1c): 1) the Ganj Complex; 2) the Northern Ophiolites, 3)
141 the Bajgan and Durkan Complexes, 4) the Sorkhband – Rudan tectonic slices 5) the
142 Coloured M \acute{e} lange Complex.

143 Recent studies have shown that the Ganj Complex represents fragments of a Late
144 Cretaceous volcanic arc that was likely built up close to the southern margin of the Lut
145 Block (Barbero et al., 2020a). The Northern Ophiolites (Fig. 1c) are Early to Late
146 Cretaceous in age and include the Band-e-Zeyarat/Dar Anar (Ghazi et al., 2004; Barbero et
147 al., 2020b), Remeshk-Mokhtarabad (McCall, 1985, 2002; Hunziker et al., 2015; Burg,
148 2018), and Fanuj-Maskutan (Moslempour et al., 2015) ophiolitic complexes. Their
149 magmatic rocks mostly show enriched-type mid-ocean ridge basalts (E-MORB) chemical
150 affinity for the Early Cretaceous ophiolites (Ghazi et al., 2004; Barbero et al. 2020b),
151 whereas the Late Cretaceous ophiolites show supra-subduction zone chemical affinity

152 (Burg, 2018; Monsef et al., 2019, Sepidbar et al., 2020). These ophiolitic complexes were
153 collectively interpreted as the remnants of the oceanic lithosphere of the North Makran
154 Ocean, which is thought to represent an oceanic basin that existed during Late Jurassic –
155 Early Cretaceous at the southern margin of the Central Iran continental plate. The Bajgan
156 and Durkan Complexes (Figs.1c, 2) have classically been interpreted as remnants of a
157 microcontinental block, which was separated from the Lut Block in the Late Jurassic - Early
158 Cretaceous. The Bajgan Complex is made up of an assemblage of metamorphic rocks that
159 include schists, paragneisses, amphibolites, marbles, as well as basic and acidic meta-
160 intrusive rocks (McCall, 1985; McCall, 2002; Dorani et al., 2017). The P-T condition of the
161 metamorphism and its age are poorly constrained. However, moderately high pressure and
162 high temperature conditions have been suggested (McCall, 1985; Dorani et al., 2017). The
163 Durkan Complex (Figs.1c, 2) consists of a highly deformed and locally slightly
164 metamorphosed (i.e., up to sub-greenschist facies) complex including: 1) Late Cretaceous
165 shallow-water limestones and thick sequences of alternating limestones, sandstones, shales,
166 cherts and volcanic rocks (Barbero et al., 2021), 2) very minor tectonic slices of
167 Carboniferous, Permian and Jurassic shelf carbonate rocks, as well as marbles and schists
168 (McCall, 1985, 2002; Hunziker et al., 2015); 3) Early – Late Jurassic different types of
169 granitoids intruded into Jurassic shelf limestones in the eastern part of the Makran
170 (Hunziker et al., 2015; Burg, 2018). This Complex has been considered as the original
171 sedimentary cover of the Bajgan metamorphic Complex (McCall, 1985, 2002). However,
172 based on recent multidisciplinary investigation on its western part, Barbero et al. (2021)
173 showed that this Complex represents a tectonically disrupted Late Cretaceous seamount
174 chain incorporated as tectonic slices into the North Makran accretionary prism.

175 The Deyader Complex crops out in the eastern sector of the North Makran (Fig. 1c). It
176 represents a meta-ophiolitic complex affected by high pressure-low temperature (HP-LT)

177 metamorphism (McCall, 1985; Hunziker et al., 2015; Omrani et al., 2017). The Sorkhband
178 and Rudan ophiolites crop out in the western part of the North Makran within the shear zone
179 between the Coloured Mélange and the Bajgan Complex (McCall, 2002; Delavari et al.,
180 2016). The Coloured Mélange Complex is composed of metric- to decametric-thick tectonic
181 slices and was formed in Cretaceous-Paleocene times (McCall and Kidd, 1982; McCall,
182 2002; Saccani et al., 2018; Burg, 2018; Esmaeili et al., 2019). Saccani et al. (2018) showed
183 that the Coloured Mélange Complex incorporates a great variety of volcanic and meta-
184 volcanic rock-types formed in both the subducting oceanic plate (i.e., oceanic plateau
185 basalts, normal mid-ocean ridge basalts, and alkaline basalts) and the upper plate (i.e. Early
186 - Late Cretaceous island arc tholeiites and calc-alkaline basalts).

187

188 *2.2. Stratigraphic features of the western part of the Durkan Complex*

189

190 Detailed fieldwork and stratigraphic, structural, and biostratigraphic investigations have
191 recently been carried out on the western part of the Durkan Complex (Barbero et al., 2021).
192 This work shows that this Complex (Fig. 2) consists of several tectonic slices, within
193 which different stratigraphic successions can be recognized (Fig. 3). The different slices
194 include both non-metamorphic and slightly metamorphosed successions, all characterized
195 by abundant volcanic rocks (Fig 3a). These stratigraphic successions can be reconciled to
196 three types of successions that are similar to those found at different depths of a seamount
197 setting. The characteristics of these successions, as described by Barbero et al. (2021) are
198 briefly summarized in the following sections.

199

200 *2.2.1. Type I succession: deep-water stage of seamount growth*

201

202 This succession type represents a Coniacian - Campanian pelagic sequence consisting
203 of thin-bedded red cherts and cherty limestones alternated with shales and shaly marls, as
204 well as minor volcanoclastic arenites and pillow breccias. Pillow basalts are frequently
205 interbedded within this sequence (Fig. 3a), and are characterized by low vesicularity (Fig.
206 3b). These features suggest eruption under a relatively thick water column pressure (Fig.
207 3b). This type of succession represents the remnants of a seamount in its deep-water stages
208 of formation characterized by pelagic sedimentation and volcanic activity in a deep-water
209 depositional environment.

210

211 2.2.2. Type II succession: seamount flank during shallow-water stage of a seamount
212 growth

213

214 This succession is characterized by a volcanic sequence showing stratigraphic transition
215 to a volcano-sedimentary sequence that, in turn, gradually passes upward to a pelagic and
216 hemipelagic sedimentary sequence (Fig. 3a). The volcanic sequence is made up of
217 alternating massive lava flows, pillow lavas, and volcanoclastic arenites and breccias (Fig.
218 3a). The volcano-sedimentary sequence consists of alternating volcanoclastic arenites and
219 breccias, shales and siltstones, and Cenomanian limestone, as well as minor massive lava
220 flows (Fig. 3a). Limestones show pelagic foraminifera assemblages suggesting a relatively
221 deep-water depositional setting. Accordingly, the analysis of the volume percent of vesicles
222 for the volcanic rocks suggest a relatively high eruption depth, which is however
223 significantly lower than those of the Type I succession (Fig. 3b). The pelagic and
224 hemipelagic sedimentary sequence consists of cherty limestones, shales, shaly marls, cherts,
225 and minor carbonatic breccias and volcanoclastic arenites (Fig. 3a). The stratigraphic

226 features of Type-II succession indicates a depositional setting along and at the base of a
227 seamount flank during the relatively shallow-water shield stage of growth of a seamount.

228

229 2.2.3. Type III: seamount summit during shallow-water stage of seamount growth

230

231 This stratigraphic succession is characterized by a volcanic sequence passing laterally
232 and upward to a volcano-sedimentary sequence that is, in turn, followed by a Cenomanian
233 carbonatic platform sequence and ends upward with a pelagic and hemipelagic sequence
234 (Fig. 3a). The volcanic sequence is characterized by pillow and massive lava flows
235 alternating with volcanoclastic arenites. The volcano-sedimentary sequence is composed by
236 alternating volcanic rocks, volcanoclastic arenites and breccias, shales, as well as turbidites
237 showing mixed carbonatic - volcanic composition (Fig. 3a). In addition, minor platform-
238 derived massive limestones are interbedded in the sequences, suggesting a shallow-water
239 depositional setting, as also indicated by the particularly high vesicularity of the pillow
240 lavas (Fig. 3b). The Cenomanian, shallow-water carbonatic platform sequence consists of
241 massive limestones alternating with subordinate volcanoclastic arenites but lacks of lava
242 flows (Fig. 3a). The uppermost hemipelagic and pelagic sequence marks the drowning of
243 the carbonatic platform. The stratigraphy of Type-III succession record shallow-water
244 volcanic activity associated with carbonatic platform sedimentation and it is comparable
245 with the stratigraphic successions formed in seamount summit setting during the shallow-
246 water shield stage of growth.

247

248

249 3. Petrography

250

251 The Durkan volcanic and volcano-sedimentary sequences include both volcanic
252 (prevailing) and metavolcanic (subordinate) rocks. The metavolcanic rocks underwent re-
253 crystallization under low-grade metamorphic conditions, though magmatic relicts are
254 commonly preserved in all samples. Volcanic rocks were affected by variable degrees of
255 alteration, which resulted in different extent of replacement of the primary magmatic
256 minerals. Nonetheless, their original magmatic texture is still recognizable. Fresh
257 plagioclase is very rare, and it is usually pseudomorphosed by a fine-grained assemblage of
258 albite, calcite and sericite. Similarly, olivine crystals are commonly replaced by iddingsite
259 and serpentine plus Fe-Ti oxides. Clinopyroxene crystals are present as both phenocrysts
260 and groundmass minerals. They occur either as fresh or altered crystals characterized by
261 pseudomorphic replacement by chlorite or actinolitic amphibole. Volcanic glass has been
262 generally replaced by an assemblage of chlorite and clay minerals. The studied volcanic
263 rocks are represented by basalts, ferrobasalts, and a couple of differentiated rocks (trachyte
264 and alkali-rhyolite). Four types of petrofacies have been distinguished according to
265 textures; they are: 1) aphyric type; 2) porphyritic type; 3) coarse-grained, doleritic type; 4)
266 metamorphic type. Representative microphotographs are given as [Supplementary Figure](#)
267 [S1](#), whereas the texture of each sample is given in [Table 1](#).

268 The aphyric type petrofacies includes basalts and ferrobasalts, as well as one trachyte
269 sample showing aphyric to slightly porphyritic ($PI < 10$) texture. In the slightly porphyritic
270 samples, the phenocrysts consist of plagioclase, clinopyroxene, and locally olivine. They
271 are set in a hypocrystalline groundmass showing intersertal to microcrystalline texture with
272 microlite of plagioclase, olivine, and clinopyroxene and less abundant Fe-Ti oxides,
273 surrounded by altered volcanic glass. In contrast, the trachyte sample is characterized by
274 aphyric texture, showing laths of plagioclase set in altered volcanic glass.

275 The porphyritic type petrofacies includes basalts and ferrobasalts showing porphyritic
276 and glomeroporphyritic texture with PI ranging from 15 to 60. The phenocrysts are up to 5-
277 6 mm in size and are mainly represented by clinopyroxene, minor plagioclase and Fe-Ti
278 oxides, and rare olivine. Clinopyroxene phenocrysts commonly show concentric zonation
279 and weak pleochroism from pale yellow to pale pink. The phenocrysts are set in a
280 hypohyaline groundmass showing intergranular to microcrystalline textures. Rarely,
281 intersertal texture can be observed in the groundmass. The groundmass consists of
282 clinopyroxene and plagioclase together with minor olivine and altered volcanic glass.

283 The coarse-grained doleritic type includes basalts and ferrobasalts showing
284 holocrystalline, inequigranular texture. They are characterized by euhedral plagioclase and
285 euhedral to subhedral clinopyroxene crystals, up to 5 mm in size. Locally, clinopyroxene
286 encloses plagioclase crystals, showing subophitic texture. These large clinopyroxene
287 crystals are surrounded by a fine-grained crystalline aggregate consisting of euhedral to
288 subhedral plagioclase, clinopyroxene as well as Fe-Ti oxides. In ferrobasalts, opaque
289 minerals show subhedral to anhedral morphology.

290 The slightly metamorphic type petrofacies includes metabasalts, and metaferrobasalts,
291 as well as one meta-alkali-rhyolite sample showing anastomosed foliation defined by a
292 fine-grained aggregate of chlorite, fibrous amphibole, Fe-Ti oxides, subordinate epidote, as
293 well as by the alignment of albite aggregates. In most samples, the foliation envelops
294 magmatic relicts consisting of clinopyroxene and minor plagioclase. In a few samples, the
295 metamorphic foliation is well developed and it is marked by the alternation of millimetre-
296 spaced and anastomosed domains with different mineralogical composition. In detail,
297 albite-rich domains alternate with domains showing chlorite, epidote and relicts of
298 magmatic clinopyroxene. The mineralogical paragenesis of these samples, as well as the
299 fine-grained size of the metamorphic minerals indicate very low-grade metamorphic

300 overprint, likely in the sub-greenschist-facies or the prehnite-pumpellyite metamorphic
301 conditions.

302

303

304 4. Analytical methods

305

306 Whole rock major and trace element compositions of a total of forty-three samples is
307 presented in this paper. Thirty-two samples were analysed for rock major and some trace
308 elements by X-ray fluorescence spectrometry (XRF) on pressed-powder pellets, using an
309 ARL Advant-XP automated X-ray spectrometer. The matrix correction method proposed
310 by [Lachance and Trail \(1966\)](#) was applied. Volatile contents were determined as loss on
311 ignition (L.O.I.) at 1000°C. In addition, XRF analyses of eleven samples are taken from
312 [Barbero et al. \(2021\)](#). For the discussion of the geochemical characteristics of the studied
313 rocks major element composition has been re-calculated on L.O.I.-free bases. The rare
314 earth elements (REE) and some trace elements (Rb, Sr, Zr, Y, Nb, Hf, Ta, Th, U) were
315 determined by inductively coupled plasma-mass spectrometry (ICP-MS) using a Thermo
316 Series X-I spectrometer on a total of thirty-nine selected samples. All whole-rock analyses
317 were performed at the Department of Physics and Earth Sciences of the Ferrara University;
318 results are shown in [Table 1, where new data from this paper and XRF data from Barbero](#)
319 [et al. \(2021\) are identified](#). The accuracy of the XRF and ICP-MS data were evaluated
320 using results for international standard rocks run as unknown. The detection limits for XRF
321 and ICP-MS analyses were evaluated using results from several runs of twenty-nine
322 international standards. Results are presented in [Supplementary Table S1](#).

323 The major element composition of clinopyroxene were obtained by electron
324 microprobe spectrometry using a Superprobe Jeol JXA 8200 (JEOL, Tokyo, Japan) at the

325 Eugen F. Stumpfl Laboratory at the University of Leoben, Austria, using both energy
326 dispersive spectrometry (EDS) and wave-length dispersive spectrometry (WDS) systems.
327 The electron microprobe was operated in the WDS mode during the quantitative analyses.
328 An accelerating voltage of 15 kV and beam current of 10 nA were used during the
329 analyses. The diameter of the beam was about 1 μm . Counting times were 20 s on the peak
330 and 10 s on both left and right backgrounds. Standards (element, emission line) were:
331 adularia (Al and Si, $K\alpha$), rutile (Ti, $K\alpha$), chromite (Cr, $K\alpha$), almandine (Fe, $K\alpha$), rhodonite
332 (Mn, $K\alpha$), olivine (Mg, $K\alpha$), wollastonite (Ca, $K\alpha$), albite (Na, $K\alpha$), and sanidine (K, $K\alpha$).
333 The following diffracting crystals were selected: TAP for Na, Mg, and Al; PETJ for K, Si,
334 and Ca; and LIFH for Ti, Cr, Mn and Fe. The detection limits were automatically
335 calculated by the Jeol microprobe software and they are listed in the following as ppm: Na,
336 Al, Mg, K, Ca (100), Si, Cr, Fe, Mn (150) and Ti (200). The results of microprobe analyses
337 are shown in [Table 2](#).

338

339

340 5. Whole rock geochemistry

341

342 The petrographic analysis has shown that the studied rocks have undergone secondary
343 alteration (e.g., ocean-floor hydrothermal alteration) or sub-greenschist facies
344 metamorphism; therefore, some elements may have been remobilized during these
345 processes. In fact, it is well known that large ion lithophile elements and many major
346 elements are commonly affected by alteration-induced mobilization. In addition, light REE
347 (LREE) may also have been mobilized during secondary alteration processes (e.g., [Pearce
348 and Norry, 1979](#)). In contrast, many incompatible elements (e.g., Ti, P, Zr, Y, Sc, Nb, Ta,
349 Hf, Th), middle (M) and heavy (H) REE, as well as some transition metals (e.g., Ni, Co,

350 Cr, V) are considered to be immobile during low-temperature alteration and
351 metamorphism. For these reasons, the geochemical features of the Durkan Complex
352 magmatic rocks are described using those elements considered immobile during alteration
353 processes. Rb and Ba are generally considered as mobile elements. Nonetheless, these
354 elements did not demonstrate a high degree of mobility in most samples. In fact, in these
355 samples, their contents show good correlations with immobile element contents (e.g.,
356 correlation coefficient with Rb vs. Y = 0.71). Therefore, Rb and Ba will be used, though
357 with caution.

358 The volcanic rocks of the Durkan Complex largely consist of basalts, subordinate
359 ferrobasalts and rare basaltic andesites, trachytes, and alkali rhyolites. Metabasalts and
360 metaferrobasalts though subordinate in volume are also found in all the succession types
361 (Table 1). Metavolcanic rocks will be discussed together with volcanic rocks because this
362 paper is focused on the identification of the geochemical features of the original volcanic
363 protoliths and their tectono-magmatic setting of formation, regardless of the tectono-
364 metamorphic events that affected some tectonic slices of volcanic rocks during their late
365 incorporation in the accretionary wedge. For the sake of simplicity, the prefix “meta” will
366 be hereafter omitted. Basaltic rocks show variable major and trace elements compositions
367 (Table 1), which most likely suggest that they represent melts at different stages of
368 fractionation. Based on the Nb/Y ratios (Winchester and Floyd, 1977; Pearce, 1996), we
369 can distinguish two main groups of rocks (Fig. 4). Group 1 rocks show a transitional nature
370 with Nb/Y ratios in the range 0.8-1.00, whereas Group 2 rocks show a clear alkaline
371 affinity with Nb/Y ratios >1 (1.15-3.16).

372

373 *5.1. Group 1 rocks*

374

375 This group includes basaltic, basaltic andesitic, and ferrobasaltic rocks, as well as one
376 trachyte sample. These rocks are mainly found in the Type-I succession, whereas they are
377 less abundant in the Type-II succession and completely lacking in Type-III succession
378 (Table 1). Group 1 basalts show a wide range of composition in terms of SiO₂ (43.3 – 53.3
379 wt%), MgO (4.93 – 11.9 wt%), Al₂O₃ (12.2 – 17.2 wt%), and Mg# (47.8 – 75.4),
380 suggesting that they were likely formed from melts at different degrees of fractionation.
381 The basaltic rocks are characterized by relatively high TiO₂ (1.20 – 2.29 wt%), P₂O₅ (0.23
382 – 0.51 wt%), Zr (73 – 220 ppm), Nb (13.5 – 32.6 ppm), Th (1.49 – 3.66 ppm), and Ta (0.92
383 – 2.18 ppm) contents coupled with relatively low Y contents (16.9 - 33.5 ppm).
384 Compatible elements (Cr, V, Ni, and Co) contents are variable, but generally high, as
385 expected for basaltic rocks (Table 1). The Ti/V ratios are in the range 28 – 61, which are
386 values typically observed in MORB to alkaline transitional basalts (Shervais, 1982).
387 Normal type MORB (N-MORB) normalized incompatible elements spider-diagrams
388 display regularly decreasing patterns from Th to Yb, (Fig. 5a). Yb content in basaltic
389 samples is relatively low, ranging from 0.49 to 0.82 times N-MORB (Sun and
390 McDounough, 1989) abundance (Fig. 5a). Group 1 rocks show mild LREE enrichment
391 with respect to HREE, as well as moderate depletion of HREE if compared to MREE (Fig.
392 5b). This is testified by the (La/Yb)_N, (Sm/Yb)_N, and (Dy/Yb)_N ratios, which are in the
393 range 4.44 – 7.86, 1.18 – 3.16, and 1.25 – 1.56, respectively (Figs. 6a, b). The Yb and La
394 contents are in the range 8.5 - 13.8 and 37.8 - 90.3, times chondrite abundance,
395 respectively (Figs. 5b, 6c). The overall chemical features of the Group 1 rocks are similar
396 to those of many plume-type MORB (P-MORB) in modern oceanic settings (e.g., Le Roex
397 et al., 1983; Sun and McDounough, 1989; Haase and Devey, 1996). Accordingly, in the
398 discrimination diagram in Fig. 7, these rocks plot in the fields for oceanic subduction-
399 unrelated setting, between the compositional fields of P-MORBs and Alkaline basalts.

400 These geochemical data collectively suggest a P-MORB affinity for Group 1 basaltic
401 rocks. Compared to the basaltic samples, the trachyte MK795 shows higher SiO₂ and lower
402 MgO contents (Table 1). As commonly observed in highly fractionated rocks, this sample
403 shows very high Zr (701 ppm) and Y (58 ppm) contents and very low contents of
404 compatible elements, TiO₂ and P₂O₅ (Table 1) as a consequence of early crystallization and
405 removal of mafic minerals, Fe-Ti oxides, and apatite. In fact, this sample shows N-MORB
406 normalized incompatible elements spider-diagrams with significant Ti and P negative
407 anomalies (Fig. 5a). The chondrite-normalized REE pattern of this sample shows a marked
408 Eu negative anomaly and depletion of middle REE (MREE) with respect to HREE (Fig.
409 5a), which suggest crystallization and removal of plagioclase and amphibole, respectively,
410 prior to the formation of the trachytes melts.

411

412 5.2. Group 2 rocks

413

414 The Group 2 rocks include basaltic, and ferrobasaltic rocks, as well as one alkali
415 rhyolitic sample. These rocks show a clear alkaline affinity, as indicated by Nb/Y ratios
416 greater than 1 (Table 1, Fig. 4). Basaltic rocks are characterized by SiO₂ ranging from
417 41.94 to 53.52 wt% and Mg# ranging between 75 and 39 suggesting that these rocks
418 represent melts at different stages of magmatic fractionation. Accordingly, these rocks
419 show marked variation of MgO and Al₂O₃ contents (Table 1). The basaltic rock of the
420 Group 2 show relatively high contents of TiO₂ (1.55 – 5.13 wt%), P₂O₅ (0.20 – 1.10 wt%),
421 Zr (139 – 403 ppm), Nb (23.6 – 71.8 ppm), and Ta (1.42 – 5.13 ppm). Ti/V ratios (41 - 76)
422 are in the range for alkaline basalts (Shervais, 1982). In contrast, Y abundance is rather
423 low, ranging between 18.5 to 33.0 ppm. Compared to Group 1 basalts, the Ti/Y (526 –
424 1448) and Zr/Y (6.7 – 20.6) ratios in Group 2 basalts are higher. The N-MORB normalized

425 incompatible elements spiderdiagrams (Figs. 5c, e) display decreasing patterns from Th to
426 Yb. Yb contents are ~0.6 times N-MORB abundance and are comparable with those of
427 Group 1 rocks. In contrast, both Ta and Nb contents are slightly higher than those of Group
428 1 rocks (Figs. 5a, c, Table 1). The chondrite normalized REE patterns (Figs. 5d, f) show
429 marked decrease from LREE to HREE ($La_N/Yb_N = 9.26 - 28.07$) with Yb and La contents
430 ranging from ~6 - 13 to ~ 100 - 250 times chondrite abundance (Sun and McDonough,
431 1989), respectively. In addition, HREE show marked depletion with respect to MREE, as
432 exemplified by the $(Sm/Yb)_N$ ratios (3.5 – 8.4), which are higher with respect to those of
433 Group 1 (Figs. 6a, b; Table 1).

434 By contrast, alkali rhyolite sample MK339 shows higher contents of SiO_2 and lower
435 MgO abundance with respect to the basaltic rocks (Table 1). This sample shows very high
436 Zr (608 ppm) and Y (69.9 ppm) and very low contents of compatible elements, TiO_2 and
437 P_2O_5 (Table 1). This sample shows N-MORB normalized incompatible elements spider-
438 diagrams with significant Ti and P negative anomalies (Fig. 5c). The chondrite-normalized
439 REE pattern of this sample shows a marked Eu negative anomaly and depletion of HREE
440 with respect both LREE and MREE (Fig. 5d). The overall geochemical features of Group 2
441 rocks are very similar to those of the within-plate alkaline volcanic rocks typically forming
442 oceanic islands (e.g., Yang et al., 2015; Safonova et al., 2016 and reference therein). In the
443 discrimination diagram in Figure 7, the Group 2 rocks plot close to the composition of the
444 ocean island basalt (OIB) (Sun and McDonough, 1989) and within the field for subduction
445 unrelated alkaline basalts.

446 Although Group 2 basaltic rocks show similar major elements and most trace elements
447 contents at comparable degree of fractionation (e.g., comparable Mg#), two different
448 subgroups of samples (hereafter named as Group 2a and Group 2b) can be identified based
449 on different REE patterns and REE ratios, as well as different ratios of some trace

450 elements. These differences are summarized by the REE ratios shown in [Figure 6](#). Group
451 2a basaltic rocks show definitely lower $(La/Yb)_N$ and $(Sm/Dy)_N$ ratios compared to Group
452 2b equivalents ([Figs. 6a, b](#)). In contrast the $(Sm/Yb)_N$ ratios shown by Group 2a and Group
453 2b rocks are largely overlapping, though, as a general tendency, these ratios are
454 comparatively higher in Group 2b rocks ([Figs. 6a, b](#)). The variation of the REE ratios
455 shown in [Figure 6](#) is totally independent from the degree of fractionation of the different
456 samples. It should also be noted that there is no correlation between the LREE/HREE (e.g.,
457 La_N/Yb_N) ratio and the absolute concentration of HREE (e.g., Yb_N) suggesting that the
458 enrichment in LREE with respect to HREE is totally independent on the absolute content
459 of HREE ([Fig. 6c](#)). In addition, Group 2b rocks show higher Nb/Y ([Fig. 4](#)), Nb/Yb, and
460 Th/Tb ratios compared to basaltic rocks of Group 2a

461

462

463 6. Clinopyroxene chemistry

464

465 No unaltered olivine or plagioclase was identified in the studied rocks, and
466 clinopyroxene underwent secondary alteration in many of the studied samples.
467 Nonetheless, a detailed petrographic study allowed us to recognize fresh clinopyroxene
468 crystals in basaltic samples of the different rock groups, as well as fresh magmatic
469 clinopyroxene relics in one metabasaltic sample. Representative chemical analyses of these
470 crystals are shown in [Table 2](#), whereas their classification according to the quadrilateral
471 diagram is given in [Supplementary Figure S2](#). In addition to crystal-chemical constraints,
472 the clinopyroxene composition is strongly influenced by the composition of the magmas
473 from which they crystallized. According to [Leterrier et al. \(1982\)](#) and [Beccaluva et al.](#)
474 [\(1989\)](#), clinopyroxene composition represents a petrogenetic indicator of the chemical

475 affinity of the magmatic melts from which they crystallized. Therefore, the mineral
476 chemistry of clinopyroxene can provide us robust constraints for understanding the
477 tectono-magmatic setting of formation of basaltic melts. The chemical features of
478 clinopyroxenes will be described according to the whole rock chemical groups.

479

480 *6.1. Group 1 rocks*

481

482 Clinopyroxenes in Group 1 basalts show augitic composition with the wollastonite
483 end-member ranging from ~38% to ~42% (Table 2). Clinopyroxenes of Group 1 rocks
484 show Mg# in the range 0.77 - 0.65, likely reflecting the crystallization from melts at
485 different fractionation stages. CaO, Al₂O₃, and Cr₂O₃ decrease with decreasing Mg#,
486 whereas FeO_{tot} and TiO₂ generally increase with the decreasing Mg# (Table 2). They
487 display relatively low contents of TiO₂ (0.91 – 1.45 wt%), Na₂O (0.28 – 0.46 wt%) and
488 CaO (19.26 – 21.11 wt%) compared to clinopyroxenes from Group 2a and Group 2b rocks
489 (Table 2, Fig. 8). Al₂O₃ (1.44 – 3.06 wt%) is lower than Group 2a and Group 2b
490 clinopyroxene at comparable value of Mg# (Table 2). The Cr₂O₃ content is relatively low
491 and shows positive correlation with Mg#. They are commonly unzoned; only three crystals
492 show little chemical variation from core to rim (Table 2). According to the discrimination
493 diagrams proposed by Leterrier et al. (1982), clinopyroxenes from Group 1 basalts plot in
494 the field for clinopyroxene from sub-alkaline tholeiitic and calc-alkaline rocks and are
495 clearly distinguished from clinopyroxene from Group 2a and Group 2b (Fig. 9a). In
496 addition, the (Ti + Cr) vs. Ca diagram shows that clinopyroxene from Group 1 rocks
497 display MORB affinity (Fig. 9b). Accordingly, in the discrimination diagram of Beccaluva
498 et al., (1989), they plot in the field for clinopyroxene from MOR and within-plate oceanic
499 settings (Fig. 10).

500

501 *6.2. Group 2a rocks*

502

503 Clinopyroxene from Group 2a were analysed in basalts and ferrobasalts. They mainly
504 show augitic composition, though a few crystals display diopsidic composition. The
505 wollastonite end-member range from ~43% to ~50% (Table 2). Mg# is generally high,
506 ranging from 0.74 to 0.84. TiO₂ (1.01 – 2.1 wt%), Na₂O (0.33 – 0.5 wt%), CaO (21.02 –
507 22.3 wt%), and Al₂O₃ (2.66 – 4.39 wt%) contents are generally higher than in
508 clinopyroxene from Group 1 rocks (Table 2; Fig. 8). Cr₂O₃ content is variable (0.12 – 0.67
509 wt%) and gradually decreases with decreasing Mg#. The crystals from sample MK479 are
510 unzoned whereas those from sample MK491 commonly show zoning with Mg# in cores
511 higher than the rims. This variation is coupled with an increase of TiO₂, Al₂O₃, and FeO_{tot}
512 contents, and a decrease of Cr₂O₃, MgO, and CaO from core to rim (Table 2). These
513 compositional variations likely reflect fractional crystallization processes during the
514 growth of the crystals, as typically observed in clinopyroxene from ophiolitic sequence
515 (Beccaluva et al., 1989). In the Ti – (Ca + Na) variation diagram, the clinopyroxenes from
516 Group 2a rocks plot in the field for pyroxene from alkaline rocks and are clearly
517 distinguished from the clinopyroxene of the Group 1 rocks (Fig. 9). Accordingly, in the
518 discrimination diagram of Beccaluva et al. (1989), they plot in the field for clinopyroxenes
519 typical of plume-influenced Iceland basalts and within-plate oceanic basalts (Fig. 10).

520

521 *6.3. Group 2b rocks*

522

523 Clinopyroxene from Group 2b rocks were analysed in basaltic, ferrobasaltic and
524 metabasaltic samples (Table 2). They are mainly represented by diopsidic clinopyroxenes

525 and minor augite. The wollastonite end-member ranges from ~47% to ~49% (Table 2).
526 Mg#, though variable, is generally high (0.74 - 0.87). Clinopyroxenes in Group 2b rocks
527 show generally higher contents of TiO₂ (1.26 – 3.69 wt%), Na₂O (0.28 – 0.66 wt%), CaO
528 (21.7 – 24.3 wt%), and Al₂O₃ (2.88 – 7.08 wt%) compared to those from the other groups
529 of rocks (Fig. 8). Cr₂O₃ contents vary from 0.01 to 1.0 wt% and are positively correlated
530 with Mg# values. Concentric zoning and multiple zones of growth are frequently observed.
531 The zoning is associated to significant chemical variations of TiO₂, CaO, Al₂O₃, Na₂O,
532 MgO, FeO_{tot} and Cr₂O₃ contents from core to rim (Table 2). Generally, the core of the
533 crystals shows higher MgO, Cr₂O₃, and CaO contents coupled with lower TiO₂, Al₂O₃,
534 Na₂O, and FeO_{tot} contents with respect to the rim. However, reverse zoning is observed in
535 some crystals. In addition, some crystals show concentric, oscillatory zoning characterized
536 by different zones of growth, showing rhythmic variation of TiO₂, CaO, Al₂O₃, Na₂O,
537 MgO, FeO_{tot} and Cr₂O₃ contents (Table 2). This is particularly evident for the sample
538 MK859cr1, in which TiO₂, Na₂O, MgO, and Cr₂O₃ show oscillatory chemical variation
539 from the core to the rim of the crystal (Table 2). These features collectively indicate that
540 the growth of the crystals occurred either from a progressively differentiating melt or from
541 the equilibrium with different pulses of new batches of primitive melts at different
542 fractionation stages. The clinopyroxenes of the Group 2b rocks plot in the field for
543 clinopyroxene of alkaline rocks (Fig. 9). An alkaline affinity for the clinopyroxene of
544 Group 2b rocks is also suggested by the discrimination diagram in Figure 10, where they
545 plot within the field for plume-influenced Iceland and within-plate oceanic basalts.

546

547 *6.4. Correlation of clinopyroxene composition vs. whole rock geochemistry*

548

549 Our mineral chemistry data show that there is a close relationship between the
550 composition of clinopyroxenes and the compositions of their hosting rocks. The diagrams
551 in [Figure 8](#) show that the variations of TiO₂, CaO, and Na₂O with respect to the variations
552 of Mg# in clinopyroxenes depict different trends depending on the different rock groups in
553 which these minerals are hosted. Clinopyroxenes from Group 1 transitional basaltic rocks
554 show relatively smooth increase in TiO₂ and Na₂O contents coupled with relatively sharp
555 decrease in CaO contents with decreasing Mg#. In contrast, in clinopyroxenes from the
556 alkaline basaltic rocks of Group 2a and Group 2b TiO₂ and Na₂O contents show sharp
557 increase with decreasing Mg#, whereas CaO contents decrease very smoothly with
558 decreasing Mg# ([Fig. 8](#)). In addition, clinopyroxenes from Group 2a and Group 2b show
559 distinct elemental behaviour with respect to the variation of Mg# values ([Fig. 8](#)). In
560 particular, clinopyroxenes from Group 2b show the relatively sharper increase of TiO₂ and
561 Na₂O contents with decreasing Mg# compared to clinopyroxenes from Group 2a ([Figs. 8a,](#)
562 [c](#)). Clinopyroxenes from Group 2a basaltic rocks are also characterized by higher (Ca +
563 Na) contents compared to those from Group 2b ([Fig. 9](#)). The variation in TiO₂ contents in
564 clinopyroxenes is commonly thought to reflect the degree of depletion or enrichment of the
565 mantle source ([Pearce and Norry, 1979](#)). High TiO₂ content in clinopyroxenes point out for
566 their crystallization from primary magmas generated from enriched mantle sources. The
567 diagrams in [Figure 11](#) clearly show a positive correlation between the Nb/Y ratios of the
568 hosting rocks and the TiO₂, CaO, and Al₂O₃ contents of their clinopyroxenes. The increase
569 in Nb/Y ratios in basaltic rocks is commonly associated with the increase of enrichment of
570 the mantle sources from which they originated ([Winchester and Floyd, 1979](#); [Pearce, 1996,](#)
571 [2008](#)). The contents in TiO₂, CaO, and Al₂O₃ in clinopyroxenes increase from transitional
572 Group 1 basalts to alkaline Group 2a and Group 2b basaltic rocks. Different compositions
573 and elemental co-variations can clearly be distinguished in the clinopyroxenes of the

574 different groups of rocks (Figs. 8, 9, 11). This evidence further supports the conclusions
575 obtained from whole rock chemistry that is, in the Durkan volcanic and metavolcanic rocks
576 three different groups of rocks can be identified (see section 5).

577

578

579 7. Discussion

580

581 *7.1. Melt petrogenesis of the volcanic and metavolcanic rocks*

582

583 The aim of this petrogenetic discussion is to identify the possible mantle sources for
584 the volcanic rocks and the magmatic protoliths of the metavolcanic rocks from the Durkan
585 Complex, as well as their melting conditions, in order to provide robust constraints for the
586 interpretation of the tectono-magmatic setting of formation of this Complex. Sections 5
587 and 6 have shown that the volcanic and metavolcanic rocks of the Durkan Complex exhibit
588 whole-rock and mineral chemistry with transitional (Group 1) and alkaline (Group 2a and
589 Group 2b) affinities. The different trace elements contents (e.g., Zr, Y, Nb) and REE
590 patterns (Fig. 5) observed in the rocks of these three groups, as well as their different
591 incompatible element (e.g., Zr/Y, Y/Nb, Nb/Yb) and REE ratios (i.e., La_N/Yb_N , Sm_N/Yb_N ,
592 Sm_N/Dy_N) (Table 2, Fig. 6) suggest that these rocks were derived from partial melting of
593 chemically distinct mantle sources and/or different melting conditions. Very similar HREE
594 (e.g., Yb) contents and no correlations between the LREE/HREE (i.e., La_N/Yb_N) ratios
595 observed in all rock groups (Table 2, Fig. 6c) suggest that the differences in the chemistry
596 of their possible mantle sources most likely consisted of different enrichments in LREE,
597 Zr, and Nb. A first idea about the petrogenesis of the Durkan volcanic and metavolcanic
598 rocks can be deduced from the Zr-Nb co-variation diagram in Figure 12a, which shows

599 that these rocks were generated by partial melting of an enriched and/or transitional mantle
600 source. The mineral chemistry of the clinopyroxenes, in particular their high TiO₂ contents,
601 also point out for the genesis of these rocks from a transitional to enriched mantle sources
602 (Fig. 10). The diagram in Figure 12b further supports this conclusion; in fact, the studied
603 rocks plot along the mixing curve between N-MORB and OIB with compositions
604 clustering toward the OIB end member. In addition, the enrichment of OIB-type chemical
605 components increases from Group 1 to Groups 2a and 2b (Fig. 12b). The Th-Nb co-
606 variation (Fig.7) further point out for a genesis of the studied rocks from the partial melting
607 of mantle sources that have been influenced by OIB-type chemical components prior to
608 melting without any contributions from subduction related chemical components and/or
609 continental crust contamination.

610 Given these considerations, we performed a semi-quantitative non-modal, batch partial
611 melting modelling in order to constrain the possible mantle peridotite compositions and
612 melting conditions that can reproduce the compositions of the most primitive basalts for
613 each geochemical group of rocks. An accurate definition and quantification of the
614 composition of mantle sources and degrees and depths of partial melting generating the
615 different rock-types is not possible, as these factors cannot be exactly constrained.
616 Therefore, we used different models based on incompatible trace elements ratios and REE
617 in order to better constrain the petrogenesis of the studied rocks (Figs. 13, 14). These
618 elements are used in the commonly accepted assumption that their content in basaltic rocks
619 basically depend on the composition of the mantle source and its degree of partial melting
620 and it is little influenced by moderate degrees of fractional crystallization of olivine,
621 clinopyroxene and plagioclase (e.g., Allègre and Minster, 1978).

622 The models in Fig. 13 have the advantage of combining information about the
623 increasing of enrichment of the mantle source (i.e., increasing of Nb/Yb with respect to

624 TiO₂/Yb in Fig. 13a and increasing of Th with respect to Nb/Yb in Fig. 13b) and the
625 presence of residual garnet in the source (i.e., TiO₂/Yb in Fig. 13a and Nb/Yb compared to
626 Th in Fig. 13b). Results from these binary models have been then compared with the REE
627 model (Fig. 14). We have previously shown that the composition of the Durkan volcanic
628 and metavolcanic rocks strongly point out for a genesis from partial melting of sub-oceanic
629 mantle sources that have been influenced by OIB-type chemical components. Therefore, in
630 our models we chose as a possible mantle source for the Durkan basaltic rocks a sub-
631 oceanic slightly depleted lherzolite residual after small volume of MORB melt extraction
632 metasomatized to various extents of enrichment by an OIB-type chemical component. In
633 our models, we used the lherzolite ZB2 from the Northern Apennines (Barbero et al.,
634 2020c) as representative of a slightly depleted sub-oceanic mantle and the enriched mantle
635 of Lustrino et al. (2002) as the metasomatizing chemical component. The modal
636 compositions of the assumed mantle sources, their chemical composition, the melting
637 proportions and the REE and trace elements distribution coefficients used in the models are
638 listed in Supplementary Table 2.

639

640 7.1.1. Group 1 rocks

641

642 The Nb/Yb vs. TiO₂/Yb model (Fig. 13a) shows that Group 1 rocks cannot be
643 generated from the partial melting of sources with depleted composition as the DMM
644 (Workman and Hart, 2005) or the lherzolite ZB2 (Barbero et al., 2020c). By contrast, the
645 geochemistry of Group 1 primitive basalts is compatible with the partial melting of a
646 calculated S1 mantle source that is significantly more enriched in Nb with respect to the
647 DMM and ZB2 mantle peridotites (Fig. 13a). The high TiO₂/Yb ratios characterizing the
648 Group 1 basalts can be explained by the presence of residual garnet in the mantle source

649 and, therefore, that partial melting started in the garnet-facies mantle (Fig. 13a).
650 Accordingly, the Nb/Yb vs. Th petrogenetic model suggest that the compositions of Group
651 1 primitive basalts can be explained by partial melting of the enriched mantle source S1
652 that starts partial melting in the garnet-facies mantle and continues to larger degrees in the
653 spinel-facies mantle. In detail, the model shows that partial melting degrees are ~2% and
654 ~7% in garnet- and spinel-facies, respectively with mixing of the different melts produced
655 in equal proportions (Fig. 13b).

656 The REE modelling well confirms these results clearly indicating that the REE
657 composition of Group 1 basalts can be explained by partial melting of the mantle source
658 S1, which is significantly enriched in LREE with respect to the DMM and the residual sub-
659 oceanic peridotite ZB2 by OIB-type chemical components (Fig. 14a). According to the
660 results from the models shown in Figure 13, the rather high (Sm/Yb)_N ratios displayed by
661 Group 1 rocks suggest the involvement of residual garnet in their mantle source. In fact,
662 the composition of Group 1 primitive basalt MK282 fits well with the melt calculated for
663 2.5% and 7.5% of partial melting of the S1 mantle source at garnet- and spinel-facies,
664 respectively, with a mixing proportion between melts generated in the garnet and spinel
665 melts of 50:50 (Fig. 14a). Different melting degrees and mixing proportions of different
666 melts (Fig. 14a₁) fail to reproduce the REE composition of the Group 1 relatively primitive
667 basalt.

668 The fairly differentiated trachyte MK795 clearly display different geochemical
669 patterns compared to basaltic rocks of this Group (Figs. 5a, b). Shallow-level (i.e., magma
670 chamber) petrogenetic processes are beyond the scope of this work since the main goal of
671 this paper is to define the petrogenesis of primary melts in order to constrain their tectono-
672 magmatic setting of formation. In addition, as commonly seen in ophiolites, the
673 tectonically dismembered nature of the volcanic series does not allow basalt-differentiated

674 rocks comagmatic relationships to be reliably constrained. This is particularly true in the
675 Durkan Complex where differentiated samples are very rare. However, differentiated rocks
676 may have various origins and may eventually not be genetically related to the associated
677 mafic rocks. In fact, they may have been generated by fractional crystallization, partial
678 melting of lower crustal rocks (i.e., anatexis), mixing of different melts, etc. We therefore
679 performed Rayleigh fractionation model using REE. Results are shown in [Supplementary](#)
680 [Figure S3](#) together with model parameters and constraints. This model clearly indicates
681 that the REE compositions of the trachyte MK795 is compatible with the composition of a
682 24% residual melt after various steps of crystal fractionation of olivine, plagioclase,
683 clinopyroxene, hornblende, magnetite, and ilmenite starting from the composition of the
684 near-primary basalt MK282 used in the mantle partial melting model shown above (see
685 also [Figs. 13, 14](#)). It follows that trachyte MK795 represent a differentiated product formed
686 by fractional crystallization.

687

688 7.1.2. Group 2a and Group 2b rocks

689

690 Group 2a and Group 2b alkaline rocks collectively show overall whole rock chemistry
691 ([Table 1](#); [Fig. 6](#)) and mineral chemistry ([Fig. 9](#)) that are quite different from those of the
692 transitional Group 1 rocks. In particular, basaltic rocks from these groups show much
693 higher Nb, Ta, Th, LREE/HREE and MREE/HREE ratios with comparable Yb absolute
694 contents ([Fig. 6](#); [Table 1](#)), which cannot be explained with partial melting of the S1 source.
695 These chemical features point out for a genesis from a mantle source more enriched
696 (source S2) in these elements and LREE compared to the theoretical S1 source. Similar to
697 Group 1 rocks, the high $(La/Yb)_N$, TiO_2/Yb , and Nb/Yb ratios of Group 2a and Group 2b
698 rocks suggest residual garnet in the mantle source ([Figs. 6a, 13](#)). Nonetheless, Group 2a

699 and Group 2b rocks, though very similar in composition for many elements, slightly differ
700 in their $(\text{La}/\text{Yb})_{\text{N}}$ and $(\text{Sm}/\text{Dy})_{\text{N}}$ ratios (Fig. 6). These differences can be explained either
701 with slightly different compositions of their mantle sources or different proportions of
702 partial melting in the garnet- and spinel-facies mantle. However, the chemical differences
703 between basalts of these two groups are limited to a few elemental ratios basically
704 involving HREE (e.g., TiO_2/Yb , Nb/Yb , Th/Tb , Sm/Dy). As a consequence, it is
705 reasonable to assume that the chemical differences between basalts of these two Groups
706 are most likely due to different proportions of partial melting in the garnet- and spinel-
707 facies mantle, rather than chemical differences of the mantle sources. Therefore, in the
708 models in Figures 13 and 14 we use the same theoretical mantle source S2 for both Group
709 2a and 2b basalts. In fact, the TiO_2/Yb vs. Nb/Yb model suggests that the genesis of
710 relatively primitive basalts from both rock groups is related to the partial melting of the
711 mantle source S2 that starts in the garnet-facies mantle. However, the composition of the
712 relatively primitive basalt of Group 2a is compatible with partial melting starting at a
713 higher pressure (4GPa) compared to Group 2b primitive basalt (3GPa) (Fig. 13a). The
714 Nb/Yb vs. Th model show that the composition of Group 2a relatively primitive basalt
715 MK340 is compatible with ~2% partial melting of the source S2 in the garnet-facies mantle
716 followed by 5% partial melting in the spinel-facies mantle, with mixing of the different
717 melts in the proportions 60% garnet melt - 40% spinel melt. (Fig. 13b). In contrast, the
718 composition of Group 2b relatively primitive basalt MK499 is compatible with 1% partial
719 melting of the source S2 in the garnet-facies mantle followed by ~3% partial melting in the
720 spinel-facies mantle, with mixing of the different melts in the proportions 65% garnet melt
721 - 35% spinel melt. (Fig. 13b).

722 Accordingly, REE model indicates that the REE composition of the relatively
723 primitive basalt MK340 (Group 2a) can be explained by ~2 % partial melting in the garnet-

724 facies and ~5% partial melting in the spinel-facies of the mantle source S2 with mixing of
725 the different melts in the proportions 60% garnet melt - 40% spinel melt (Fig. 14b).
726 Likewise, the REE model carried out for Group 2b rocks (Fig. 14c) is perfectly in
727 agreement with the models based on TiO₂, Nb, Th, and Yb contents (Fig. 13). The model
728 in Figure 14c shows indeed that the REE composition of the relatively primitive basalt
729 MK499 is compatible with 1.5% partial melting in the garnet-facies mantle followed by
730 4% partial melting in the spinel-facies mantle of the source S2, with mixing of the different
731 melts in the proportions 65% garnet melt - 35% spinel melt.

732 As already discussed in section 7.1.1 for the trachyte MK795, the different chemistry
733 of the alkali rhyolite MK339 compared to Group 2 basalts (Figs. 5c-f) may reflect the
734 effect of fractional crystallization, or anatexis, or other petrogenetic processes. Rayleigh
735 fractionation model using REE are shown in Supplementary Figure S3. This model clearly
736 shows that the REE compositions of the alkali rhyolite MK339 is compatible with the
737 composition of a 25% residual melt after various steps of crystal fractionation of olivine,
738 plagioclase, clinopyroxene, magnetite, and ilmenite starting from the composition of the
739 near-primary basalt MK340 used in the mantle partial melting model for Group 2a rocks
740 (see also Figs. 13, 14b).

741

742 *7.2. Tectono-magmatic significance of the volcanic and metavolcanic rocks*

743

744 Previous studies have suggested that the Durkan Complex represents remnants of the
745 Permian - Cretaceous continental margin of the Bajgan Complex microcontinental
746 basement (McCall, 1985; Hunziker et al., 2015). However, a recent multidisciplinary study
747 of the western part of the Durkan Complex has demonstrated that it consists of Late
748 Cretaceous volcano-sedimentary successions, which represent portions of a seamount or,

749 most likely, of a seamount chain (Barbero et al., 2021). The geochemical and mineral
750 chemistry data, as well as petrogenetic models presented in this paper collectively suggest
751 that the volcanic rocks in these sequences consist of an association of transitional P-
752 MORBs and alkaline OIBs, which were formed by partial melting of enriched mantle
753 sources with variable contribution of melts formed at both garnet- and spinel-facies. These
754 data strongly support the interpretation of the Barbero et al. (2021). In Figure 15 we
755 therefore propose a schematic tectono-magmatic model that can explain the petrogenetic
756 processes, which occurred during the formation of the Durkan seamount chain. According
757 to Barbero et al. (2021), the Type-II and Type-III volcano-sedimentary successions consist
758 of remnants of seamount flank and seamount summit depositional and eruptional settings,
759 respectively, and were formed during the Cenomanian in the shallow-water stage of
760 growth of a seamount (Fig. 15a). These types of successions are characterized by alkaline
761 volcanic rocks (Group 2a and Group 2b), whose geochemistry and melt petrogenesis (see
762 section 7.1) clearly indicate that they derived from low degree of partial melting at both
763 garnet- and facies-spinel of an enriched OIB-type (plume-type) mantle source (S2 in Fig.
764 15a). By contrast, the Type-I volcano-sedimentary succession represents the remnants of
765 Coniacian – early Campanian sedimentation and volcanism in a pelagic setting during the
766 deep-water stage of growth of a seamount (Fig. 15b; Barbero et al., 2021). This Type of
767 succession is mainly characterized by transitional P-MORB rocks (Group 1) and minor
768 Group 2a alkaline rocks, whereas Group 2b basalts were not found in this succession. The
769 petrogenetic model show that, compared to Group 2a basalts, Group 2b basalts are
770 characterized by higher proportions of melts formed at garnet-facies with respect to melts
771 formed at spinel-facies mantle and an overall smaller degree of partial melting (Fig. 14).
772 By contrast, the deep-water stage of formation of the seamounts was characterized by the
773 partial melting of an enriched mantle source bearing strongly enriched mantle patches

774 (sources S1 and S2, respectively in [Fig. 15b](#)). The lack of Group 2b rocks and the
775 prevalence of Group 1 rocks may also be explained by mantle partial melting at relatively
776 shallower depth and higher partial melting degree during the deep-water stage of the
777 seamount formation with respect to the shallow-water stage of the seamount growth ([Figs.](#)
778 [15a, b](#)). In addition, this implies a minor contribution of melts produced at garnet-facies
779 with respect to the shallow-water stage of the seamount growth. These features are
780 compatible with oceanic within-plate magmatism related to the rising of deep, enriched
781 mantle plume material ([Figs. 15a, b](#)). Indeed, mantle plumes are likely the most effective
782 mean for transferring anomalous heat flux and enriched chemical components from the
783 lower to the upper mantle (e.g., [Regelous et al., 2003](#); [Pearce, 2008](#); [White, 2010](#); [Kerr,](#)
784 [2014](#); [Safonova and Santosh, 2014](#)). The rising of mantle material that is more enriched
785 and hotter than the ambient sub-oceanic mantle facilitates the starting of the partial melting
786 at deeper level within the garnet stability field ([Figs. 15a, b](#)). This can well explain the
787 clear residual garnet geochemical signature shown by all the studied rocks. The processes
788 responsible for the geochemical variation of the erupted basalts during the different stage
789 of growth of the Durkan seamount chain are difficult to be constrained in detail, mainly
790 because of the disrupted tectonic nature of the different Durkan successions, which is, in
791 turn, related to multiple deformative events occurred during their incorporation into the
792 accretionary prism ([Barbero et al., 2021](#)). However, it is commonly accepted that during
793 the progressive growth of seamounts, from the early stage of formation to their emergence
794 above the sea level (i.e., shallow-water shield stage), the volcanic products progressively
795 change from tholeiitic rocks to progressively more enriched transitional and alkaline rocks
796 (e.g., [Moore and Clague, 1992](#); [Regelous et al., 2003](#)). In this classical scenario the Durkan
797 Type I, II and III successions are associated with progressive chemical changes of magmas
798 from tholeiitic to alkaline signatures, which could be mainly derived from different degrees

799 of partial melting of variably enriched mantle sources. The chemical composition of
800 analysed clinopyroxenes is also consistent with progressive chemical changes of magmas
801 from tholeiitic to alkaline nature. The chemical variation of seamount volcanic rocks may
802 be explained by the combination of several factors, such as: 1) the increasing contribution
803 from an enriched mantle source to the ambient sub-oceanic mantle; 2) the decreasing in
804 partial melting degrees; 3) the increase of the depth of partial melting; 4) the variation of
805 the thickness of the melting column (e.g., [Regelous et al., 2003](#); [Safonova, 2008](#); [White,](#)
806 [2010](#); [Safonova and Santosh, 2014](#)). According to [Safonova et al. \(2016\)](#), the large
807 volumetric prevalence of alkaline rocks in the shallow-water shield stage of the Durkan
808 volcano-sedimentary sequences suggest relatively higher contributions of melting in the
809 garnet-facies of a strongly enriched mantle source during this stage coupled with the
810 decrease of the overall partial melting degree ([Fig. 15a](#)). These features are consistent with
811 the deepening of the partial melting region in response of the enhancing of the lithospheric
812 load (i.e., crust + lithospheric mantle) due to the thickening of the seamount edifice
813 coupled with an increasing of the mantle plume influence on the sub-oceanic ambient
814 mantle and a shortening of the melting mantle column ([Fig. 15a](#)). By contrast, during the
815 deep-water stage of the seamount life the crustal load is significantly lower. In this stage,
816 the sub-oceanic mantle is relatively less influenced by the metasomatizing effects of the
817 mantle plume ([Fig. 15b](#)). The combination of these effects likely produces partial melting
818 of a moderately enriched mantle source, though partial melting may also involve strongly
819 enriched portions of the mantle. In this stage, partial melting in the spinel-facies is
820 prevailing with respect that in the garnet-facies mantle as the melting mantle column is
821 rather wide ([Fig. 15b](#)). This hypothesis agrees with data from both modern and ancient
822 seamounts, which point out the importance of the lithospheric thickness in controlling the
823 melting processes associated with the rising of a mantle plume. In detail, a thin lithosphere

824 above a mantle plume causes the shallowing of partial melting combined with higher
825 degree of the partial melting, producing melts less enriched in LREE with respect to M-
826 and HREE. By contrast, higher thickness of lithosphere likely causes the deepening of the
827 partial melting region combined with the decrease of the partial melting degree and the
828 shortening of the melting column, thus, promoting the prevalence of partial melting at the
829 garnet-facies (e.g., [Regelous et al., 2003](#); [Safonova, 2008](#); [White, 2010](#)).

830

831

832 *7.3. Geodynamic significance of the western Durkan Complex: A Late Cretaceous*
833 *seamount chain in the northern Neo-Tethys?*

834

835 Cretaceous alkaline and OIB rocks comparable with those of the Durkan Complex are
836 widespread within the Neo-Tethys-related collisional belts from Caucasus to Himalaya.
837 They have commonly been interpreted as remnants of seamounts and/or oceanic plateau
838 associated with mantle-plume activity (e.g., [Rolland et al., 2010, 2020](#); [Saccani et al.,](#)
839 [2013, 2018](#); [Yang and Dilek, 2015](#); [Yang et al., 2015, 2019](#); [Esmaili et al 2019](#); [Barbero](#)
840 [et al., 2020b, 2021](#)). This evidence supports the hypothesis that the tectono-magmatic
841 evolution of different sectors of the Neo-Tethys Ocean was strongly influenced by the
842 wide occurrence of mantle plume activity at a regional-scale during the Late Cretaceous.
843 Our data well agree with this general scenario of the Cretaceous Neo-Tethys, as they point
844 out for the existence of a significant mantle plume activity in the Makran sector of this
845 Ocean during the same time. Our data allow us to depict two different stages of a seamount
846 growth at two different times. The Type-II and Type-III volcano-sedimentary successions
847 of the Durkan Complex include Cenomanian carbonatic platform and strongly enriched
848 alkaline basalts, thus recording the existence of one or more oceanic seamounts that

849 reached a shallow-water shield stage during the early Late Cretaceous (Fig. 15a). The
850 occurrence of “mature” seamount edifices implies that a vigorous mantle plume activity
851 was already existing in the oceanic basin at that time. By contrast, the Durkan Type-I
852 succession, which is characterized by pelagic sediments and prevailing transitional
853 volcanic rocks, records an early phase of growth of a seamount (i.e., deep-water stage) in
854 the late Late Cretaceous (Fig. 15b). A general fading away at the end of Cretaceous of
855 OIB-type volcanism is observed in the Neo-Tethyan related belts from Caucasus to
856 Himalaya and it is interpreted to reflect a progressively decreasing mantle plume activity in
857 the Neo-Tethys during these times (e.g., Rolland et al., 2010, 2020; Yang and Dilek, 2015;
858 Esmaeili et al 2019; Barbero et al., 2020b, 2021). We can speculate that the occurrence in
859 the Durkan Complex of a relatively older (Cenomanian) mature seamount and a relatively
860 younger (Coniacian – Campanian) immature seamount may eventually be related to the
861 Late Cretaceous progressive decreasing of plume activity observed at a regional scale. This
862 hypothesis needs, however, to be proved by further studies.

863

864

865

866

8. Conclusion

867

868

869

870

871

872

The Durkan Complex represents a tectonic element of the North Makran domain that was classically interpreted as a continental margin succession though a recent study suggested that it represents a tectonically disrupted portion of a Late Cretaceous seamount chain. The petrographic and geochemical study presented in this paper allow the following conclusion to be drawn:

- 873 1) The Durkan Complex is composed by tectonic slices showing successions similar
874 to those found at different depths of a seamount environment. The successions are
875 characterized by abundant volcanic rocks and are either non-metamorphic or
876 slightly metamorphosed.
- 877 2) The volcanic and metavolcanics rocks are largely represented by basaltic rocks.
878 Based on whole rock chemistry and clinopyroxene chemistry, basaltic rocks
879 consist of both transitional basalts showing P-MORB composition (Group 1) and
880 alkaline basalts showing OIB composition (Groups 2a and 2b).
- 881 3) The chemical composition of clinopyroxenes from the different rock groups is
882 strictly depending on the whole rock composition of their hosting rocks. In
883 particular, TiO_2 , Al_2O_3 , and Na_2O contents in minerals increase from transitional to
884 alkaline basalts.
- 885 4) Petrogenetic models indicate that the Durkan volcanic rocks derived from partial
886 melting of a sub-oceanic mantle metasomatized to various extents by an OIB-type
887 chemical component. The chemical difference between different Groups of basalts
888 are related to a combination of different extents of metasomatic enrichment and
889 different melting conditions (i.e., partial melting degrees and melting depths).

890 Our new data compared to literature data allow us to conclude that the different
891 volcano-sedimentary successions of the Durkan Complex record portions of seamounts of
892 different ages formed during both shallow-water shield stage (Cenomanian) and deep-
893 water stage (Coniacian-Campanian). The age, composition, and evolution of these distinct
894 seamounts in the Makran sector of the Neo-Tethys is compatible with regional-scale
895 evidence (from Caucasus to Himalaya), which suggest that abundant transitional and
896 alkaline basalts were erupted as a consequence of the interaction between the sub-oceanic
897 lithosphere and significant mantle plume activity.

898
899
900
901
902
903
904
905
906
907
908
909
910
911
912
913
914
915
916
917
918
919
920
921

Acknowledgment

The research has been funded by: Darius Project (Head M. Marroni), PRA project of the Pisa University (Head S. Rocchi), IGG-CNR, FAR-2018 Project of the Ferrara University (Head E.S.). R. Tassinari and R. Tamoni (University of Ferrara) are acknowledged for technical support with chemical analyses and with thin section production, respectively. Mr. Ahmad Behboodi is sincerely thanked for his appreciated assistance in organizing field work, and PhD student Ahmad Nateghpour from Kharazmi University is thanked for his help during field work. Constructive and thorough reviews for the Journal by two anonymous reviewers, as well as valuable suggestions by the Editor G. Shellnutt have helped us improve the science and organization presented in the paper.

References

922 Allahyari, K., Saccani, E., Rahimzadeh, B., Zeda, O., 2014. Mineral chemistry and petrology
923 of highly magnesian ultramafic cumulates from the Sarve-Abad (Sawlava) ophiolites
924 (Kurdistan, NW Iran): New evidence for boninitic magmatism in intra-oceanic fore-arc
925 setting in the Neo-Tethys between Arabia and Iran. *Journal of Asian Earth Sciences* 79,
926 312–328, doi: 10.1016/j.jseaes.2013.10.005.

927 Allègre, C.J., Minster, J.F., 1978. Quantitative models of trace element behavior in magmatic
928 processes. *Earth Planet. Sci. Lett.* 38, 1-25.

929 Bagheri, S., Stampfli, G., 2008, The Anarak, Jandaq and Posht-e-Badam metamorphic
930 complexes in central Iran: New geological data, relationships and tectonic implications.
931 *Tectonophysics* 451, p. 123–155. <https://doi.org/10.1016/j.tecto.2007.11.047>.

932 Barbero, E., Delavari, M., Dolati, A., Saccani, E., Marroni, M., Catanzariti, R., Pandolfi, L.,
933 2020a. The Ganj Complex reinterpreted as a Late Cretaceous volcanic arc: Implications
934 for the geodynamic evolution of the North Makran domain (southeast Iran). *Journal of*
935 *Asian Earth Science*, <https://doi.org/10.1016/j.jseaes.2020.104306>.

936 Barbero, E., Delavari, M., Dolati, A., Vahedi, L., Langone, A., Marroni, M., Pandolfi, L.,
937 Zaccarini, F., Saccani, E., 2020b. Early Cretaceous Plume–Ridge Interaction Recorded
938 in the Band-e-Zeyarat Ophiolite (North Makran, Iran): New Constraints from
939 Petrological, Mineral Chemistry, and Geochronological Data. *Minerals* 10, 1100,
940 doi:10.3390/min10121100.

941 Barbero, E., Festa, A., Saccani, E., Catanzariti, R., D’Onofrio, R., 2020c. Redefinition of the
942 Ligurian Units at the Alps–Apennines junction (NW Italy) and their role in the evolution
943 of the Ligurian accretionary wedge: constraints from mélanges and broken formations.
944 *Journal of the Geological Society of London* 177, 562–574,
945 <https://doi.org/10.1144/jgs2019-022>.

946 Barbero, E., Pandolfi, L., Delavari, M., Dolati, A., Saccani, E., Catanzariti, R., Lucani, V.,
947 Chiari, M., Marroni, M., 2021. The western Durkan Complex (Makran Accretionary
948 Prism, SE Iran): A Late Cretaceous tectonically disrupted seamounts chain and its role
949 in controlling deformation style. *Geoscience Frontiers* 12,
950 <https://doi.org/10.1016/j.gsf.2020.12.001>.

951 Barrier, E., Vrielynck, B., Brouillet, J.F., Brunet, M.F., 2018. Paleotectonic Reconstruction of
952 the Central Tethyan Realm. Tectonono-Sedimentary-Palinspastic maps from Late
953 Permian to Pliocene. Atlas of 20 maps (scale: 1:15.000.000). CCGM/CGMW, Paris,
954 <http://www.ccgm.org>.

955 Beccaluva, L., Macciotta, G., Piccardo, G.B., Zeda, O., 1989. Clinopyroxene compositions of
956 ophiolite basalts as petrogenetic indicator. *Chemical Geology* 77, 165-182.

957 Bonnet, G., Agard, P., Angiboust, S., Monié, P., Fournier, M., Caron, B., Omrani, J., 2020.
958 Structure and metamorphism of a subducted seamount (Zagros suture, Southern Iran).
959 *Geosphere*, 16, 62–81. <https://doi.org/10.1130/GES02134.1>

960 Bortolotti, V., Chiari, M., Goncuoglu, M.C., Principi, G., Saccani, E., Tekin, U.K., Tassinari,
961 R., 2017. The Jurassic–Early Cretaceous basalt–chert association in the ophiolites of the
962 Ankara Mélange, east of Ankara, Turkey: age and geochemistry. *Geological Magazine*
963 155, 451-478, doi: <https://doi.org/10.1017/S0016756817000401>.

964 Burg, J.-P., 2018. Geology of the onshore Makran accretionary wedge: Synthesis and tectonic
965 interpretation. *Earth Science Reviews* 185, 1210-1231,
966 <https://doi.org/10.1016/j.earscirev.2018.09.011>.

967 Burg, J.-P., Bernoulli, D., Smit, J., Dolati, A., Bahroudi, A., 2008. A giant catastrophic mud-
968 and-debris flow in the Miocene Makran. *Terra Nova* 20, 188-193.

969 Burg, J.-P., Dolati, A., Bernoulli, D., Smit, J., 2013. Structural style of the Makran tertiary
970 accretionary complex in SE Iran. In: Al Hosani, K., Roure, F., Ellison, R., Lokier, S.

971 (Eds.), *Lithosphere Dynamics and Sedimentary Basins: The Arabian Plate and*
972 *Analogues*. *Frontiers in Earth Sciences* vol.5. Springer, Berlin, Heidelberg, pp. 239-259.

973 Chauvet, F., Lapierre, H., Maury, R.C., Bosch, D., Basile, C., Cotten, J., Brunet, P., Campillo,
974 S., 2011. Triassic alkaline magmatism of the Hawasina Nappes: Post-breakup melting of
975 the Oman lithospheric mantle modified by the Permian Neotethyan Plume. *Lithos* 122,
976 122-136.

977 Delavari, M., Dolati, A., Marroni, M., Pandolfi, L., Saccani E., 2016. Association of MORB
978 and SSZ ophiolites along the shear zone between Coloured Mélange and Bajgan
979 Complexes (North Maran, Iran): Evidence from the Sorkhband area. *Ofioliti* 41, 21-34.

980 Dercourt, J., Zonenshian, L.P., Ricou, L.E., Kazmin, V.G., LePichon, X., Knipper, A.L.,
981 Grandjacquet, C., Sbertshikov, M., Geysant, J., Lepvrier, C., Pechersky, D.H., Boulin,
982 J., Sibuet, J.C., Savostin, L.A., Sorokhtin, O., Westphal, M., Bazhenov, M.L., Lauer,
983 J.P., Biju-Duval, B., 1986. Geological evolution of the Tethys Belt from the Atlantic to
984 the Pamir since the Lias. *Tectonophysics* 123, 241-315.

985 Dilek, Y., Furnes, H., 2011. Ophiolite genesis and global tectonics: geochemical and tectonic
986 fingerprinting of ancient oceanic lithosphere. *Geological Society of America Bulletin*
987 123, 387-411.

988 Dolati, A., Burg, J.-P., 2013. Preliminary fault analysis and paleostress evolution in the
989 Makran Fold-and-Thrust Belt in Iran. In: Al Hosani, K., Roure, F., Ellison, R., Lokier,
990 S. (Eds.), *Lithosphere Dynamics and Sedimentary Basins: The Arabian Plate and*
991 *Analogues*. *Frontiers in Earth Sciences*, Springer, Heidelberg, pp. 261–277.
992 https://doi.org/10.1007/978-3-642-30609-9_13

993 Dolati, A., 2010. *Stratigraphy, Structure Geology and Low-temperature Thermochronology*
994 *Across the Makran Accretionary Wedge in Iran*. (PhD Thesis). ETH Zurich, pp. 165.

995 Dorani, M., Arvin, M., Oberhänsli, R., Dargahi, S., 2017. P-T evolution of metapelites from
996 the Bajgan complex in the Makran accretionary prism, south eastern Iran. *Geochemistry*
997 77, 459–475. <https://doi.org/10.1016/j.chemer.2017.07.004>.

998 Droop, G.T.R., 1987. A general equation for estimating Fe³⁺ concentrations in
999 ferromagnesian silicates and oxides from microprobe analyses, using stoichiometric
1000 criteria. *Mineralogical Magazine* 51, 431–435.

1001 Eftekhar-Nezhad, J., Arshadi, S., Mahdavi, M.A., Morgan, K.H., McCall, G.J.H., Huber, H.,
1002 1979. Fannuj Quadrangle Map 1:250000. Tehran: Ministry of Mines and Metal,
1003 Geological Survey of Iran.

1004 Esmaeili, R., Xiao, W., Ebrahimi, M., Zhang, J.E., Zhang, Z., El-Rahman, Y.A., Han, C.,
1005 Wan, B., Ao, S., Song, D., Shahabi, S., Aouizerat, A., 2019. Makran ophiolitic basalts
1006 (SE Iran) record Late Cretaceous Neotethys plume-ridge interaction. *International*
1007 *Geology Review*, doi: 10.1080/00206814.2019.1658232.

1008 Ghazi, A.M., Hassanipak, A.A., Mahoney, J.J., Duncon R.A., 2004. Geochemical
1009 characteristics, ⁴⁰Ar-³⁹Ar ages and original tectonic setting of the Band-e-Zeyarat/Dar
1010 Anar ophiolite, Makran accretionary Prism, S.E. Iran. *Tectonophysics* 193, 175-196.

1011 Gradstein, F.M., Ogg, J.G., Scmitz, M.D., Ogg G.M., 2012. *The Geologic Time Scheme*.
1012 Elsevier, Amsterdam, International Commission on Stratigraphy, pp.1144.

1013 Haase, K.M., Devey, C.W., 1996. Geochemistry of lavas from the Ahu and Tupa volcanic
1014 fields, Easter Hotspot, southeast Pacific: Implications for magma genesis near a
1015 spreading axis. *Earth and Planetary Science Letters* 137, 129-143.

1016 Hanan, B. B., Blichert-Toft, J., Kingsley, R., Schilling, J.-G., 2000. Depleted Iceland mantle
1017 plume geochemical signature: Artifact of multicomponent mixing? *Geochemistry,*
1018 *Geophysics, Geosystems*, 1(4), <https://doi.org/10.1029/1999GC000009>

1019 Hässig, M., Rolland, Y., Sosson, M., Galoyan, G., Sahakyan, L., Topuz, G., Çelik, Ö.F.,
1020 Avagyan, A., Müller, C., 2013. Linking the NE Anatolian and Lesser Caucasus
1021 ophiolites: evidence for large-scale obduction of oceanic crust and implications for the
1022 formation of the Lesser Caucasus-Pontides Arc. *Geodinamica Acta* 26, 311–330,
1023 <https://doi.org/10.1080/09853111.2013.877236>

1024 Hunziker, D., Burg, J.-P., Bouilhol, P., von Quadt, A., 2015. Jurassic rifting at the Eurasian
1025 Tethys margin: Geochemical and geochronological constraints from granitoids of North
1026 Makran, southeastern Iran. *Tectonics* 34, 571-593.

1027 Isozaki, Y., Maruyama, S., Furuoka, F., 1990. Accreted oceanic materials in Japan.
1028 *Tectonophysics*, 181, 179–205. [https://doi.org/10.1016/0040-1951\(90\)90016-2](https://doi.org/10.1016/0040-1951(90)90016-2)

1029 Janney, P.E., Le Roex, A.P., Carlson, R.L., 2005. Hafnium isotope and trace element
1030 constraints on the nature of mantle heterogeneity beneath the Central Southwest Indian
1031 Ridge. *Journal of Petrology* 46, 2427-2464.

1032 Kerr, A.C., 2014. Oceanic Plateaus. In: Holland, H.D., Turekian, K.K. (Eds.), *Treatise on*
1033 *Geochemistry*, Second edition vol. 4, Elsevier, Oxford, pp. 631–667.

1034 Khan, S.R., Jan, M.Q., Khan, T., Khan, A.M., 2007. Petrology of the dykes from the
1035 Waziristan Ophiolite, NW Pakistan, *Journal of Asian Earth Sciences* 29, 369-377, doi:
1036 [10.1016/j.jseaes.2006.08.001](https://doi.org/10.1016/j.jseaes.2006.08.001)

1037 Kopp, C., Fruehn, J., Flueh, E.R., Reichert, C., Kukowski, N., Bialas, J., Klaeschen, D., 2000.
1038 Structure of the Makran subduction zone from wide-angle and reflection seismic data.
1039 *Tectonophysics* 329, 171–191, [https://doi.org/10.1016/S0040-1951\(00\)00195-5](https://doi.org/10.1016/S0040-1951(00)00195-5)

1040 Lachance, G.R., Trail, R.J., 1966. Practical solution to the matrix problem in X-ray analysis.
1041 *Canadian Spectroscopy* 11, 43-48.

1042 LeRoex, A.P., Dick, H.J.B., Erlank, A.J., Reid, A.M., Frey, F.A., Hart, S.R., 1983.
1043 *Geochemistry, Mineralogy and Petrogenesis of Lavas Erupted along the Southwest*

1044 Indian Ridge Between the Bouvet Triple Junction and 11 degrees East. *Journal of*
1045 *Petrology* 24, 267-318.

1046 Leterrier, J., Maury, R.C., Thonon, P., Girard, D., Marchal, M., 1982. Clinopyroxene
1047 composition as a method of identification of the magmatic affinities of paleo-volcanic
1048 series. *Earth and Planetary Science Letters* 59, 139-154.

1049 Lustrino, M., Melluso, L., Morra, V., 2002. The transition from alkaline to tholeiitic magmas:
1050 a case study from the Orosei-Dorgali Pliocene volcanic district (NE Sardinia, Italy).
1051 *Lithos* 63, 83–113.

1052 McCall, G.J.H., 1985. Explanatory text of the Minab Quadrangle Map; 1:250,000; No. J13.
1053 Geological Survey of Iran, Tehran, pp. 530.

1054 McCall, G.J.H., 2002. A summary of the geology of the Iranian Makran. *The Tectonic and*
1055 *Climatic Evolution of the Arabian Sea Region*. In: Clift, P.D., Kroon, D., Gaedicke, C.,
1056 Craig, J. (Eds.), *Geological Society of London Special Publications* 195, 147-204.

1057 McCall, G.J.H., Kidd, R.G.W., 1982. The Makran southeastern Iran: the anatomy of a
1058 convergent margin active from Cretaceous to present. In: Leggett, J.K. (Ed.), *Trench-*
1059 *forearc geology: sedimentation and tectonics of modern and ancient plate margins*. Vol
1060 10, 387-397.

1061 Mohammadi, A., Burg, J.-P., Winkler, W., Ruh, J., von Quadt, A., 2016. Detrital zircon and
1062 provenance analysis of Late Cretaceous–Miocene onshore Iranian Makran strata:
1063 Implications for the tectonic setting. *Geological Society of America Bulletin* 128, 1481–
1064 1499. <https://doi.org/10.1130/B31361.1>

1065 Monsef, I., Rahgoshay, M., Pirouz, M., Chiaradia, M., Grégoire, M., Ceuleneer, G., 2019. The
1066 Eastern Makran Ophiolite (SE Iran): evidence for a Late Cretaceous fore-arc oceanic
1067 crust. *International Geology Review*, 61, 1313–1339.
1068 <https://doi.org/10.1080/00206814.2018.1507764>.

1069 Moore, J.G., 1970. Water Content of Basalt Erupted on the ocean floor. Contribution to
1070 Mineralogy and Petrology 28, 272–279, <https://doi.org/10.1007/BF00388949>.

1071 Moore, J.G., Schilling, J.G., 1973. Vesicles, water, and sulfur in Reykjanes Ridge basalts.
1072 Contribution to Mineralogy and Petrology 41, 105–118.
1073 <https://doi.org/10.1007/BF00375036>

1074 Moore, J.G., Clague, D.A., 1992. Volcano growth and evolution of the island of Hawaii.
1075 Geological Society of America Bulletin 104, 1471–1484. [https://doi.org/10.1130/0016-](https://doi.org/10.1130/0016-7606(1992)104<1471:VGAEOT>2.3.CO;2)
1076 [7606\(1992\)104<1471:VGAEOT>2.3.CO;2](https://doi.org/10.1130/0016-7606(1992)104<1471:VGAEOT>2.3.CO;2)

1077 Moslempour, M.E., Khalatbari-Jafari, M., Ghaderi, M., 2015. Petrology, Geochemistry and
1078 Tectonics of the Extrusive Sequence of Fannuj-Maskutan Ophiolite, Southeastern Iran.
1079 Journal Geological Society of India 85, 604-618.

1080 Omrani, H., Moazzen, M., Oberhänsli, R., Moslempour, M.E., 2017. Iranshahr blueschist:
1081 subduction of the inner Makran oceanic crust. Journal of Metamorphic Geology 35,
1082 373-392.

1083 Pearce J.A., 1996. A user's guide to basalt discrimination diagrams. In: Bailes, A.H.,
1084 Christiansen, E.H., Galley, A.G., Jenner, G.A., Keith, J.D., Kerrich, R., Lentz, D.R.,
1085 Leshner, C.M., Lucas, S.B., Ludden, J.N., Pearce, J.A., Peloquin, S.A., Stern, R.A.,
1086 Stone, W.E., Syme, E.C., Swinden, H.S., Wyman, D.A. (Eds.), Trace element
1087 geochemistry of volcanic rocks: applications for massive sulphide exploration. Short
1088 Course Notes. Geological Association of Canada 12, 79-113.

1089 Pearce, J.A., 2008. Geochemical fingerprinting of oceanic basalts with applications to
1090 ophiolite classification and the search for Archean oceanic crust. Lithos 100, 14–48,
1091 <https://doi.org/10.1016/j.lithos.2007.06.016>.

1092 Pearce, J.A., Norry, M.J., 1979. Petrogenetic implications of Ti, Zr, Y, and Nb variations in
1093 volcanic rocks. Contributions to Mineralogy and Petrology 69, 33-47.

- 1094 Pirnia, T., Saccani, E., Torabi, G., Chiari, M., Gorican, S., Barbero, E., 2020. Cretaceous
1095 tectonic evolution of the Neo-Tethys in Central Iran: Evidence from petrology and age
1096 of the Nain-Ashin ophiolitic basalts. *Geoscience Frontiers*, 11, 57–81,
1097 <https://doi.org/10.1016/j.gsf.2019.02.008>
- 1098 Platt, J.P., Leggett, J.K., Young, J., Raza, H., Alam, S., 1985. Large-scale sediment
1099 underplating in the Makran accretionary prism, southwest Pakistan. *Geology* 13, 507,
1100 [https://doi.org/10.1130/0091-7613\(1985\)13<507:LSUITM>2.0.CO;2](https://doi.org/10.1130/0091-7613(1985)13<507:LSUITM>2.0.CO;2)
- 1101 Regelous, M., Hofmann, A.W., Abouchami W., Galer, S.J.G., 2003. Geochemistry of Lavas
1102 from the Emperor Seamounts, and the Geochemical Evolution of Hawaiian Magmatism
1103 from 85 to 42 Ma. *Journal of Petrology* 44, 113–140,
1104 <https://doi.org/10.1093/petrology/44.1.113>.
- 1105 Riaz, M.S., Bin, S., Naeem, S., Kai, W., Xie, Z., Gilani, S.M.M., Ashraf, U., 2019. Over 100
1106 years of faults interaction, stress accumulation, and creeping implications, on Chaman
1107 Fault System, Pakistan. *International Journal of Earth Sciences* 108, 1351–1359,
1108 <https://doi.org/10.1007/s00531-019-01710-0>.
- 1109 Robertson, A.H.F., 2007. Overview of tectonic settings related to the rifting and opening of
1110 Mesozoic ocean basins in the Eastern Tethys: Oman, Himalayas and Eastern
1111 Mediterranean regions. *Geological Society of London Special Publications* 282, 325–
1112 388, <https://doi.org/10.1144/SP282.15>.
- 1113 Rolland, Y., Galoyan, G., Sosson, M., Melkonyan, R., Avagyan, A., 2010. The Armenian
1114 Ophiolite: insights for Jurassic back-arc formation, Lower Cretaceous hot spot
1115 magmatism and Upper Cretaceous obduction over the South Armenian Block.
1116 *Geological Society of London Special Publications* 340, 353–382,
1117 <https://doi.org/10.1144/SP340.15>.

1118 Rolland, Y., Hässig, M., Bosch, D., Bruguier, O., Melis, R., Galoyan, G., Topuz, G.,
1119 Sahakyan, L., Avagyan, A., Sosson, M., 2020. The East Anatolia–Lesser Caucasus
1120 ophiolite: An exceptional case of large-scale obduction, synthesis of data and numerical
1121 modelling. *Geoscience Frontiers* 11, 83–108, <https://doi.org/10.1016/j.gsf.2018.12.009>.

1122 Saccani, E., Allahyari, K., Beccaluva, L., Bianchini, G., 2013. Geochemistry and petrology of
1123 the Kermanshah ophiolites (Iran): Implication for the interaction between passive
1124 rifting, oceanic accretion, and OIB-type components in the Southern Neo-Tethys Ocean.
1125 *Gondwana Research* 24, 392–411, <https://doi.org/10.1016/j.gr.2012.10.009>.

1126 Saccani, E., 2015. A new method of discriminating different types of post-Archean ophiolitic
1127 basalts and their tectonic significance using Th-Nb and Ce-Dy-Yb systematics.
1128 *Geoscience Frontiers* 6, 481-501.

1129 Saccani, E., Delavari, M., Dolati, A., Marroni, M., Pandolfi, L., Chiari, M., Barbero E., 2018.
1130 New insights into the geodynamics of Neo-Tethys in the Makran area: Evidence from
1131 age and petrology of ophiolites from the Coloured Mélange Complex (SE Iran).
1132 *Gondwana Research* 62, 306-327.

1133 Safonova, I., 2008. Geochemical Evolution of Intraplate Magmatism in the Paleo-Asian
1134 Ocean from the Late Neoproterozoic to the Early Cambrian. *Petrology* 16, 492-511.

1135 Safonova, I., 2017. Juvenile versus recycled crust in the Central Asian Orogenic Belt:
1136 Implications from ocean plate stratigraphy, blueschist belts and intra-oceanic arcs.
1137 *Gondwana Research* 47, 6-27, <http://dx.doi.org/10.1016/j.gr.2016.09.003>.

1138 Safonova, I.Y., Santosh, M., 2014. Accretionary complexes in the Asia-Pacific region:
1139 Tracing archives of ocean plate stratigraphy and tracking mantle plumes. *Gondwana*
1140 *Research* 25, 126–158, <https://doi.org/10.1016/j.gr.2012.10.008>.

1141 Safonova, I., Maruyama, S., Kojima, S., Komiya, T., Krivonogov, S., Koshida, K., 2016.
1142 Recognizing OIB and MORB in accretionary complexes: A new approach based on

1143 ocean plate stratigraphy, petrology and geochemistry. *Gondwana Research* 33, 92–114,
1144 <https://doi.org/10.1016/j.gr.2015.06.013>.

1145 Samimi Namin, M., 1982. Geological Map of Taherui 1:250000 Scale. Tehran: Ministry of
1146 Mines and Metal, Geological Survey of Iran.

1147 Samimi Namin, M., 1983. Geological Map of Minab 1:250000 Scale. Tehran: Ministry of
1148 Mines and Metal, Geological Survey of Iran.

1149 Sepidbar, F., Lucci, F., Biabangard, H., Zaki Khedr, M., Jiantang, P., 2020. Geochemistry and
1150 tectonic significance of the Fannuj-Maskutan SSZ-type ophiolite (Inner Makran, SE
1151 Iran). *International Geology Review*, <https://doi.org/10.1080/00206814.2020.1753118>

1152 Shervais, J.W., 1982. Ti-V plots and the petrogenesis of modern and ophiolitic lavas. *Earth
1153 and Planetary Science Letters* 59, 101–118, [https://doi.org/10.1016/0012-](https://doi.org/10.1016/0012-821X(82)90120-0)
1154 [821X\(82\)90120-0](https://doi.org/10.1016/0012-821X(82)90120-0).

1155 Sun, S.S., McDonough, W.F., 1989. Chemical and isotopic systematics of oceanic basalts:
1156 implications for mantle composition and processes. In: Saunders, A.D., Norry, M.J.
1157 (Eds.), *Magmatism in the Ocean Basins*. Geological Society of London Special
1158 Publication 42, 313-345.

1159 Yang, G.X., Li, Y.J., Xiao, W.J., Tong, L.L., 2015. OIB-type rocks within West Junggar ophiolitic
1160 mélanges: evidence for the accretion of seamounts. *Earth-Science Reviews* 150, 477-496,
1161 <http://dx.doi.org/10.1016/j.earscirev.2015.09.002>.

1162 Yang G.X., Li Y.J., Tong L.L., Wang Z.P., Duan, F.H., Xu, Q., Li, H., 2019. An overview of oceanic
1163 island basalts in accretionary complexes and seamounts accretion in the western Central Asian
1164 Orogenic Belt. *Journal of Asian Earth Sciences* 179, 385-398.

1165 Wan, B., Wang, X., Liu, X., Cai, K., Xiao, W., Mitchell, R.N., 2020. Long-lived seamount subduction
1166 in ancient orogens: Evidence from the Paleozoic South Tianshan. *Geology*.
1167 <https://doi.org/10.1130/G48547.1>

1168 White, W.M., 2010. Oceanic Island Basalts and Mantle Plumes: The Geochemical
1169 Perspective. *Annual Review of Earth and Planetary Sciences* 38, 133–160,
1170 <https://doi.org/10.1146/annurev-earth-040809-152450>.
1171 Winchester, J.A., Floyd, P.A., 1977. Geochemical discrimination of different magma series
1172 and their differentiation products using immobile elements. *Chemical Geology* 20, 325-
1173 343.
1174 Workman, R.K., Hart, S.R., 2005. Major and trace element composition of the depleted
1175 MORB mantle (DMM). *Earth and Planetary Science Letters* 231, 53-72.

1176

1177

1178

1179

1180

1181

1182

1183 **Table captions**

1184

1185 **Table 1.** Major (wt.%) and trace (ppm) element composition of representative volcanic
1186 and metavolcanic rocks from the western part of the Durkan Complex. Abbreviations: bas:
1187 basalt; bas and: basaltic andesite; tra: trachyte; a-rhy: alkali-rhyolite; XRF: X-ray
1188 fluorescence spectrometry; ICP-MS: inductively coupled plasma-mass spectrometry; n.d.:
1189 not detected. $Mg\# = 100 \times MgO / (MgO + FeO)$. $Fe_2O_3 = 0.15 \times FeO$. Normalizing values
1190 for REE ratios from [Sun and McDonough \(1989\)](#). Asterisks indicate samples whose XRF
1191 composition is taken from [Barbero et al. \(2021\)](#).

1192

1193 **Table 2.** Representative analyses of clinopyroxene from basaltic and metabasaltic
1194 rocks from the western part of the Durkan Complex. Atoms per formula units (a.p.f.u.) are
1195 calculated on the bases of four cations. The compositions of Fe³⁺ and Fe²⁺ were calculated
1196 from the measured total FeO according to [Droop \(1987\)](#); $Mg\# = Mg / (Mg + Fe^{2+})$.
1197 Abbreviations, Wo: wollastonite; En: enstatite; Fs: ferrosilite; Acm: Acmite.
1198 Abbreviations, c: core; ec: external part of the core; r: rim.

1199

1200 **Figure caption**

1201

1202 **Figure 1.** a) Simplified tectonic sketch map of the Iranian-Afghan-Pakistani area
1203 (modified from [Khan et al., 2007](#); [Bagheri and Stampfli, 2008](#); [Allahyari et al., 2014](#);
1204 [Mohammadi et al., 2016](#); [Pirnia et al., 2020](#); [Barbero et al., 2020b](#)); b) structural sketch
1205 map showing the different tectono-stratigraphic domains of the Makran Accretionary
1206 Wedge (modified from [Burg et al., 2013](#)); c) simplified geological-structural map of the
1207 North Makran Domain showing the different tectonic units (modified from [Eftekhari-](#)
1208 [Nezhad et al. 1979](#); [Burg, 2018](#); [Samimi Namin, 1982, 1983](#); [Barbero et al., 2020b](#)).

1209

1210 **Figure 2.** Simplified geological map of the western part of the Durkan Complex
1211 (based on [Samimi Namin, 1982](#) and modified according to our original fieldwork and
1212 photointerpretation with satellite images). The locations of the sampled areas are also
1213 shown.

1214

1215 **Figure 3.** a) Schematic stratigraphic column and ages for the three different types of
1216 successions in the western part of the Durkan Complex; b) vesicle volume % vs. depth of
1217 eruption for basalts from the different successions. The different curves indicate the depth-

1218 vesicles percent for tholeiitic (solid line, from [Moore and Schilling, 1973](#)) and alkaline
1219 (dashed line, from [Moore, 1970](#)) volcanic rocks. Modified from [Barbero et al., \(2021\)](#).

1220

1221

1222 **Figure 4.** Nb/Y vs. Zr/Ti discrimination diagram of [Winchester and Floyd \(1977\)](#)

1223 modified by [Pearce \(1996\)](#) for volcanic and metavolcanic rocks from the western part of
1224 the Durkan Complex.

1225

1226 **Figure 5.** N-MORB normalized incompatible element patterns (left column) and

1227 Chondrite-normalized rare earth element patterns (right column) for volcanic and

1228 metavolcanic rocks from the part of the Durkan Complex. Normalizing values are from

1229 [Sun and McDonough \(1989\)](#). Compositions of average plume-influenced mid-ocean ridge

1230 basalt (P-MORB) from the Southwest Indian Ridge and typical alkaline oceanic within-

1231 plate basalt (OIB) are from [Janney et al. \(2005\)](#) and [Sun and McDonough \(1989\)](#),

1232 respectively.

1233

1234 **Figure 6.** Chondrite-normalized $(\text{Sm}/\text{Yb})_N$ vs. $(\text{La}/\text{Yb})_N$ (a), $(\text{Sm}/\text{Yb})_N$ vs. $(\text{Sm}/\text{Dy})_N$

1235 (b), and $(\text{La}/\text{Yb})_N$ vs. Yb_N (c) diagrams for the volcanic and metavolcanic rocks of the

1236 western part of the Durkan Complex. Normalizing values are from [Sun and McDonough](#)

1237 [\(1989\)](#).

1238

1239 **Figure 7.** N-MORB normalized Th vs. Nb discrimination diagram of [Saccani \(2015\)](#)

1240 for volcanic and metavolcanic rocks from the western part of the Durkan Complex.

1241 Vectors indicate the trends of compositional variations due to the main petrogenetic

1242 processes. Abbreviations, AFC: assimilation-fractional crystallization; OIB-CE: ocean

1243 island-type (plume-type) component enrichment; FC: fractional crystallization; MORB:
1244 mid-ocean ridge basalt; N-: normal type; E-: enriched type; P-: plume type; D-: depleted
1245 type; IAT: island arc tholeiite; CAB: calc-alkaline basalt; AB: alkaline oceanic within-
1246 plate basalt; MTB: medium titanium basalt. Normalizing values, as well as the composition
1247 of typical N-MORB (white star), E-MORB (grey star), and OIB (black star) are from [Sun](#)
1248 [and McDonough \(1989\)](#).

1249
1250 **Figure 8.** Diagram showing the variation of TiO_2 , CaO , and Na_2O contents vs. Mg#
1251 for clinopyroxenes from the basaltic and metabasaltic rocks of the western part of the
1252 Durkan Complex. Arrows represent the average trends of variation for clinopyroxene from
1253 the different geochemical groups of rocks.

1254
1255 **Figure 9.** a) Ti vs. (Ca + Na) and b) (Ti + Cr) vs. Ca discrimination diagrams of
1256 [Leterrier et al. \(1982\)](#) showing the compositions of clinopyroxenes from the volcanic and
1257 metavolcanic rocks from the western the part of the Durkan Complex.

1258
1259 **Figure 10.** Compositions of clinopyroxenes from the basaltic and metabasaltic rocks
1260 from the western the part of the Durkan Complex plotted in the $\text{TiO}_2\text{--Na}_2\text{O--SiO}_2/100$
1261 diagram for discriminating clinopyroxenes in basalts from different oceanic settings
1262 ([Beccaluva et al., 1989](#)). Abbreviations, E-MORB: enriched mid-ocean ridge basalt; N-
1263 MORB: normal mid-ocean ridge basalt; WOPB: within oceanic plate basalts; ICB: Iceland
1264 basalts; and SSZ: supra-subduction zone basalts.

1265
1266 **Figure 11.** Variation of TiO_2 (a), CaO (b), and Al_2O_3 (c) contents in clinopyroxenes
1267 from basaltic and metabasaltic rocks from the western the part of the Durkan Complex vs.

1268 the Nb/Y ratios of their hosting rocks. Only clinopyroxene with Mg# in the range 0.74 –
1269 0.80 are plotted to allow comparison between the different chemical groups.

1270

1271 **Figure 12.** a) Nb vs. Zr and b) Zr/Y vs. Zr/Nb diagrams for volcanic and metavolcanic
1272 rocks from the western part of the Durkan Complex. N-MORB, E-MORB and OIB end-
1273 members are from [Sun and McDonough \(1989\)](#). Fields showing the compositional
1274 variation of different types of basalts from subduction-unrelated ophiolites and modern
1275 oceanic setting are shown for comparison in Panel b) (data from [Saccani et al., 2013](#), [Le
1276 Roex et al., 1983](#); [Hanan et al., 2000](#); [Chauvet et al., 2011](#)). The dashed line in b)
1277 represents the mixing curve calculated using OIB and N-MORB end-members (from [Le
1278 Roex et al. 1983](#)).

1279

1280 **Figure 13.** a) Nb/Yb vs. TiO₂/Yb diagram showing the isobaric melting curves for
1281 theoretical mantle sources S1 and S2 calculated for different pressures according to [Pearce
1282 \(2008\)](#); b) Nb/Yb vs. Th batch melting curve for the theoretical mantle source S1 and S2
1283 calculated for both spinel- and garnet-facies conditions. The dashed line represents the
1284 mixing line of various melt fractions from garnet- and spinel-facies mantle. S1 and S2
1285 represent theoretical mantle sources calculated by assuming different degrees of
1286 enrichment by an OIB-type chemical component ([Lustrino et al., 2002](#)) of a sub-oceanic
1287 slightly depleted lherzolite residual after small volume of MORB melt extraction
1288 (lherzolite ZB2, [Barbero et al., 2020c](#)). Depleted MORB mantle (DMM) and primitive
1289 mantle (PM) compositions are also shown in [Figure 13a](#) (data from [Workman and Hart,
1290 2005](#) and [Sun and McDonough, 1989](#), respectively). Input parameters (source modes,
1291 melting proportions, and partition coefficients, source compositions) for the model in
1292 [Figure 13b](#) are given in [Supplementary Table S2](#). Volcanic and metavolcanic rocks from

1293 the western part of the Durkan Complex are plotted in both diagrams. The relatively less
1294 fractionated basalts of each rock type are shown with large symbols, whereas other
1295 samples are shown with small, grey symbols.

1296

1297 **Figure 14.** Calculated chondrite-normalized (Sun and McDonough, 1989) rare earth
1298 element (REE) liquid composition for parental melts derived from mantle sources S1 and
1299 S2, assuming various degrees of non-modal batch partial melting in the spinel- and garnet-
1300 facies mantle, as well as different proportions of melt fractions from garnet- and spinel-
1301 facies mantle. S1 and S2 represent theoretical mantle sources calculated by assuming
1302 different degrees of enrichment by an OIB-type chemical component (Lustrino et al., 2002)
1303 of a sub-oceanic slightly depleted lherzolite residual after small volume of MORB melt
1304 extraction (lherzolite ZB2, Barbero et al., 2020c). Abbreviations: EM: enriched mantle
1305 source (from Lustrino et al., 2002); DMM: depleted MORB mantle (Workman and Hart,
1306 2005). Input parameters for the REE models (source modes, melting proportions, and
1307 partition coefficients), as well as compositions of the different mantle sources are shown in
1308 Supplementary Table S2. The comparison between the composition of the relatively less
1309 fractionated basalts of Group 1, Group 2a, and Group 2b and the calculated melts are
1310 shown in panels a), b), c), respectively. Representative examples of the mixing of various
1311 melt fractions from garnet- and spinel-facies mantle are shown in a1).

1312

1313 **Figure 15.** Conceptual cartoon showing the petrogenetic processes operating during
1314 the shallow-water (a) and deep-water (b) stages of growth of the Durkan seamounts. The
1315 depositional positions of the different types of successions within the seamount chain is
1316 modified from Barbero et al. (2021). Abbreviations, MORB: mid-oceanic ridge basalt;
1317 OIB: ocean island basalt; S1 and S2: enriched mantle sources derived from different

1318 degrees of enrichment by an OIB-type chemical component of a sub-oceanic slightly
1319 depleted lherzolite residual after small volume of MORB melt extraction; spl: spinel; gt:
1320 garnet.

1 New evidence for Late Cretaceous plume-related seamounts in the Middle East sector
2 of the Neo-Tethys: Constraints from geochemistry, petrology, and mineral chemistry of the
3 magmatic rocks from the western Durkan Complex (Makran Accretionary Prism, SE Iran)
4
5
6

7 Edoardo Barbero¹, Federica Zaccarini², Morteza Delavari³, Asghar Dolati³, Emilio
8 Saccani¹, Michele Marroni^{4,5}, Luca Pandolfi^{4,5}
9
10

11 1 Dipartimento di Fisica e Scienze della Terra, Università di Ferrara, 44123 Ferrara,
12 Italy; brbdrd@unife.it (E.B.); sac@unife.it (E.S.)

13 2 Department of Applied Geological Sciences and Geophysics, University of Leoben,
14 8700 Leoben, Austria; federica.zaccarini@unileoben.ac.at

15 3 Faculty of Earth Sciences, Kharazmi University, Tehran 15719-19911, Iran;
16 delavari@khu.ac.ir (M.D.); dolati@khu.ac.ir (A.D.)

17 4 Dipartimento di Scienze della Terra, Università di Pisa, 56126 Pisa, Italy;
18 luca.pandolfi@unipi.it (L.P.); michele.marroni@unipi.it (M.M.)

19 5 Istituto di Geoscienze e Georisorse, Consiglio Nazionale delle Ricerche (CNR),
20 56124 Pisa, Italy
21
22

23 * Corresponding author: Emilio Saccani (sac@unife.it)
24
25

26 Abstract

27 The Durkan Complex in the Makran Accretionary Prism (SE Iran) has been interpreted
28 either as a continental margin succession or a Late Cretaceous tectonically disrupted
29 seamount chain. New whole rock and clinopyroxene chemical data for basaltic and
30 metabasaltic rocks of the Durkan Complex allow us to distinguish two main rock groups:
31 a) rocks showing transitional chemical affinity (Group 1) and compositions resembling
32 those of plume-type mid-oceanic ridge basalts; b) rocks with within-plate oceanic island
33 basalt (OIB) compositions showing a clear alkaline affinity (Group 2). Based on whole
34 rock REE contents and clinopyroxene chemistry, alkaline rocks can be further subdivided
35 in two sub-groups, namely, the Group 2a and 2b. Compared to Group 2a, Group 2b rocks
36 show a more pronounced alkaline nature marked by higher whole rock La/Yb and Sm/Dy
37 ratios and higher TiO₂ and Na₂O contents in clinopyroxenes. Trace element and REE
38 petrogenetic models show that the Durkan basaltic rocks were generated from the partial
39 melting of depleted sub-oceanic mantle source that was metasomatized by OIB-type
40 chemical components in a within-plate oceanic setting. The chemical differences in the
41 three rock groups are related to different combinations of partial melting degree, depths of
42 melting, and various extent of enrichment of the mantle sources by OIB-type chemical
43 components, which are related, in turn, to a Late Cretaceous mantle plume activity in the
44 northern Neo-Tethys realm. We suggest that the Durkan Complex formed in a seamount
45 setting and that its different volcano-sedimentary successions record different stages of
46 seamount formation.

47
48 **Keywords:** Ophiolite, Geochemistry, Petrology, Clinopyroxene chemistry, Alkaline
49 basalt, Seamount, Makran Accretionary Prism, Iran

50

51

52 1. Introduction

53
54 Ophiolitic basaltic and metabasaltic rocks are widespread within collisional-type and
55 accretionary-type orogenic belts and are of particular importance, as their petrological
56 features are sensitive to different geodynamic settings of formation. Different tectonic
57 environments, such as mid-oceanic ridge, within-plate oceanic island, convergent and rifted
58 margins, are indeed characterized by the occurrence of chemically distinctive types of
59 basaltic rocks (Pearce, 1996; Dilek and Furnes, 2011; Saccani, 2015; Safonova et al., 2016).
60 Among them, basaltic rocks with oceanic island basalt (OIB) chemical affinity are of
61 particular interest as they may represent remnants of deformed oceanic seamounts (Yang et
62 al., 2015, 2019; Wan et al., 2020). Seamounts are largely subducted and their remnants in
63 the accretionary and collisional belts are represented only by blocks in ophiolitic mélanges
64 (e.g., Yang et al., 2019; Safonova et al., 2016) or as coherent slices underplated at different
65 depths (e.g., Isozaki et al., 1990; Bonnet et al., 2020). In addition, recognizing basalts with
66 OIB affinity within accretionary and collisional belts is particularly important as they likely
67 represent the only elements for reconstructing periods of mantle plume activity during Earth
68 history (Safonova and Santosh, 2014; Wan et al., 2020). It follows that detailed petrological
69 studies of basaltic rocks within the accretionary and collisional belts are fundamental for
70 constraining their tectono-magmatic settings of formation and, consequently, for
71 reconstructing the progressive geodynamic history of the paleo-oceanic basins and their
72 related continental margins (Robertson, 2007; Hässig et al., 2013; Safonova, 2017; Saccani
73 et al., 2018; Rolland et al., 2020).

74 The Makran Accretionary Prism (hereafter, simply Makran) in SE Iran and SW
75 Pakistan (Figs. 1a, b) is related to the long-lived geodynamic evolution of the Neo-Tethys
76 Ocean and its northern continental margin, represented by the Lut and Afghan blocks

77 (McCall and Kidd, 1982; Burg et al., 2008; 2013; Burg, 2018; Saccani et al., 2018; Monsef
78 et al., 2018; Barbero et al., 2020a). The Makran consists of several tectono-stratigraphic
79 domains (Fig. 1b) that have been deformed and incorporated in the accretionary prism,
80 starting from the Cretaceous (e.g., Platt et al., 1985; Dolati and Burg., 2013; Burg, 2018;
81 Saccani et al., 2018; Barbero et al., 2020a, b). Among these, the North Makran domain
82 records the pre-Eocene deformation history of the accretionary wedge. It consists of several
83 tectonic units (Fig. 1c) that, in turn, represent distinct tectonic domains, including the Neo-
84 Tethys oceanic lithosphere, seamounts and/or oceanic plateau, as well as arc-forearc-trench
85 domains. The North Makran also includes tectonic units derived from an exotic
86 microcontinental block and its sedimentary cover (McCall and Kidd, 1982; Dorani et al.,
87 2017; Burg, 2018; Monsef et al., 2018; Saccani et al., 2018). The Durkan Complex is one of
88 the major tectonic elements of the North Makran domain (Fig. 1c) and it was described as a
89 highly deformed complex including Early Cretaceous – early Paleocene shallow water
90 succession, abundant volcanic rocks, as well as subordinate tectonic slices of Carboniferous,
91 Permian and Jurassic shallow water sedimentary rocks and Middle - Late Jurassic granitoids
92 (McCall, 1985; Hunziker et al., 2015). It has been classically interpreted as the Permian –
93 Cretaceous disrupted sedimentary cover of the passive margin of a continental basement as
94 old as Paleozoic, whose remnants are now represented by the Bajgan Complex (McCall and
95 Kidd, 1982; McCall, 2002). The Bajgan-Durkan Complexes are collectively thought to
96 represent the remnants of a continental ribbon detached from the Eurasian margin by the
97 Late Jurassic – Early Cretaceous rifting that led to the opening of the North Makran Ocean
98 (McCall and Kidd, 1982; McCall, 2002; Hunziker et al., 2015; Burg, 2018). However,
99 Barbero et al. (2021) showed that the western Durkan Complex consists of tectonic slices
100 including volcano-sedimentary sequences, which represent remnants of a tectonically
101 disrupted Late Cretaceous seamounts chain. This interpretation, which is radically different

102 from the extant interpretation, is based on field investigations and detailed stratigraphic,
103 structural, and biochronological data, as well as preliminary petrographic and geochemical
104 data on volcanic rocks. However, a thorough geochemical and petrological investigations of
105 the volcanic rocks included in the Durkan volcano-sedimentary sequences is necessary for
106 better constraining the tectono-magmatic setting of formation of the Durkan Complex, as
107 well as its significance for the geodynamic evolution of the pre-Eocene Makran
108 Accretionary Prism. Therefore, in this paper, we present new whole-rock, as well as mineral
109 geochemical data on the volcanic and metavolcanics rocks from the Durkan Complex.
110 These data will be discussed in the context of the detailed tectono-stratigraphic results
111 presented by [Barbero et al. \(2021\)](#) with the purpose of adding the final touch to the
112 knowledge of tectono-magmatic setting of formation of this Complex. Finally, these
113 findings will then be discussed for the Late Cretaceous geodynamic evolution of the
114 northern Neo-Tethys realm.

115

116

117 2. Geological setting

118

119 *2.1. General geological setting of the Makran Accretionary Prism*

120

121 The Makran Accretionary Prism is the result of a complex Cretaceous – Present day
122 geodynamic history, which is related to the subduction of the Neo-Tethys oceanic
123 lithosphere below the southern margin of Eurasia ([McCall and Kidd, 1982](#); [Dercourt et al.,](#)
124 [1986](#); [Saccani et al., 2018](#); [Burg, 2018](#); [Monsef et al., 2018](#); [Barrier et al., 2018](#); [Barbero et](#)
125 [al., 2020a, b](#)). The Makran is an E-W trending active subduction complex, which is laterally
126 separated from the Zagros and the Himalayan collisional systems by N-S trending strike-

127 slip fault zones (Figs. 1a, b) (e.g. Dercourt et al., 1986; Kopp et al., 2000; Burg et al., 2013;
128 Mohammadi et al., 2016; Riaz et al., 2019). The present-day deformation front of the
129 Makran is located offshore in the Oman Sea (Fig. 1a). The onshore Makran is characterized
130 by the tectonic juxtaposition of several tectono-stratigraphic domains (Dolati, 2010; Burg et
131 al., 2013). In the western part of the prism these domains are from the structural top to the
132 bottom (i.e., from the north to the south): 1) the North Makran; 2) the Inner Makran; 3) the
133 Outer Makran; 4) the Coastal Makran (Fig. 1c). The Inner, Outer and Coastal Makran
134 domains represent the Eocene - present day accretionary complex and include Eocene –
135 Pleistocene mainly terrigenous sedimentary successions (e.g., Dolati, 2010; Burg et al.,
136 2013; Burg, 2018). The North Makran domain includes remnants of pre-Eocene
137 accretionary stages and consists of a tectonic stack of oceanic and continental derived units,
138 some of which showing variable degrees of metamorphic imprint (e.g., McCall and Kidd,
139 1982; Burg, 2018). These units include from north to south and from the higher to the
140 lowermost structural position (Fig. 1c): 1) the Ganj Complex; 2) the Northern Ophiolites, 3)
141 the Bajgan and Durkan Complexes, 4) the Sorkhband – Rudan tectonic slices 5) the
142 Coloured Mélange Complex.

143 Recent studies have shown that the Ganj Complex represents fragments of a Late
144 Cretaceous volcanic arc that was likely built up close to the southern margin of the Lut
145 Block (Barbero et al., 2020a). The Northern Ophiolites (Fig. 1c) are Early to Late
146 Cretaceous in age and include the Band-e-Zeyarat/Dar Anar (Ghazi et al., 2004; Barbero et
147 al., 2020b), Remeshk-Mokhtarabad (McCall, 1985, 2002; Hunziker et al., 2015; Burg,
148 2018), and Fanuj-Maskutan (Moslempour et al., 2015) ophiolitic complexes. Their
149 magmatic rocks mostly show enriched-type mid-ocean ridge basalts (E-MORB) chemical
150 affinity for the Early Cretaceous ophiolites (Ghazi et al., 2004; Barbero et al. 2020b),
151 whereas the Late Cretaceous ophiolites show supra-subduction zone chemical affinity

152 (Burg, 2018; Monsef et al., 2019, Sepidbar et al., 2020). These ophiolitic complexes were
153 collectively interpreted as the remnants of the oceanic lithosphere of the North Makran
154 Ocean, which is thought to represent an oceanic basin that existed during Late Jurassic –
155 Early Cretaceous at the southern margin of the Central Iran continental plate. The Bajgan
156 and Durkan Complexes (Figs. 1c, 2) have classically been interpreted as remnants of a
157 microcontinental block, which was separated from the Lut Block in the Late Jurassic - Early
158 Cretaceous. The Bajgan Complex is made up of an assemblage of metamorphic rocks that
159 include schists, paragneisses, amphibolites, marbles, as well as basic and acidic meta-
160 intrusive rocks (McCall, 1985; McCall, 2002; Dorani et al., 2017). The P-T condition of the
161 metamorphism and its age are poorly constrained. However, moderately high pressure and
162 high temperature conditions have been suggested (McCall, 1985; Dorani et al., 2017). The
163 Durkan Complex (Figs. 1c, 2) consists of a highly deformed and locally slightly
164 metamorphosed (i.e., up to sub-greenschist facies) complex including: 1) Late Cretaceous
165 shallow-water limestones and thick sequences of alternating limestones, sandstones, shales,
166 cherts and volcanic rocks (Barbero et al., 2021), 2) very minor tectonic slices of
167 Carboniferous, Permian and Jurassic shelf carbonate rocks, as well as marbles and schists
168 (McCall, 1985, 2002; Hunziker et al., 2015); 3) Early – Late Jurassic different types of
169 granitoids intruded into Jurassic shelf limestones in the eastern part of the Makran
170 (Hunziker et al., 2015; Burg, 2018). This Complex has been considered as the original
171 sedimentary cover of the Bajgan metamorphic Complex (McCall, 1985, 2002). However,
172 based on recent multidisciplinary investigation on its western part, Barbero et al. (2021)
173 showed that this Complex represents a tectonically disrupted Late Cretaceous seamounts
174 chain incorporated as tectonic slices into the North Makran accretionary prism.

175 The Deyader Complex crops out in the eastern sector of the North Makran (Fig. 1c). It
176 represents a meta-ophiolitic complex affected by high pressure-low temperature (HP-LT)

177 metamorphism (McCall, 1985; Hunziker et al., 2015; Omrani et al., 2017). The Sorkhband
178 and Rudan ophiolites crop out in the western part of the North Makran within the shear zone
179 between the Coloured Mélange and the Bajgan Complex (McCall, 2002; Delavari et al.,
180 2016). The Coloured Mélange Complex is composed of metric- to decametric-thick tectonic
181 slices and was formed in Cretaceous-Paleocene times (McCall and Kidd, 1982; McCall,
182 2002; Saccani et al., 2018; Burg, 2018; Esmaeili et al., 2019). Saccani et al. (2018) showed
183 that the Coloured Mélange Complex incorporates a great variety of volcanic and meta-
184 volcanic rock-types formed in both the subducting oceanic plate (i.e., oceanic plateau
185 basalts, normal mid-ocean ridge basalts, and alkaline basalts) and the upper plate (i.e. Early
186 - Late Cretaceous island arc tholeiites and calc-alkaline basalts).

187

188 *2.2. Stratigraphic features of the western part of the Durkan Complex*

189

190 Detailed fieldwork and stratigraphic, structural, and biostratigraphic investigations have
191 recently been carried out on the western part of the Durkan Complex (Barbero et al., 2021).
192 This work shows that this Complex (Fig. 2) consists of several tectonic slices, within
193 which different stratigraphic successions can be recognized (Fig. 3). The different slices
194 include both non-metamorphic and slightly metamorphosed successions, all characterized
195 by abundant volcanic rocks (Fig 3a). These stratigraphic successions can be reconciled to
196 three types of successions that are similar to those found at different depths of a seamount
197 setting. The characteristics of these successions, as described by Barbero et al. (2021) are
198 briefly summarized in the following sections.

199

200 *2.2.1. Type I succession: deep-water stage of seamount growth*

201

Formatted: Font color: Black

202 This succession type represents a Coniacian - Campanian pelagic sequence consisting
203 of thin-bedded red cherts and cherty limestones alternated with shales and shaly marls, as
204 well as minor volcanoclastic arenites and pillow breccias. Pillow basalts are frequently
205 interbedded within this sequence (Fig. 3a), and are characterized by low vesicularity (Fig.
206 3b). These features suggest eruption under a relatively thick water column pressure (Fig.
207 3b). This type of succession represents the remnants of a seamount in its deep-water stages
208 of formation characterized by pelagic sedimentation and volcanic activity in a deep-water
209 depositional environment.

210

211 2.2.2. Type II succession: seamount flank during shallow-water stage of a seamount
212 growth

213

214 This succession is characterized by a volcanic sequence showing stratigraphic transition
215 to a volcano-sedimentary sequence that, in turn, gradually passes upward to a pelagic and
216 hemipelagic sedimentary sequence (Fig. 3a). The volcanic sequence is made up ~~by of~~
217 alternating massive lava flows, pillow lavas, and volcanoclastic arenites and breccias (Fig.
218 3a). The volcano-sedimentary sequence consists of alternating volcanoclastic arenites and
219 breccias, shales and siltstones, and Cenomanian limestone, as well as minor massive lava
220 flows (Fig. 3a). Limestones show pelagic foraminifera assemblages suggesting a relatively
221 deep-water depositional setting. Accordingly, the analysis of the volume percent of vesicles
222 for the volcanic rocks suggest a relatively high eruption depth, which is however
223 significantly lower than those of the Type I succession (Fig. 3b). The pelagic and
224 hemipelagic sedimentary sequence consists of cherty limestones, shales, shaly marls, cherts,
225 and minor carbonatic breccias and volcanoclastic arenites (Fig. 3a). The stratigraphic
226 features of Type-II succession ~~point out for~~ indicates a depositional setting along and at the

227 base of a seamount flank during the relatively shallow-water shield stage of growth of a
228 seamount.

229

230 2.2.3. Type III: seamount summit during shallow-water stage of seamount growth

231

232 This stratigraphic succession is characterized by a volcanic sequence passing laterally
233 and upward to a volcano-sedimentary sequence that is, in turn, followed by a Cenomanian
234 carbonatic platform sequence and ends upward with a pelagic and hemipelagic sequence
235 (Fig. 3a). The volcanic sequence is characterized by pillow and massive lava flows
236 alternating with volcanoclastic arenites. The volcano-sedimentary sequence is composed by
237 alternating volcanic rocks, volcanoclastic arenites and breccias, shales, as well as turbidites
238 showing mixed carbonatic - volcanic composition (Fig. 3a). In addition, minor platform-
239 derived massive limestones are interbedded in the sequences, suggesting a shallow-water
240 depositional setting, as also indicated by the particularly high vesicularity of the pillow
241 lavas (Fig. 3b). The Cenomanian, shallow-water carbonatic platform sequence consists of
242 massive limestones alternating with subordinate volcanoclastic arenites but lacks of lava
243 flows (Fig. 3a). The uppermost hemipelagic and pelagic sequence marks the drowning of
244 the carbonatic platform. The stratigraphy of Type-III succession record shallow-water
245 volcanic activity associated with carbonatic platform sedimentation and it is comparable
246 with the stratigraphic successions formed in seamount summit setting during the shallow-
247 water shield stage of growth.

248

249

250 3. Petrography

251

252 The Durkan volcanic and volcano-sedimentary sequences include both volcanic
253 (prevailing) and metavolcanic (subordinate) rocks. The metavolcanic rocks underwent re-
254 crystallization under low-grade metamorphic conditions, though magmatic relicts are
255 commonly preserved in all samples. Volcanic rocks were affected by variable degrees of
256 alteration, which resulted in different extent of replacement of the primary magmatic
257 minerals. Nonetheless, their original magmatic texture is still recognizable. Fresh
258 plagioclase is very rare, and it is usually pseudomorphosed by a fine-grained assemblage of
259 albite, calcite and sericite. Similarly, olivine crystals are commonly replaced by iddingsite
260 and serpentine plus Fe-Ti oxides. Clinopyroxene crystals are present as both phenocrysts
261 and groundmass minerals. They occur either as fresh or altered crystals characterized by
262 pseudomorphic replacement by chlorite or actinolitic amphibole. Volcanic glass has been
263 generally replaced by an assemblage of chlorite and clay minerals. The studied volcanic
264 rocks are represented by basalts, ferrobasalts, and a couple of differentiated rocks (trachyte
265 and alkali-rhyolite). Four types of petrofacies have been distinguished according to
266 textures; they are: 1) aphyric type; 2) porphyritic type; 3) coarse-grained, doleritic type; 4)
267 metamorphic type. Representative microphotographs are given as [Supplementary Figure](#)
268 [S1](#), whereas the texture of each sample is given in [Table 1](#).

269 The aphyric type petrofacies includes basalts and ferrobasalts, as well as one trachyte
270 sample showing aphyric to slightly porphyritic ($PI < 10$) texture. In the slightly porphyritic
271 samples, the phenocrysts consist of plagioclase, clinopyroxene, and locally olivine. They
272 are set in a hypocrySTALLINE groundmass showing intersertal to microcrystalline texture with
273 microlite of plagioclase, olivine, and clinopyroxene and less abundant Fe-Ti oxides,
274 surrounded by altered volcanic glass. In contrast, the trachyte sample is characterized by
275 aphyric texture, showing laths of plagioclase set in altered volcanic glass.

276 The porphyritic type petrofacies includes basalts and ferrobasalts showing porphyritic
277 and glomeroporphyritic texture with PI ranging from 15 to 60. The phenocrysts are up to 5-
278 6 mm in size and are mainly represented by clinopyroxene, minor plagioclase and Fe-Ti
279 oxides, and rare olivine. Clinopyroxene phenocrysts commonly show concentric zonation
280 and weak pleochroism from pale yellow to pale pink. The phenocrysts are set in a
281 hypohyaline groundmass showing intergranular to microcrystalline textures. Rarely,
282 intersertal texture can be observed in the groundmass. The groundmass consists of
283 clinopyroxene and plagioclase together with minor olivine and altered volcanic glass.

284 The coarse-grained doleritic type includes basalts and ferrobasalts showing
285 holocrystalline, inequigranular texture. They are characterized by euhedral plagioclase and
286 euhedral to subhedral clinopyroxene crystals, up to 5 mm in size. Locally, clinopyroxene
287 encloses plagioclase crystals, showing subophitic texture. These large clinopyroxene
288 crystals are surrounded by a fine-grained crystalline aggregate consisting of euhedral to
289 subhedral plagioclase, clinopyroxene as well as Fe-Ti oxides. In ferrobasalts, opaque
290 minerals show subhedral to anhedral morphology.

291 The slightly metamorphic type petrofacies includes metabasalts, and metaferrobasalts,
292 as well as one meta-alkali-rhyolite sample showing anastomosed foliation defined by a
293 fine-grained aggregate of chlorite, fibrous amphibole, Fe-Ti oxides, subordinate epidote, as
294 well as by the alignment of albite aggregates. In most samples, the foliation envelops
295 magmatic relicts consisting of clinopyroxene and minor plagioclase. In a few samples, the
296 metamorphic foliation is well developed and it is marked by the alternation of millimetre-
297 spaced and anastomosed domains with different mineralogical composition. In detail,
298 albite-rich domains alternate with domains showing chlorite, epidote and relicts of
299 magmatic clinopyroxene. The mineralogical paragenesis of these samples, as well as the
300 fine-grained size of the metamorphic minerals indicate very low-grade metamorphic

301 overprint, likely in the sub-greenschist-facies or the prehnite-pumpellyite metamorphic
302 conditions.

303

304

305 4. Analytical methods

306

307 Whole rock major and trace element compositions of a total of forty-three samples is
308 presented in this paper. Thirty-two samples were analysed for rock major and some trace
309 elements by X-ray fluorescence spectrometry (XRF) on pressed-powder pellets, using an
310 ARL Advant-XP automated X-ray spectrometer. The matrix correction method proposed
311 by [Lachance and Trail \(1966\)](#) was applied. Volatile contents were determined as loss on
312 ignition (L.O.I.) at 1000°C. In addition, XRF analyses of eleven samples are taken from
313 [Barbero et al. \(2021\)](#). For the discussion of the geochemical characteristics of the studied
314 rocks major element composition has been re-calculated on L.O.I.-free bases. The rare
315 earth elements (REE) and some trace elements (Rb, Sr, Zr, Y, Nb, Hf, Ta, Th, U) were
316 determined by inductively coupled plasma-mass spectrometry (ICP-MS) using a Thermo
317 Series X-I spectrometer on a total of thirty-nine selected samples. All whole-rock analyses
318 were performed at the Department of Physics and Earth Sciences of the Ferrara University;
319 results are shown in [Table 1](#), where new data from this paper and XRF data from [Barbero
320 et al. \(2021\)](#) are identified. The accuracy of the XRF and ICP-MS data were evaluated
321 using results for international standard rocks run as unknown. The detection limits for XRF
322 and ICP-MS analyses were evaluated using results from several runs of twenty-nine
323 international standards. Results are presented in [Supplementary Table S1](#).

324 The major element composition of clinopyroxene were obtained by electron
325 microprobe spectrometry using a Superprobe Jeol JXA 8200 (JEOL, Tokyo, Japan) at the

326 Eugen F. Stumpfl Laboratory at the University of Leoben, Austria, using both energy
327 dispersive spectrometry (EDS) and wave-length dispersive spectrometry (WDS) systems.
328 The electron microprobe was operated in the WDS mode during the quantitative analyses.
329 An accelerating voltage of 15 kV and beam current of 10 nA were used during the
330 analyses. The diameter of the beam was about 1 μm . Counting times were 20 s on the peak
331 and 10 s on both left and right backgrounds. Standards (element, emission line) were:
332 adularia (Al and Si, $K\alpha$), rutile (Ti, $K\alpha$), chromite (Cr, $K\alpha$), almandine (Fe, $K\alpha$), rhodonite
333 (Mn, $K\alpha$), olivine (Mg, $K\alpha$), wollastonite (Ca, $K\alpha$), albite (Na, $K\alpha$), and sanidine (K, $K\alpha$).
334 The following diffracting crystals were selected: TAP for Na, Mg, and Al; PETJ for K, Si,
335 and Ca; and LIFH for Ti, Cr, Mn and Fe. The detection limits were automatically
336 calculated by the Jeol microprobe software and they are listed in the following as ppm: Na,
337 Al, Mg, K, Ca (100), Si, Cr, Fe, Mn (150) and Ti (200). The results of microprobe analyses
338 are shown in [Table 2](#).

339
340

341 5. Whole rock geochemistry

342

343 The petrographic analysis has shown that the studied rocks have undergone secondary
344 alteration (e.g., ocean-floor hydrothermal alteration) or sub-greenschist facies
345 metamorphism; therefore, some elements may have been remobilized during these
346 processes. In fact, it is well known that large ion lithophile elements and many major
347 elements are commonly affected by alteration-induced mobilization. In addition, light REE
348 (LREE) may also have been mobilized during secondary alteration processes (e.g., [Pearce
349 and Norry, 1979](#)). In contrast, many incompatible elements (e.g., Ti, P, Zr, Y, Sc, Nb, Ta,
350 Hf, Th), middle (M) and heavy (H) REE, as well as some transition metals (e.g., Ni, Co,

351 Cr, V) are considered to be immobile during low-temperature alteration and
352 metamorphism. For these reasons, the geochemical features of the Durkan Complex
353 magmatic rocks are described using those elements considered immobile during alteration
354 processes. Rb and Ba are generally considered as mobile elements. Nonetheless, these
355 elements ~~did not demonstrate a high degree of mobility resulted significantly mobilized~~
356 ~~only in some most samples, whereas in many samples they were little mobilised~~. In fact, in
357 these samples, their contents show good correlations with immobile element contents (e.g.,
358 correlation coefficient with Rb vs. Y = 0.71). Therefore, Rb and Ba will be used, though
359 with caution.

360 The volcanic rocks of the Durkan Complex largely consist of basalts, subordinate
361 ferrobasalts and rare basaltic andesites, trachytes, and alkali rhyolites. Metabasalts and
362 metaferrobasalts though subordinate in volume are also found in all the succession types
363 (Table 1). Metavolcanic rocks will be discussed together with volcanic rocks because this
364 paper is focused on the identification of the geochemical features of the original volcanic
365 protoliths and their tectono-magmatic setting of formation, regardless of the tectono-
366 metamorphic events that affected some tectonic slices of volcanic rocks during their late
367 incorporation in the accretionary wedge. For the sake of simplicity, the prefix “meta” will
368 be hereafter omitted. Basaltic rocks show variable major and trace elements compositions
369 (Table 1), which most likely suggest that they represent melts at different stages of
370 fractionation. Based on the Nb/Y ratios (Winchester and Floyd, 1977; Pearce, 1996), we
371 can distinguish two main groups of rocks (Fig. 4). Group 1 rocks show a transitional nature
372 with Nb/Y ratios in the range 0.8-1.00, whereas Group 2 rocks show a clear alkaline
373 affinity with Nb/Y ratios >1 (1.15-3.16).

374

375 *5.1. Group 1 rocks*

376
377 This group includes basaltic, basaltic andesitic, and ferrobaltic rocks, as well as one
378 trachyte sample. These rocks are mainly found in the Type-I succession, whereas they are
379 less abundant in the Type-II succession and completely lacking in Type-III succession
380 (Table 1). Group 1 basalts show a wide range of composition in terms of SiO₂ (43.3 – 53.3
381 wt%), MgO (4.93 – 11.9 wt%), Al₂O₃ (12.2 – 17.2 wt%), and Mg# (47.8 – 75.4),
382 suggesting that they were likely formed from melts at different degrees of fractionation.
383 The basaltic rocks are characterized by relatively high TiO₂ (1.20 – 2.29 wt%), P₂O₅ (0.23
384 – 0.51 wt%), Zr (73 – 220 ppm), Nb (13.5 – 32.6 ppm), Th (1.49 – 3.66 ppm), and Ta (0.92
385 – 2.18 ppm) contents coupled with relatively low Y contents (16.9 - 33.5 ppm).
386 Compatible elements (Cr, V, Ni, and Co) contents are variable, but generally high, as
387 expected for basaltic rocks (Table 1). The Ti/V ratios are in the range 28 – 61, which are
388 values typically observed in MORB to alkaline transitional basalts (Shervais, 1982).
389 Normal type MORB (N-MORB) normalized incompatible elements spider-diagrams
390 display regularly decreasing patterns from Th to Yb, (Fig. 5a). Yb content in basaltic
391 samples is relatively low, ranging from 0.49 to 0.82 times N-MORB (Sun and
392 McDounough, 1989) abundance (Fig. 5a). Group 1 rocks show mild LREE enrichment
393 with respect to HREE, as well as moderate depletion of HREE if compared to MREE (Fig.
394 5b). This is testified by the (La/Yb)_N, (Sm/Yb)_N, and (Dy/Yb)_N ratios, which are in the
395 range 4.44 – 7.86, 1.18 – 3.16, and 1.25 – 1.56, respectively (Figs. 6a, b). The Yb and La
396 contents are in the range 8.5 - 13.8 and 37.8 - 90.3, times chondrite abundance,
397 respectively (Figs. 5b, 6c). The overall chemical features of the Group 1 rocks are similar
398 to those of many plume-type MORB (P-MORB) in modern oceanic settings (e.g., Le Roex
399 et al., 1983; Sun and McDounough, 1989; Haase and Devey, 1996). Accordingly, in the
400 discrimination diagram in Fig. 7, these rocks plot in the fields for oceanic subduction-

401 unrelated setting, between the compositional fields of P-MORBs and Alkaline basalts.
402 These geochemical data collectively suggest a P-MORB affinity for Group 1 basaltic
403 rocks. Compared to the basaltic samples, the trachyte MK795 shows higher SiO₂ and lower
404 MgO contents (Table 1). As commonly observed in highly fractionated rocks, this sample
405 shows very high Zr (701 ppm) and Y (58 ppm) contents and very low contents of
406 compatible elements, TiO₂ and P₂O₅ (Table 1) as a consequence of early crystallization and
407 removal of mafic minerals, Fe-Ti oxides, and apatite. In fact, this sample shows N-MORB
408 normalized incompatible elements spider-diagrams with significant Ti and P negative
409 anomalies (Fig. 5a). The chondrite-normalized REE pattern of this sample shows a marked
410 Eu negative anomaly and depletion of middle REE (MREE) with respect to HREE (Fig.
411 5a), which suggest crystallization and removal of plagioclase and amphibole, respectively,
412 prior to the formation of the trachytes melts.

413

414 5.2. Group 2 rocks

415

416 The Group 2 rocks include basaltic, and ferrobasaltic rocks, as well as one alkali
417 rhyolitic sample. These rocks show a clear alkaline affinity, as indicated by Nb/Y ratios
418 greater than 1 (Table 1, Fig. 4). Basaltic rocks are characterized by SiO₂ ranging from
419 41.94 to 53.52 wt% and Mg# ranging between 75 and 39 suggesting that these rocks
420 represent melts at different stages of magmatic fractionation. Accordingly, these rocks
421 show marked variation of MgO and Al₂O₃ contents (Table 1). The basaltic rock of the
422 Group 2 show relatively high contents of TiO₂ (1.55 – 5.13 wt%), P₂O₅ (0.20 – 1.10 wt%),
423 Zr (139 – 403 ppm), Nb (23.6 – 71.8 ppm), and Ta (1.42 – 5.13 ppm). Ti/V ratios (41 - 76)
424 are in the range for alkaline basalts (Shervais, 1982). In contrast, Y abundance is rather
425 low, ranging between 18.5 to 33.0 ppm. Compared to Group 1 basalts, the Ti/Y (526 –

426 1448) and Zr/Y (6.7 – 20.6) ratios in Group 2 basalts are higher. The N-MORB normalized
427 incompatible elements spiderdiagrams (Figs. 5c, e) display decreasing patterns from Th to
428 Yb. Yb contents are ~0.6 times N-MORB abundance and are comparable with those of
429 Group 1 rocks. In contrast, both Ta and Nb contents are slightly higher than those of Group
430 1 rocks (Figs. 5a, c, Table 1). The chondrite normalized REE patterns (Figs. 5d, f) show
431 marked decrease from LREE to HREE ($La_N/Yb_N = 9.26 - 28.07$) with Yb and La contents
432 ranging from ~6 - 13 to ~ 100 - 250 times chondrite abundance (Sun and McDonough,
433 1989), respectively. In addition, HREE show marked depletion with respect to MREE, as
434 exemplified by the $(Sm/Yb)_N$ ratios (3.5 – 8.4), which are higher with respect to those of
435 Group 1 (Figs. 6a, b; Table 1).

436 By contrast, alkali rhyolite sample MK339 shows higher contents of SiO_2 and lower
437 MgO abundance with respect to the basaltic rocks (Table 1). This sample shows very high
438 Zr (608 ppm) and Y (69.9 ppm) and very low contents of compatible elements, TiO_2 and
439 P_2O_5 (Table 1). This sample shows N-MORB normalized incompatible elements spider-
440 diagrams with significant Ti and P negative anomalies (Fig. 5c). The chondrite-normalized
441 REE pattern of this sample shows a marked Eu negative anomaly and depletion of HREE
442 with respect both LREE and MREE (Fig. 5d). The overall geochemical features of Group 2
443 rocks are very similar to those of the within-plate alkaline volcanic rocks typically forming
444 oceanic islands (e.g., Yang et al., 2015; Safonova et al., 2016 and reference therein). In the
445 discrimination diagram in Figure 7, the Group 2 rocks plot close to the composition of the
446 ocean island basalt (OIB) (Sun and McDonough, 1989) and within the field for subduction
447 unrelated alkaline basalts.

448 Although Group 2 basaltic rocks show similar major elements and most trace elements
449 contents at comparable degree of fractionation (e.g., comparable Mg#), two different
450 subgroups of samples (hereafter named as Group 2a and Group 2b) can be identified based

451 on different REE patterns and REE ratios, as well as different ratios of some trace
452 elements. These differences are summarized by the REE ratios shown in [Figure 6](#). Group
453 2a basaltic rocks show definitely lower $(La/Yb)_N$ and $(Sm/Dy)_N$ ratios compared to Group
454 2b equivalents ([Figs. 6a, b](#)). In contrast the $(Sm/Yb)_N$ ratios shown by Group 2a and Group
455 2b rocks are largely overlapping, though, as a general tendency, these ratios are
456 comparatively higher in Group 2b rocks ([Figs. 6a, b](#)). The variation of the REE ratios
457 shown in [Figure 6](#) is totally independent from the degree of fractionation of the different
458 samples. It should also be noted that there is no correlation between the LREE/HREE (e.g.,
459 La_N/Yb_N) ratio and the absolute concentration of HREE (e.g., Yb_N) suggesting that the
460 enrichment in LREE with respect to HREE is totally independent on the absolute content
461 of HREE ([Fig. 6c](#)). In addition, Group 2b rocks show higher Nb/Y ([Fig. 4](#)), Nb/Yb, and
462 Th/Tb ratios compared to basaltic rocks of Group 2a

463

464

465 6. Clinopyroxene chemistry

466

467 No ~~fresh unaltered~~ olivine ~~and/or~~ plagioclase ~~crystals were found~~ ~~was identified~~ in the
468 studied rocks, and clinopyroxene underwent secondary alteration in many of the studied
469 samples. Nonetheless, a detailed petrographic study allowed us to recognize fresh
470 clinopyroxene crystals in basaltic samples of the different rock groups, as well as fresh
471 magmatic clinopyroxene relics in one metabasaltic sample. Representative chemical
472 analyses of these crystals are shown in [Table 2](#), whereas their classification according to
473 the quadrilateral diagram is given in [Supplementary Figure S2](#). ~~Beside~~ In addition to
474 crystal-chemical constraints, the clinopyroxene composition is strongly influenced by the
475 composition of the magmas from which they crystallized. According to [Leterrier et al.](#)

476 (1982) and Beccaluva et al. (1989), clinopyroxene composition represents a petrogenetic
477 indicator of the chemical affinity of the magmatic melts from which they crystallized.
478 Therefore, the mineral chemistry of clinopyroxene can provide us robust constraints for
479 understanding the tectono-magmatic setting of formation of basaltic melts. The chemical
480 features of clinopyroxenes will be described according to the whole rock chemical groups.

481

482 *6.1. Group 1 rocks*

483

484 Clinopyroxenes in Group 1 basalts show augitic composition with the wollastonite
485 end-member ranging from ~38% to ~42% (Table 2). Clinopyroxenes of Group 1 rocks
486 show Mg# in the range 0.77 - 0.65, likely reflecting the crystallization from melts at
487 different fractionation stages. CaO, Al₂O₃, and Cr₂O₃ decrease with decreasing Mg#,
488 whereas FeO_{tot} and TiO₂ generally increase with the decreasing Mg# (Table 2). They
489 display relatively low contents of TiO₂ (0.91 – 1.45 wt%), Na₂O (0.28 – 0.46 wt%) and
490 CaO (19.26 – 21.11 wt%) compared to clinopyroxenes from Group 2a and Group 2b rocks
491 (Table 2, Fig. 8). Al₂O₃ (1.44 – 3.06 wt%) is lower than Group 2a and Group 2b
492 clinopyroxene at comparable value of Mg# (Table 2). The Cr₂O₃ content is relatively low
493 and shows positive correlation with Mg#. They are commonly unzoned; only three crystals
494 show little chemical variation from core to rim (Table 2). According to the discrimination
495 diagrams proposed by Leterrier et al. (1982), clinopyroxenes from Group 1 basalts plot in
496 the field for clinopyroxene from sub-alkaline tholeiitic and calc-alkaline rocks and are
497 clearly distinguished from clinopyroxene from Group 2a and Group 2b (Fig. 9a). In
498 addition, the (Ti + Cr) vs. Ca diagram shows that clinopyroxene from Group 1 rocks
499 display MORB affinity (Fig. 9b). Accordingly, in the discrimination diagram of Beccaluva

500 [et al., \(1989\)](#), they plot in the field for clinopyroxene from MOR and within-plate oceanic
501 settings ([Fig. 10](#)).

502

503 *6.2. Group 2a rocks*

504

505 Clinopyroxene from Group 2a were analysed in basalts and ferrobasalts. They mainly
506 show augitic composition, though a few crystals display diopsidic composition. The
507 wollastonite end-member range from ~43% to ~50% ([Table 2](#)). Mg# is generally high,
508 ranging from 0.74 to 0.84. TiO₂ (1.01 – 2.1 wt%), Na₂O (0.33 – 0.5 wt%), CaO (21.02 –
509 22.3 wt%), and Al₂O₃ (2.66 – 4.39 wt%) contents are generally higher than in
510 clinopyroxene from Group 1 rocks ([Table 2](#); [Fig. 8](#)). Cr₂O₃ content is variable (0.12 – 0.67
511 wt%) and gradually decreases with decreasing Mg#. The crystals from sample MK479 are
512 unzoned whereas those from sample MK491 commonly show zoning with Mg# in cores
513 higher than the rims. This variation is coupled with an increase of TiO₂, Al₂O₃, and FeO_{tot}
514 contents, and a decrease of Cr₂O₃, MgO, and CaO from core to rim ([Table 2](#)). These
515 compositional variations likely reflect fractional crystallization processes during the
516 growth of the crystals, as typically observed in clinopyroxene from ophiolitic sequence
517 ([Beccaluva et al., 1989](#)). In the Ti – (Ca + Na) variation diagram, the clinopyroxenes from
518 Group 2a rocks plot in the field for pyroxene from alkaline rocks and are clearly
519 distinguished from the clinopyroxene of the Group 1 rocks ([Fig. 9](#)). Accordingly, in the
520 discrimination diagram of [Beccaluva et al. \(1989\)](#), they plot in the field for clinopyroxenes
521 typical of plume-influenced Iceland basalts and within-plate oceanic basalts ([Fig. 10](#)).

522

523 *6.3. Group 2b rocks*

524

525 Clinopyroxene from Group 2b rocks were analysed in basaltic, ferrobaltic and
526 metabasaltic samples (Table 2). They are mainly represented by diopsidic clinopyroxenes
527 and minor augite. The wollastonite end-member ranges from ~47% to ~49% (Table 2).
528 Mg#, though variable, is generally high (0.74 - 0.87). Clinopyroxenes in Group 2b rocks
529 show generally higher contents of TiO₂ (1.26 – 3.69 wt%), Na₂O (0.28 – 0.66 wt%), CaO
530 (21.7 – 24.3 wt%), and Al₂O₃ (2.88 – 7.08 wt%) compared to those from the other groups
531 of rocks (Fig. 8). Cr₂O₃ contents vary from 0.01 to 1.0 wt% and are positively correlated
532 with Mg# values. Concentric zoning and multiple zones of growth are frequently observed.
533 The zoning is associated to significant chemical variations of TiO₂, CaO, Al₂O₃, Na₂O,
534 MgO, FeO_{tot} and Cr₂O₃ contents from core to rim (Table 2). Generally, the core of the
535 crystals shows higher MgO, Cr₂O₃, and CaO contents coupled with lower TiO₂, Al₂O₃,
536 Na₂O, and FeO_{tot} contents with respect to the rim. However, reverse zoning is observed in
537 some crystals. In addition, some crystals show concentric, oscillatory zoning characterized
538 by different zones of growth, showing rhythmic variation of TiO₂, CaO, Al₂O₃, Na₂O,
539 MgO, FeO_{tot} and Cr₂O₃ contents (Table 2). This is particularly evident for the sample
540 MK859cr1, in which TiO₂, Na₂O, MgO, and Cr₂O₃ show oscillatory chemical variation
541 from the core to the rim of the crystal (Table 2). These features collectively indicate that
542 the growth of the crystals occurred either from a progressively differentiating melt or from
543 the equilibrium with different pulses of new batches of primitive melts at different
544 fractionation stages. The clinopyroxenes of the Group 2b rocks plot in the field for
545 clinopyroxene of alkaline rocks (Fig. 9). An alkaline affinity for the clinopyroxene of
546 Group 2b rocks is also suggested by the discrimination diagram in Figure 10, where they
547 plot within the field for plume-influenced Iceland and within-plate oceanic basalts.

548

549 *6.4. Correlation of clinopyroxene composition vs. whole rock geochemistry*

550

551 Our mineral chemistry data show that there is a close relationship between the
552 composition of clinopyroxenes and the compositions of their hosting rocks. The diagrams
553 in [Figure 8](#) show that the variations of TiO₂, CaO, and Na₂O with respect to the variations
554 of Mg# in clinopyroxenes depict different trends depending on the different rock groups in
555 which these minerals are hosted. Clinopyroxenes from Group 1 transitional basaltic rocks
556 show relatively smooth increase in TiO₂ and Na₂O contents coupled with relatively sharp
557 decrease in CaO contents with decreasing Mg#. In contrast, in clinopyroxenes from the
558 alkaline basaltic rocks of Group 2a and Group 2b TiO₂ and Na₂O contents show sharp
559 increase with decreasing Mg#, whereas CaO contents decrease very smoothly with
560 decreasing Mg# ([Fig. 8](#)). In addition, clinopyroxenes from Group 2a and Group 2b show
561 distinct elemental behaviour with respect to the variation of Mg# values ([Fig. 8](#)). In
562 particular, clinopyroxenes from Group 2b show the relatively sharper increase of TiO₂ and
563 Na₂O contents with decreasing Mg# compared to clinopyroxenes from Group 2a ([Figs. 8a,](#)
564 [c](#)). Clinopyroxenes from Group 2a basaltic rocks are also characterized by higher (Ca +
565 Na) contents compared to those from Group 2b ([Fig. 9](#)). The variation in TiO₂ contents in
566 clinopyroxenes is commonly thought to reflect the degree of depletion or enrichment of the
567 mantle source ([Pearce and Norry, 1979](#)). High TiO₂ content in clinopyroxenes point out for
568 their crystallization from primary magmas generated from enriched mantle sources. The
569 diagrams in [Figure 11](#) clearly show a positive correlation between the Nb/Y ratios of the
570 hosting rocks and the TiO₂, CaO, and Al₂O₃ contents of their clinopyroxenes. The increase
571 in Nb/Y ratios in basaltic rocks is commonly associated with the increase of enrichment of
572 the mantle sources from which they originated ([Winchester and Floyd, 1979](#); [Pearce, 1996,](#)
573 [2008](#)). The contents in TiO₂, CaO, and Al₂O₃ in clinopyroxenes increase from transitional
574 Group 1 basalts to alkaline Group 2a and Group 2b basaltic rocks. Different compositions

575 and elemental co-variations can clearly be distinguished in the clinopyroxenes of the
576 different groups of rocks (Figs. 8, 9, 11). This evidence further supports the conclusions
577 obtained from whole rock chemistry that is, in the Durkan volcanic and metavolcanic rocks
578 three different groups of rocks can be identified (see section 5).

579

580

581 7. Discussion

582

583 7.1. Melt petrogenesis of the volcanic and metavolcanic rocks

584

585 The aim of this petrogenetic discussion is to identify the possible mantle sources for
586 the volcanic rocks and the magmatic protoliths of the metavolcanic rocks from the Durkan
587 Complex, as well as their melting conditions, in order to provide robust constraints for the
588 interpretation of the tectono-magmatic setting of formation of this Complex. Sections 5
589 and 6 have shown that the volcanic and metavolcanic rocks of the Durkan Complex exhibit
590 whole-rock and mineral chemistry with transitional (Group 1) and alkaline (Group 2a and
591 Group 2b) affinities. The different trace elements contents (e.g., Zr, Y, Nb) and REE
592 patterns (Fig. 5) observed in the rocks of these three groups, as well as their different
593 incompatible element (e.g., Zr/Y, Y/Nb, Nb/Yb) and REE ratios (i.e., La_N/Yb_N , Sm_N/Yb_N ,
594 Sm_N/Dy_N) (Table 2, Fig. 6) suggest that these rocks were derived from partial melting of
595 chemically distinct mantle sources and/or different melting conditions. Very similar HREE
596 (e.g., Yb) contents and no correlations between the LREE/HREE (i.e., La_N/Yb_N) ratios
597 observed in all rock groups (Table 2, Fig. 6c) suggest that the differences in the chemistry
598 of their possible mantle sources most likely consisted ~~in~~ of different enrichments in LREE,
599 Zr, and Nb. A first idea about the petrogenesis of the Durkan volcanic and metavolcanic

600 rocks can be deduced from the Zr-Nb co-variation diagram in [Figure 12a](#), which shows
601 that these rocks were generated by partial melting of an enriched and/or transitional mantle
602 source. The mineral chemistry of the clinopyroxenes, in particular their high TiO₂ contents,
603 also point out for the genesis of these rocks from a transitional to enriched mantle sources
604 ([Fig. 10](#)). The diagram in [Figure 12b](#) further supports this conclusion; in fact, the studied
605 rocks plot along the mixing curve between N-MORB and OIB with compositions
606 clustering toward the OIB end member. In addition, the enrichment of OIB-type chemical
607 components increases from Group 1 to Groups 2a and 2b ([Fig. 12b](#)). The Th-Nb co-
608 variation ([Fig.7](#)) further point out for a genesis of the studied rocks from the partial melting
609 of mantle sources that have been influenced by OIB-type chemical components prior to
610 melting without any contributions from subduction related chemical components and/or
611 continental crust contamination.

612 Given these considerations, we performed a semi-quantitative non-modal, batch partial
613 melting modelling in order to constrain the possible mantle peridotite compositions and
614 melting conditions that can reproduce the compositions of the most primitive basalts for
615 each geochemical group of rocks. An accurate definition and quantification of the
616 composition of mantle sources and degrees and depths of partial melting generating the
617 different rock-types is not possible, as these factors cannot be exactly constrained.
618 Therefore, we used different models based on incompatible trace elements ratios and REE
619 in order to better constrain the petrogenesis of the studied rocks ([Figs. 13, 14](#)). These
620 elements are used in the commonly accepted assumption that their content in basaltic rocks
621 basically depend on the composition of the mantle source and its degree of partial melting
622 and it is little influenced by moderate degrees of fractional crystallization of olivine,
623 clinopyroxene and plagioclase (e.g., [Allègre and Minster, 1978](#)).

624 The models in [Fig. 13](#) have the advantage of combining information about the
625 increasing of enrichment of the mantle source (i.e., increasing of Nb/Yb with respect to
626 TiO_2/Yb in [Fig. 13a](#) and increasing of Th with respect to Nb/Yb in [Fig. 13b](#)) and the
627 presence of residual garnet in the source (i.e., TiO_2/Yb in [Fig. 13a](#) and Nb/Yb compared to
628 Th in [Fig. 13b](#)). Results from these binary models have been then compared with the REE
629 model ([Fig. 14](#)). We have previously shown that the composition of the Durkan volcanic
630 and metavolcanic rocks strongly point out for a genesis from partial melting of sub-oceanic
631 mantle sources that have been influenced by OIB-type chemical components. Therefore, in
632 our models we chose as a possible mantle source for the Durkan basaltic rocks a sub-
633 oceanic slightly depleted lherzolite residual after small volume of MORB melt extraction
634 metasomatized to various extents of enrichment by an OIB-type chemical component. In
635 our models, we used the lherzolite ZB2 from the Northern Apennines ([Barbero et al.,](#)
636 [2020c](#)) as representative of a slightly depleted sub-oceanic mantle and the enriched mantle
637 of [Lustrino et al. \(2002\)](#) as the metasomatizing chemical component. The modal
638 compositions of the assumed mantle sources, their chemical composition, the melting
639 proportions and the REE and trace elements distribution coefficients used in the models are
640 listed in [Supplementary Table 2](#).

641 642 7.1.1. Group 1 rocks

643
644 The Nb/Yb vs. TiO_2/Yb model ([Fig. 13a](#)) shows that Group 1 rocks cannot be
645 generated from the partial melting of sources with depleted composition as the DMM
646 ([Workman and Hart, 2005](#)) or the lherzolite ZB2 ([Barbero et al., 2020c](#)). By contrast, the
647 geochemistry of Group 1 primitive basalts is compatible with the partial melting of a
648 calculated S1 mantle source that is significantly more enriched in Nb with respect to the

649 DMM and ZB2 mantle peridotites (Fig. 13a). The high TiO_2/Yb ratios characterizing the
650 Group 1 basalts can be explained by the presence of residual garnet in the mantle source
651 and, therefore, that partial melting started in the garnet-facies mantle (Fig. 13a).
652 Accordingly, the Nb/Yb vs. Th petrogenetic model suggest that the compositions of Group
653 1 primitive basalts can be explained by partial melting of the enriched mantle source S1
654 that starts partial melting in the garnet-facies mantle and continues to larger degrees in the
655 spinel-facies mantle. In detail, the model shows that partial melting degrees are ~2% and
656 ~7% in garnet- and spinel-facies, respectively with mixing of the different melts produced
657 in equal proportions (Fig. 13b).

658 The REE modelling well confirms these results clearly indicating that the REE
659 composition of Group 1 basalts can be explained by partial melting of the mantle source
660 S1, which is significantly enriched in LREE with respect to the DMM and the residual sub-
661 oceanic peridotite ZB2 by OIB-type chemical components (Fig. 14a). According to the
662 results from the models shown in Figure 13, the rather high $(\text{Sm}/\text{Yb})_N$ ratios displayed by
663 Group 1 rocks suggest the involvement of residual garnet in their mantle source. In fact,
664 the composition of Group 1 primitive basalt MK282 fits well with the melt calculated for
665 2.5% and 7.5% of partial melting of the S1 mantle source at garnet- and spinel-facies,
666 respectively, with a mixing proportion between melts generated in the garnet and spinel
667 melts of 50:50 (Fig. 14a). Different melting degrees and mixing proportions of different
668 melts (Fig. 14a₁) fail to reproduce the REE composition of the Group 1 relatively primitive
669 basalt.

670 The fairly differentiated trachyte MK795 clearly display different geochemical
671 patterns compared to basaltic rocks of this Group (Figs. 5a, b). Shallow-level (i.e., magma
672 chamber) petrogenetic processes are beyond the scope of this work since the main goal of
673 this paper is to define the petrogenesis of primary melts in order to constrain their tectono-

674 magmatic setting of formation. In addition, as commonly seen in ophiolites, the
675 tectonically dismembered nature of the volcanic series does not allow basalt-differentiated
676 rocks comagmatic relationships to be reliably constrained. This is particularly true in the
677 Durkan Complex where differentiated samples are very rare. However, differentiated rocks
678 may have various origins and may eventually not be genetically related to the associated
679 mafic rocks. In fact, they may have been generated by fractional crystallization, partial
680 melting of lower crustal rocks (i.e., anatexis), mixing of different melts, etc. We therefore
681 performed Rayleigh fractionation model using REE. Results are shown in [Supplementary](#)
682 [Figure S3](#) together with model parameters and constraints. This model clearly indicates
683 that the REE compositions of the trachyte MK795 is compatible with the composition of a
684 24% residual melt after various steps of crystal fractionation of olivine, plagioclase,
685 clinopyroxene, hornblende, magnetite, and ilmenite starting from the composition of the
686 near-primary basalt MK282 used in the mantle partial melting model shown above (see
687 also [Figs. 13, 14](#)). It follows that trachyte MK795 represent a differentiated product formed
688 by fractional crystallization.

689

690 7.1.2. Group 2a and Group 2b rocks

691

692 Group 2a and Group 2b alkaline rocks collectively show overall whole rock chemistry
693 ([Table 1](#); [Fig. 6](#)) and mineral chemistry ([Fig. 9](#)) that are quite different from those of the
694 transitional Group 1 rocks. In particular, basaltic rocks from these groups show much
695 higher Nb, Ta, Th, LREE/HREE and MREE/HREE ratios with comparable Yb absolute
696 contents ([Fig. 6](#); [Table 1](#)), which cannot be explained with partial melting of the S1 source.
697 These chemical features point out for a genesis from a mantle source more enriched
698 (source S2) in these elements and LREE compared to the theoretical S1 source. Similar to

699 Group 1 rocks, the high $(La/Yb)_N$, TiO_2/Yb , and Nb/Yb ratios of Group 2a and Group 2b
700 rocks suggest residual garnet in the mantle source (Figs. 6a, 13). Nonetheless, Group 2a
701 and Group 2b rocks, though very similar in composition for many elements, slightly differ
702 in their $(La/Yb)_N$ and $(Sm/Dy)_N$ ratios (Fig. 6). These differences can be explained either
703 with slightly different compositions of their mantle sources or different proportions of
704 partial melting in the garnet- and spinel-facies mantle. However, the chemical differences
705 between basalts of these two groups are limited to a few elemental ratios basically
706 involving HREE (e.g., TiO_2/Yb , Nb/Yb , Th/Tb , Sm/Dy). As a consequence, it is
707 reasonable to assume that the chemical differences between basalts of these two Groups
708 are most likely due to different proportions of partial melting in the garnet- and spinel-
709 facies mantle, rather than chemical differences of the mantle sources. Therefore, in the
710 models in Figures 13 and 14 we use the same theoretical mantle source S2 for both Group
711 2a and 2b basalts. In fact, the TiO_2/Yb vs. Nb/Yb model suggests that the genesis of
712 relatively primitive basalts from both rock groups is related to the partial melting of the
713 mantle source S2 that starts in the garnet-facies mantle. However, the composition of the
714 relatively primitive basalt of Group 2a is compatible with partial melting starting at a
715 higher pressure (4GPa) compared to Group 2b primitive basalt (3GPa) (Fig. 13a). The
716 Nb/Yb vs. Th model show that the composition of Group 2a relatively primitive basalt
717 MK340 is compatible with ~2% partial melting of the source S2 in the garnet-facies mantle
718 followed by 5% partial melting in the spinel-facies mantle, with mixing of the different
719 melts in the proportions 60% garnet melt - 40% spinel melt. (Fig. 13b). In contrast, the
720 composition of Group 2b relatively primitive basalt MK499 is compatible with 1% partial
721 melting of the source S2 in the garnet-facies mantle followed by ~3% partial melting in the
722 spinel-facies mantle, with mixing of the different melts in the proportions 65% garnet melt
723 - 35% spinel melt. (Fig. 13b).

724 Accordingly, REE model indicates that the REE composition of the relatively
725 primitive basalt MK340 (Group 2a) can be explained by ~2 % partial melting in the garnet-
726 facies and ~5% partial melting in the spinel-facies of the mantle source S2 with mixing of
727 the different melts in the proportions 60% garnet melt - 40% spinel melt (Fig. 14b).
728 Likewise, the REE model carried out for Group 2b rocks (Fig. 14c) is perfectly in
729 agreement with the models based on TiO₂, Nb, Th, and Yb contents (Fig. 13). The model
730 in Figure 14c shows indeed that the REE composition of the relatively primitive basalt
731 MK499 is compatible with 1.5% partial melting in the garnet-facies mantle followed by
732 4% partial melting in the spinel-facies mantle of the source S2, with mixing of the different
733 melts in the proportions 65% garnet melt - 35% spinel melt.

734 As already discussed in section 7.1.1 for the trachyte MK795, the different chemistry
735 of the alkali rhyolite MK339 compared to Group 2 basalts (Figs. 5c-f) may reflect the
736 effect of fractional crystallization, or anatexis, or other petrogenetic processes. Rayleigh
737 fractionation model using REE are shown in Supplementary Figure S3. This model clearly
738 shows that the REE compositions of the alkali rhyolite MK339 is compatible with the
739 composition of a 25% residual melt after various steps of crystal fractionation of olivine,
740 plagioclase, clinopyroxene, magnetite, and ilmenite starting from the composition of the
741 near-primary basalt MK340 used in the mantle partial melting model for Group 2a rocks
742 (see also Figs. 13, 14b).

743

744 7.2. Tectono-magmatic significance of the volcanic and metavolcanic rocks

745

746 Previous studies have suggested that the Durkan Complex represents remnants of the
747 Permian - Cretaceous continental margin of the Bajgan Complex microcontinental
748 basement (McCall, 1985; Hunziker et al., 2015). However, a recent multidisciplinary study

749 of the western part of the Durkan Complex has demonstrated that it consists of Late
750 Cretaceous volcano-sedimentary successions, which represent portions of a seamount or,
751 most likely, of a seamount chain (Barbero et al., 2021). The geochemical and mineral
752 chemistry data, as well as petrogenetic models presented in this paper collectively suggest
753 that the volcanic rocks in these sequences consist of an association of transitional P-
754 MORBs and alkaline OIBs, which were formed by partial melting of enriched mantle
755 sources with variable contribution of melts formed at both garnet- and spinel-facies. These
756 data strongly support the interpretation of the Barbero et al. (2021). In Figure 15 we
757 therefore propose a schematic tectono-magmatic model that can explain the petrogenetic
758 processes, which occurred during the formation of the Durkan seamount chain. According
759 to Barbero et al. (2021), the Type-II and Type-III volcano-sedimentary successions consist
760 of remnants of seamount flank and seamount summit depositional and eruptive settings,
761 respectively, and were formed during the Cenomanian in the shallow-water stage of
762 growth of a seamount (Fig. 15a). These types of successions are characterized by alkaline
763 volcanic rocks (Group 2a and Group 2b), whose geochemistry and melt petrogenesis (see
764 section 7.1) clearly indicate that they derived from low degree of partial melting at both
765 garnet- and facies-spinel of an enriched OIB-type (plume-type) mantle source (S2 in Fig.
766 15a). By contrast, the Type-I volcano-sedimentary succession represents the remnants of
767 Coniacian – early Campanian sedimentation and volcanism in a pelagic setting during the
768 deep-water stage of growth of a seamount (Fig. 15b; Barbero et al., 2021). This Type of
769 succession is mainly characterized by transitional P-MORB rocks (Group 1) and minor
770 Group 2a alkaline rocks, whereas Group 2b basalts were not found in this succession. The
771 petrogenetic model show that, compared to Group 2a basalts, Group 2b basalts are
772 characterized by higher proportions of melts formed at garnet-facies with respect to melts
773 formed at spinel-facies mantle and an overall smaller degree of partial melting (Fig. 14).

774 By contrast, the deep-water stage of formation of the seamounts was characterized by the
775 partial melting of an enriched mantle source bearing strongly enriched mantle patches
776 (sources S1 and S2, respectively in [Fig. 15b](#)). The lack of Group 2b rocks and the
777 prevalence of Group 1 rocks may also be explained by mantle partial melting at relatively
778 shallower depth and higher partial melting degree during the deep-water stage of the
779 seamount formation with respect to the shallow-water stage of the seamount growth ([Figs.](#)
780 [15a, b](#)). In addition, this implies a minor contribution of melts produced at garnet-facies
781 with respect to the shallow-water stage of the seamount growth. These features are
782 compatible with oceanic within-plate magmatism related to the rising of deep, enriched
783 mantle plume material ([Figs. 15a, b](#)). Indeed, mantle plumes are likely the most effective
784 mean for transferring anomalous heat flux and enriched chemical components from the
785 lower to the upper mantle (e.g., [Regelous et al., 2003](#); [Pearce, 2008](#); [White, 2010](#); [Kerr,](#)
786 [2014](#); [Safonova and Santosh, 2014](#)). The rising of mantle material that is more enriched
787 and hotter than the ambient sub-oceanic mantle facilitates the starting of the partial melting
788 at deeper level within the garnet stability field ([Figs. 15a, b](#)). This can well explain the
789 clear residual garnet geochemical signature shown by all the studied rocks. The processes
790 responsible for the geochemical variation of the erupted basalts during the different stage
791 of growth of the Durkan seamount chain are difficult to be constrained in detail, mainly
792 because of the disrupted tectonic nature of the different Durkan successions, which is, in
793 turn, related to multiple deformative events occurred during their incorporation into the
794 accretionary prism ([Barbero et al., 2021](#)). However, it is commonly accepted that during
795 the progressive growth of seamounts, from the early stage of formation to their emergence
796 above the sea level (i.e., shallow-water shield stage), the volcanic products progressively
797 change from tholeiitic rocks to progressively more enriched transitional and alkaline rocks
798 (e.g., [Moore and Clague, 1992](#); [Regelous et al., 2003](#)). In this classical scenario the Durkan

799 Type I, II and III successions are associated with progressive chemical changes of magmas
800 from tholeiitic to alkaline signatures, which could be mainly derived from different degrees
801 of partial melting of variably enriched mantle sources. The chemical composition of
802 analysed clinopyroxenes is also consistent with progressive chemical changes of magmas
803 from tholeiitic to alkaline nature. The chemical variation of seamount volcanic rocks may
804 be explained by the combination of several factors, such as: 1) the increasing contribution
805 from an enriched mantle source to the ambient sub-oceanic mantle; 2) the decreasing in
806 partial melting degrees; 3) the increase of the depth of partial melting; 4) the variation of
807 the thickness of the melting column (e.g., [Regelous et al., 2003](#); [Safonova, 2008](#); [White,](#)
808 [2010](#); [Safonova and Santosh, 2014](#)). According to [Safonova et al. \(2016\)](#), the large
809 volumetric prevalence of alkaline rocks in the shallow-water shield stage of the Durkan
810 volcano-sedimentary sequences suggest relatively higher contributions of melting in the
811 garnet-facies of a strongly enriched mantle source during this stage coupled with the
812 decrease of the overall partial melting degree ([Fig. 15a](#)). These features are consistent with
813 the deepening of the partial melting region in response of the enhancing of the lithospheric
814 load (i.e., crust + lithospheric mantle) due to the thickening of the seamount edifice
815 coupled with an increasing of the mantle plume influence on the sub-oceanic ambient
816 mantle and a shortening of the melting mantle column ([Fig. 15a](#)). By contrast, during the
817 deep-water stage of the seamount life the crustal load is significantly lower. In this stage,
818 the sub-oceanic mantle is relatively less influenced by the metasomatizing effects of the
819 mantle plume ([Fig. 15b](#)). The combination of these effects likely produces partial melting
820 of a moderately enriched mantle source, though partial melting may also involve strongly
821 enriched portions of the mantle. In this stage, partial melting in the spinel-facies is
822 prevailing with respect that in the garnet-facies mantle as the melting mantle column is
823 rather wide ([Fig. 15b](#)). This hypothesis agrees with data from both modern and ancient

824 seamounts, which point out the importance of the lithospheric thickness in controlling the
825 melting processes associated with the rising of a mantle plume. In detail, a thin lithosphere
826 above a mantle plume causes the shallowing of partial melting combined with higher
827 degree of the partial melting, producing melts less enriched in LREE with respect to M-
828 and HREE. By contrast, higher thickness of lithosphere likely causes the deepening of the
829 partial melting region combined with the decrease of the partial melting degree and the
830 shortening of the melting column, thus, promoting the prevalence of partial melting at the
831 garnet-facies (e.g., [Regelous et al., 2003](#); [Safonova, 2008](#); [White, 2010](#)).

832

833

834 *7.3. Geodynamic significance of the western Durkan Complex: A Late Cretaceous*
835 *seamount chain in the northern Neo-Tethys?*

836

837 Cretaceous alkaline and OIB rocks comparable with those of the Durkan Complex are
838 widespread within the Neo-Tethys-related collisional belts from Caucasus to Himalaya.
839 They have commonly been interpreted as remnants of seamounts and/or oceanic plateau
840 associated with mantle-plume activity (e.g., [Rolland et al., 2010, 2020](#); [Saccani et al.,](#)
841 [2013, 2018](#); [Yang and Dilek, 2015](#); [Yang et al., 2015, 2019](#); [Esmaili et al 2019](#); [Barbero](#)
842 [et al., 2020b, 2021](#)). This evidence supports the hypothesis that the tectono-magmatic
843 evolution of different sectors of the Neo-Tethys Ocean was strongly influenced by the
844 wide occurrence of mantle plume activity at a regional-scale during the Late Cretaceous.
845 Our data well agree with this general scenario of the Cretaceous Neo-Tethys, as they point
846 out for the existence of a significant mantle plume activity in the Makran sector of this
847 Ocean during the same time. Our data allow us to depict two different stages of a seamount
848 growth at two different times. The Type-II and Type-III volcano-sedimentary successions

849 of the Durkan Complex include Cenomanian carbonatic platform and strongly enriched
850 alkaline basalts, thus recording the existence of one or more oceanic seamounts that
851 reached a shallow-water shield stage during the early Late Cretaceous (Fig. 15a). The
852 occurrence of “mature” seamount edifices implies that a vigorous mantle plume activity
853 was already existing in the oceanic basin at that time. By contrast, the Durkan Type-I
854 succession, which is characterized by pelagic sediments and prevailing transitional
855 volcanic rocks, records an early phase of growth of a seamount (i.e., deep-water stage) in
856 the late Late Cretaceous (Fig. 15b). A general fading away at the end of Cretaceous of
857 OIB-type volcanism is observed in the Neo-Tethyan related belts from Caucasus to
858 Himalaya and it is interpreted to reflect a progressively decreasing mantle plume activity in
859 the Neo-Tethys during these times (e.g., Rolland et al., 2010, 2020; Yang and Dilek, 2015;
860 Esmaeili et al 2019; Barbero et al., 2020b, 2021). We can speculate that the occurrence in
861 the Durkan Complex of a relatively older (Cenomanian) mature seamount and a relatively
862 younger (Coniacian – Campanian) immature seamount may eventually be related to the
863 Late Cretaceous progressive decreasing of plume activity observed at a regional scale. This
864 hypothesis needs, however, to be proved by further studies.

865

866

867

868 8. Conclusion

869

870 The Durkan Complex represents a tectonic element of the North Makran domain that
871 was classically interpreted as a continental margin succession though a recent study
872 suggested that it represents a tectonically disrupted portion of a Late Cretaceous seamount

873 chain. The petrographic and geochemical study presented in this paper allow the following
874 conclusion to be drawn:

- 875 1) The Durkan Complex is composed by tectonic slices showing successions similar
876 to those found at different depths of a seamount environment. The successions are
877 characterized by abundant volcanic rocks and are either non-metamorphic or
878 slightly metamorphosed.
- 879 2) The volcanic and metavolcanics rocks are largely represented by basaltic rocks.
880 Based on whole rock chemistry and clinopyroxene chemistry, basaltic rocks
881 consist of both transitional basalts showing P-MORB composition (Group 1) and
882 alkaline basalts showing OIB composition (Groups 2a and 2b).
- 883 3) The chemical composition of clinopyroxenes from the different rock groups is
884 strictly depending on the whole rock composition of their hosting rocks. In
885 particular, TiO_2 , Al_2O_3 , and Na_2O contents in minerals increase from transitional to
886 alkaline basalts.
- 887 4) Petrogenetic models indicate that the Durkan volcanic rocks derived from partial
888 melting of a sub-oceanic mantle metasomatized to various extents by an OIB-type
889 chemical component. The chemical difference between different Groups of basalts
890 are related to a combination of different extents of metasomatic enrichment and
891 different melting conditions (i.e., partial melting degrees and melting depths).

892 Our new data compared to literature data allow us to conclude that the different
893 volcano-sedimentary successions of the Durkan Complex record portions of seamounts of
894 different ages formed during both shallow-water shield stage (Cenomanian) and deep-
895 water stage (Coniacian-Campanian). The age, composition, and evolution of these distinct
896 seamounts in the Makran sector of the Neo-Tethys is compatible with regional-scale
897 evidence (from Caucasus to Himalaya), which suggest that abundant transitional and

898 alkaline basalts were erupted as a consequence of the interaction between the sub-oceanic
899 lithosphere and significant mantle plume activity.

900

901

902

903

904

905 **Acknowledgment**

906

907 The research has been funded by: Darius Project (Head M. Marroni), PRA project of the Pisa
908 University (Head S. Rocchi), IGG-CNR, FAR-2018 Project of the Ferrara University (Head E.S.).
909 R. Tassinari and R. Tamoni (University of Ferrara) are acknowledged for technical support with
910 chemical analyses and with thin section production, respectively. Mr. Ahmad Behboodi is sincerely
911 thanked for his appreciated assistance in organizing field work, and PhD student Ahmad
912 Nateghpour from Kharazmi University is thanked for his help during field work. Constructive and
913 thorough reviews for the Journal by two anonymous reviewers, as well as valuable suggestions by
914 the Editor G. Shellnutt have helped us improve the science and organization presented in the paper.

915

916

917

918

919

920

921

922

923 **References**

924 Allahyari, K., Saccani, E., Rahimzadeh, B., Zeda, O., 2014. Mineral chemistry and petrology
925 of highly magnesian ultramafic cumulates from the Sarve-Abad (Sawlava) ophiolites
926 (Kurdistan, NW Iran): New evidence for boninitic magmatism in intra-oceanic fore-arc
927 setting in the Neo-Tethys between Arabia and Iran. *Journal of Asian Earth Sciences* 79,
928 312–328, doi: 10.1016/j.jseae.2013.10.005.

929 Allègre, C.J., Minster, J.F., 1978. Quantitative models of trace element behavior in magmatic
930 processes. *Earth Planet. Sci. Lett.* 38, 1-25.

931 Bagheri, S., Stampfli, G., 2008. The Anarak, Jandaq and Posht-e-Badam metamorphic
932 complexes in central Iran: New geological data, relationships and tectonic implications.
933 *Tectonophysics* 451, p. 123–155. <https://doi.org/10.1016/j.tecto.2007.11.047>.

934 Barbero, E., Delavari, M., Dolati, A., Saccani, E., Marroni, M., Catanzariti, R., Pandolfi, L.,
935 2020a. The Ganj Complex reinterpreted as a Late Cretaceous volcanic arc: Implications
936 for the geodynamic evolution of the North Makran domain (southeast Iran). *Journal of*
937 *Asian Earth Science*, <https://doi.org/10.1016/j.jseae.2020.104306>.

938 Barbero, E., Delavari, M., Dolati, A., Vahedi, L., Langone, A., Marroni, M., Pandolfi, L.,
939 Zaccarini, F., Saccani, E., 2020b. Early Cretaceous Plume–Ridge Interaction Recorded
940 in the Band-e-Zeyarat Ophiolite (North Makran, Iran): New Constraints from
941 Petrological, Mineral Chemistry, and Geochronological Data. *Minerals* 10, 1100,
942 doi:10.3390/min10121100.

943 Barbero, E., Festa, A., Saccani, E., Catanzariti, R., D’Onofrio, R., 2020c. Redefinition of the
944 Ligurian Units at the Alps–Apennines junction (NW Italy) and their role in the evolution
945 of the Ligurian accretionary wedge: constraints from mélanges and broken formations.
946 *Journal of the Geological Society of London* 177, 562–574,
947 <https://doi.org/10.1144/jgs2019-022>.

948 Barbero, E., Pandolfi, L., Delavari, M., Dolati, A., Saccani, E., Catanzariti, R., Lucani, V.,
949 Chiari, M., Marroni, M., 2021. The western Durkan Complex (Makran Accretionary
950 Prism, SE Iran): A Late Cretaceous tectonically disrupted seamounts chain and its role
951 in controlling deformation style. *Geoscience Frontiers* 12,
952 <https://doi.org/10.1016/j.gsf.2020.12.001>.

953 Barrier, E., Vrielynck, B., Brouillet, J.F., Brunet, M.F., 2018. Paleotectonic Reconstruction of
954 the Central Tethyan Realm. Tectonono-Sedimentary-Palinspastic maps from Late
955 Permian to Pliocene. Atlas of 20 maps (scale: 1:15.000.000). CCGM/CGMW, Paris,
956 <http://www.ccgm.org>.

957 Beccaluva, L., Macciotta, G., Piccardo, G.B., Zeda, O., 1989. Clinopyroxene compositions of
958 ophiolite basalts as petrogenetic indicator. *Chemical Geology* 77, 165-182.

959 Bonnet, G., Agard, P., Angiboust, S., Monié, P., Fournier, M., Caron, B., Omrani, J., 2020.
960 Structure and metamorphism of a subducted seamount (Zagros suture, Southern Iran).
961 *Geosphere*, 16, 62–81. <https://doi.org/10.1130/GES02134.1>

962 Bortolotti, V., Chiari, M., Goncuoglu, M.C., Principi, G., Saccani, E., Tekin, U.K., Tassinari,
963 R., 2017. The Jurassic–Early Cretaceous basalt–chert association in the ophiolites of the
964 Ankara Mélange, east of Ankara, Turkey: age and geochemistry. *Geological Magazine*
965 155, 451-478, doi: <https://doi.org/10.1017/S0016756817000401>.

966 Burg, J.-P., 2018. Geology of the onshore Makran accretionary wedge: Synthesis and tectonic
967 interpretation. *Earth Science Reviews* 185, 1210-1231,
968 <https://doi.org/10.1016/j.earscirev.2018.09.011>.

969 Burg, J.-P., Bernoulli, D., Smit, J., Dolati, A., Bahroudi, A., 2008. A giant catastrophic mud-
970 and-debris flow in the Miocene Makran. *Terra Nova* 20, 188-193.

971 Burg, J.-P., Dolati, A., Bernoulli, D., Smit, J., 2013. Structural style of the Makran tertiary
972 accretionary complex in SE Iran. In: Al Hosani, K., Roure, F., Ellison, R., Lokier, S.

973 (Eds.), *Lithosphere Dynamics and Sedimentary Basins: The Arabian Plate and*
974 *Analogues*. *Frontiers in Earth Sciences* vol.5. Springer, Berlin, Heidelberg, pp. 239-259.

975 Chauvet, F., Lapierre, H., Maury, R.C., Bosch, D., Basile, C., Cotten, J., Brunet, P., Campillo,
976 S., 2011. Triassic alkaline magmatism of the Hawasina Nappes: Post-breakup melting of
977 the Oman lithospheric mantle modified by the Permian Neotethyan Plume. *Lithos* 122,
978 122-136.

979 Delavari, M., Dolati, A., Marroni, M., Pandolfi, L., Saccani E., 2016. Association of MORB
980 and SSZ ophiolites along the shear zone between Coloured Mélange and Bajgan
981 Complexes (North Maran, Iran): Evidence from the Sorkhband area. *Ophioliti* 41, 21-34.

982 Dercourt, J., Zonenshian, L.P., Ricou, L.E., Kazmin, V.G., LePichon, X., Knipper, A.L.,
983 Grandjacquet, C., Sbertshikov, M., Geysant, J., Lepvrier, C., Pechersky, D.H., Boulin,
984 J., Sibuet, J.C., Savostin, L.A., Sorokhtin, O., Westphal, M., Bazhenov, M.L., Lauer,
985 J.P., Biju-Duval, B., 1986. Geological evolution of the Tethys Belt from the Atlantic to
986 the Pamir since the Lias. *Tectonophysics* 123, 241-315.

987 Dilek, Y., Furnes, H., 2011. Ophiolite genesis and global tectonics: geochemical and tectonic
988 fingerprinting of ancient oceanic lithosphere. *Geological Society of America Bulletin*
989 123, 387-411.

990 Dolati, A., Burg, J.-P., 2013. Preliminary fault analysis and paleostress evolution in the
991 Makran Fold-and-Thrust Belt in Iran. In: Al Hosani, K., Roure, F., Ellison, R., Lokier,
992 S. (Eds.), *Lithosphere Dynamics and Sedimentary Basins: The Arabian Plate and*
993 *Analogues*. *Frontiers in Earth Sciences*, Springer, Heidelberg, pp. 261–277.
994 https://doi.org/10.1007/978-3-642-30609-9_13

995 Dolati, A., 2010. *Stratigraphy, Structure Geology and Low-temperature Thermochronology*
996 *Across the Makran Accretionary Wedge in Iran*. (PhD Thesis). ETH Zurich, pp. 165.

997 Dorani, M., Arvin, M., Oberhänsli, R., Dargahi, S., 2017. P-T evolution of metapelites from
998 the Bajgan complex in the Makran accretionary prism, south eastern Iran. *Geochemistry*
999 77, 459–475. <https://doi.org/10.1016/j.chemer.2017.07.004>.

1000 Droop, G.T.R., 1987. A general equation for estimating Fe³⁺ concentrations in
1001 ferromagnesian silicates and oxides from microprobe analyses, using stoichiometric
1002 criteria. *Mineralogical Magazine* 51, 431–435.

1003 Eftekhar-Nezhad, J., Arshadi, S., Mahdavi, M.A., Morgan, K.H., McCall, G.J.H., Huber, H.,
1004 1979. Fannuj Quadrangle Map 1:250000. Tehran: Ministry of Mines and Metal,
1005 Geological Survey of Iran.

1006 Esmacili, R., Xiao, W., Ebrahimi, M., Zhang, J.E., Zhang, Z., El-Rahman, Y.A., Han, C.,
1007 Wan, B., Ao, S., Song, D., Shahabi, S., Aouizerat, A., 2019. Makran ophiolitic basalts
1008 (SE Iran) record Late Cretaceous Neotethys plume-ridge interaction. *International*
1009 *Geology Review*, doi: 10.1080/00206814.2019.1658232.

1010 Ghazi, A.M., Hassanipak, A.A., Mahoney, J.J., Duncon R.A., 2004. Geochemical
1011 characteristics, 40Ar-39Ar ages and original tectonic setting of the Band-e-Zeyarat/Dar
1012 Anar ophiolite, Makran accretionary Prism, S.E. Iran. *Tectonophysics* 193, 175-196.

1013 Gradstein, F.M., Ogg, J.G., Scmitz, M.D., Ogg G.M., 2012. *The Geologic Time Scheme*.
1014 Elsevier, Amsterdam, International Commission on Stratigraphy, pp.1144.

1015 Haase, K.M., Devey, C.W., 1996. Geochemistry of lavas from the Ahu and Tupa volcanic
1016 fields, Easter Hotspot, southeast Pacific: Implications for magma genesis near a
1017 spreading axis. *Earth and Planetary Science Letters* 137, 129-143.

1018 Hanan, B. B., Blichert-Toft, J., Kingsley, R., Schilling, J.-G., 2000. Depleted Iceland mantle
1019 plume geochemical signature: Artifact of multicomponent mixing? *Geochemistry,*
1020 *Geophysics, Geosystems*, 1(4), <https://doi.org/10.1029/1999GC000009>

- 1021 Hässig, M., Rolland, Y., Sosson, M., Galoyan, G., Sahakyan, L., Topuz, G., Çelik, Ö.F.,
1022 Avagyan, A., Müller, C., 2013. Linking the NE Anatolian and Lesser Caucasus
1023 ophiolites: evidence for large-scale obduction of oceanic crust and implications for the
1024 formation of the Lesser Caucasus-Pontides Arc. *Geodinamica Acta* 26, 311–330,
1025 <https://doi.org/10.1080/09853111.2013.877236>
- 1026 Hunziker, D., Burg, J.-P., Bouilhol, P., von Quadt, A., 2015. Jurassic rifting at the Eurasian
1027 Tethys margin: Geochemical and geochronological constraints from granitoids of North
1028 Makran, southeastern Iran. *Tectonics* 34, 571-593.
- 1029 Isozaki, Y., Maruyama, S., Furuoka, F., 1990. Accreted oceanic materials in Japan.
1030 *Tectonophysics*, 181, 179–205. [https://doi.org/10.1016/0040-1951\(90\)90016-2](https://doi.org/10.1016/0040-1951(90)90016-2)
- 1031 Janney, P.E., Le Roex, A.P., Carlson, R.L., 2005. Hafnium isotope and trace element
1032 constraints on the nature of mantle heterogeneity beneath the Central Southwest Indian
1033 Ridge. *Journal of Petrology* 46, 2427-2464.
- 1034 Kerr, A.C., 2014. Oceanic Plateaus. In: Holland, H.D., Turekian, K.K. (Eds.), *Treatise on*
1035 *Geochemistry*, Second edition vol. 4, Elsevier, Oxford, pp. 631–667.
- 1036 Khan, S.R., Jan, M.Q., Khan, T., Khan, A.M., 2007. Petrology of the dykes from the
1037 Waziristan Ophiolite, NW Pakistan, *Journal of Asian Earth Sciences* 29, 369-377, doi:
1038 [10.1016/j.jseaes.2006.08.001](https://doi.org/10.1016/j.jseaes.2006.08.001)
- 1039 Kopp, C., Fruehn, J., Flueh, E.R., Reichert, C., Kukowski, N., Bialas, J., Klaeschen, D., 2000.
1040 Structure of the Makran subduction zone from wide-angle and reflection seismic data.
1041 *Tectonophysics* 329, 171–191, [https://doi.org/10.1016/S0040-1951\(00\)00195-5](https://doi.org/10.1016/S0040-1951(00)00195-5)
- 1042 Lachance, G.R., Trail, R.J., 1966. Practical solution to the matrix problem in X-ray analysis.
1043 *Canadian Spectroscopy* 11, 43-48.
- 1044 LeRoex, A.P., Dick, H.J.B., Erlank, A.J., Reid, A.M., Frey, F.A., Hart, S.R., 1983.
1045 *Geochemistry, Mineralogy and Petrogenesis of Lavas Erupted along the Southwest*

1046 Indian Ridge Between the Bouvet Triple Junction and 11 degrees East. *Journal of*
1047 *Petrology* 24, 267-318.

1048 Leterrier, J., Maury, R.C., Thonon, P., Girard, D., Marchal, M., 1982. Clinopyroxene
1049 composition as a method of identification of the magmatic affinities of paleo-volcanic
1050 series. *Earth and Planetary Science Letters* 59, 139-154.

1051 Lustrino, M., Melluso, L., Morra, V., 2002. The transition from alkaline to tholeiitic magmas:
1052 a case study from the Orosei-Dorgali Pliocene volcanic district (NE Sardinia, Italy).
1053 *Lithos* 63, 83–113.

1054 McCall, G.J.H., 1985. Explanatory text of the Minab Quadrangle Map; 1:250,000; No. J13.
1055 Geological Survey of Iran, Tehran, pp. 530.

1056 McCall, G.J.H., 2002. A summary of the geology of the Iranian Makran. *The Tectonic and*
1057 *Climatic Evolution of the Arabian Sea Region*. In: Clift, P.D., Kroon, D., Gaedicke, C.,
1058 Craig, J. (Eds.), *Geological Society of London Special Publications* 195, 147-204.

1059 McCall, G.J.H., Kidd, R.G.W., 1982. The Makran southeastern Iran: the anatomy of a
1060 convergent margin active from Cretaceous to present. In: Leggett, J.K. (Ed.), *Trench-*
1061 *forearc geology: sedimentation and tectonics of modern and ancient plate margins*. Vol
1062 10, 387-397.

1063 Mohammadi, A., Burg, J.-P., Winkler, W., Ruh, J., von Quadt, A., 2016. Detrital zircon and
1064 provenance analysis of Late Cretaceous–Miocene onshore Iranian Makran strata:
1065 Implications for the tectonic setting. *Geological Society of America Bulletin* 128, 1481–
1066 1499. <https://doi.org/10.1130/B31361.1>

1067 Monsef, I., Rahgoshay, M., Pirouz, M., Chiaradia, M., Grégoire, M., Ceuleneer, G., 2019. The
1068 Eastern Makran Ophiolite (SE Iran): evidence for a Late Cretaceous fore-arc oceanic
1069 crust. *International Geology Review*, 61, 1313–1339.
1070 <https://doi.org/10.1080/00206814.2018.1507764>.

1071 Moore, J.G., 1970. Water Content of Basalt Erupted on the ocean floor. Contribution to
1072 Mineralogy and Petrology 28, 272–279, <https://doi.org/10.1007/BF00388949>.

1073 Moore, J.G., Schilling, J.G., 1973. Vesicles, water, and sulfur in Reykjanes Ridge basalts.
1074 Contribution to Mineralogy and Petrology 41, 105–118.
1075 <https://doi.org/10.1007/BF00375036>

1076 Moore, J.G., Clague, D.A., 1992. Volcano growth and evolution of the island of Hawaii.
1077 Geological Society of America Bulletin 104, 1471–1484. [https://doi.org/10.1130/0016-](https://doi.org/10.1130/0016-7606(1992)104<1471:VGAEOT>2.3.CO;2)
1078 [7606\(1992\)104<1471:VGAEOT>2.3.CO;2](https://doi.org/10.1130/0016-7606(1992)104<1471:VGAEOT>2.3.CO;2)

1079 Moslempour, M.E., Khalatbari-Jafari, M., Ghaderi, M., 2015. Petrology, Geochemistry and
1080 Tectonics of the Extrusive Sequence of Fannuj-Maskutan Ophiolite, Southeastern Iran.
1081 Journal Geological Society of India 85, 604-618.

1082 Omrani, H., Moazzen, M., Oberhänsli, R., Moslempour, M.E., 2017. Iranshahr blueschist:
1083 subduction of the inner Makran oceanic crust. Journal of Metamorphic Geology 35,
1084 373-392.

1085 Pearce J.A., 1996. A user's guide to basalt discrimination diagrams. In: Bailes, A.H.,
1086 Christiansen, E.H., Galley, A.G., Jenner, G.A., Keith, J.D., Kerrich, R., Lentz, D.R.,
1087 Leshner, C.M., Lucas, S.B., Ludden, J.N., Pearce, J.A., Peloquin, S.A., Stern, R.A.,
1088 Stone, W.E., Syme, E.C., Swinden, H.S., Wyman, D.A. (Eds.), Trace element
1089 geochemistry of volcanic rocks: applications for massive sulphide exploration. Short
1090 Course Notes. Geological Association of Canada 12, 79-113.

1091 Pearce, J.A., 2008. Geochemical fingerprinting of oceanic basalts with applications to
1092 ophiolite classification and the search for Archean oceanic crust. Lithos 100, 14–48,
1093 <https://doi.org/10.1016/j.lithos.2007.06.016>.

1094 Pearce, J.A., Norry, M.J., 1979. Petrogenetic implications of Ti, Zr, Y, and Nb variations in
1095 volcanic rocks. Contributions to Mineralogy and Petrology 69, 33-47.

1096 Pirmia, T., Saccani, E., Torabi, G., Chiari, M., Gorican, S., Barbero, E., 2020. Cretaceous
1097 tectonic evolution of the Neo-Tethys in Central Iran: Evidence from petrology and age
1098 of the Nain-Ashin ophiolitic basalts. *Geoscience Frontiers*, 11, 57–81,
1099 <https://doi.org/10.1016/j.gsf.2019.02.008>

1100 Platt, J.P., Leggett, J.K., Young, J., Raza, H., Alam, S., 1985. Large-scale sediment
1101 underplating in the Makran accretionary prism, southwest Pakistan. *Geology* 13, 507,
1102 [https://doi.org/10.1130/0091-7613\(1985\)13<507:LSUITM>2.0.CO;2](https://doi.org/10.1130/0091-7613(1985)13<507:LSUITM>2.0.CO;2)

1103 Regelous, M., Hofmann, A.W., Abouchami W., Galer, S.J.G., 2003. Geochemistry of Lavas
1104 from the Emperor Seamounts, and the Geochemical Evolution of Hawaiian Magmatism
1105 from 85 to 42 Ma. *Journal of Petrology* 44, 113–140,
1106 <https://doi.org/10.1093/petrology/44.1.113>.

1107 Riaz, M.S., Bin, S., Naeem, S., Kai, W., Xie, Z., Gilani, S.M.M., Ashraf, U., 2019. Over 100
1108 years of faults interaction, stress accumulation, and creeping implications, on Chaman
1109 Fault System, Pakistan. *International Journal of Earth Sciences* 108, 1351–1359,
1110 <https://doi.org/10.1007/s00531-019-01710-0>.

1111 Robertson, A.H.F., 2007. Overview of tectonic settings related to the rifting and opening of
1112 Mesozoic ocean basins in the Eastern Tethys: Oman, Himalayas and Eastern
1113 Mediterranean regions. *Geological Society of London Special Publications* 282, 325–
1114 388, <https://doi.org/10.1144/SP282.15>.

1115 Rolland, Y., Galoyan, G., Sosson, M., Melkonyan, R., Avagyan, A., 2010. The Armenian
1116 Ophiolite: insights for Jurassic back-arc formation, Lower Cretaceous hot spot
1117 magmatism and Upper Cretaceous obduction over the South Armenian Block.
1118 *Geological Society of London Special Publications* 340, 353–382,
1119 <https://doi.org/10.1144/SP340.15>.

1120 Rolland, Y., Hässig, M., Bosch, D., Bruguier, O., Melis, R., Galoyan, G., Topuz, G.,
1121 Sahakyan, L., Avagyan, A., Sosson, M., 2020. The East Anatolia–Lesser Caucasus
1122 ophiolite: An exceptional case of large-scale obduction, synthesis of data and numerical
1123 modelling. *Geoscience Frontiers* 11, 83–108, <https://doi.org/10.1016/j.gsf.2018.12.009>.

1124 Saccani, E., Allahyari, K., Beccaluva, L., Bianchini, G., 2013. Geochemistry and petrology of
1125 the Kermanshah ophiolites (Iran): Implication for the interaction between passive
1126 rifting, oceanic accretion, and OIB-type components in the Southern Neo-Tethys Ocean.
1127 *Gondwana Research* 24, 392–411, <https://doi.org/10.1016/j.gr.2012.10.009>.

1128 Saccani, E., 2015. A new method of discriminating different types of post-Archean ophiolitic
1129 basalts and their tectonic significance using Th-Nb and Ce-Dy-Yb systematics.
1130 *Geoscience Frontiers* 6, 481-501.

1131 Saccani, E., Delavari, M., Dolati, A., Marroni, M., Pandolfi, L., Chiari, M., Barbero E., 2018.
1132 New insights into the geodynamics of Neo-Tethys in the Makran area: Evidence from
1133 age and petrology of ophiolites from the Coloured Mélange Complex (SE Iran).
1134 *Gondwana Research* 62, 306-327.

1135 Safonova, I., 2008. Geochemical Evolution of Intraplate Magmatism in the Paleo-Asian
1136 Ocean from the Late Neoproterozoic to the Early Cambrian. *Petrology* 16, 492-511.

1137 Safonova, I., 2017. Juvenile versus recycled crust in the Central Asian Orogenic Belt:
1138 Implications from ocean plate stratigraphy, blueschist belts and intra-oceanic arcs.
1139 *Gondwana Research* 47, 6-27, <http://dx.doi.org/10.1016/j.gr.2016.09.003>.

1140 Safonova, I.Y., Santosh, M., 2014. Accretionary complexes in the Asia-Pacific region:
1141 Tracing archives of ocean plate stratigraphy and tracking mantle plumes. *Gondwana*
1142 *Research* 25, 126–158, <https://doi.org/10.1016/j.gr.2012.10.008>.

1143 Safonova, I., Maruyama, S., Kojima, S., Komiya, T., Krivonogov, S., Koshida, K., 2016.
1144 Recognizing OIB and MORB in accretionary complexes: A new approach based on

1145 ocean plate stratigraphy, petrology and geochemistry. *Gondwana Research* 33, 92–114,
1146 <https://doi.org/10.1016/j.gr.2015.06.013>.

1147 Samimi Namin, M., 1982. Geological Map of Taherui 1:250000 Scale. Tehran: Ministry of
1148 Mines and Metal, Geological Survey of Iran.

1149 Samimi Namin, M., 1983. Geological Map of Minab 1:250000 Scale. Tehran: Ministry of
1150 Mines and Metal, Geological Survey of Iran.

1151 Sepidbar, F., Lucci, F., Biabangard, H., Zaki Khedr, M., Jiantang, P., 2020. Geochemistry and
1152 tectonic significance of the Fannuj-Maskutan SSZ-type ophiolite (Inner Makran, SE
1153 Iran). *International Geology Review*, <https://doi.org/10.1080/00206814.2020.1753118>

1154 Shervais, J.W., 1982. Ti-V plots and the petrogenesis of modern and ophiolitic lavas. *Earth
1155 and Planetary Science Letters* 59, 101–118, [https://doi.org/10.1016/0012-](https://doi.org/10.1016/0012-821X(82)90120-0)
1156 [821X\(82\)90120-0](https://doi.org/10.1016/0012-821X(82)90120-0).

1157 Sun, S.S., McDonough, W.F., 1989. Chemical and isotopic systematics of oceanic basalts:
1158 implications for mantle composition and processes. In: Saunders, A.D., Norry, M.J.
1159 (Eds.), *Magmatism in the Ocean Basins*. Geological Society of London Special
1160 Publication 42, 313-345.

1161 Yang, G.X., Li, Y.J., Xiao, W.J., Tong, L.L., 2015. OIB-type rocks within West Junggar ophiolitic
1162 mélanges: evidence for the accretion of seamounts. *Earth-Science Reviews* 150, 477-496,
1163 <http://dx.doi.org/10.1016/j.earscirev.2015.09.002>.

1164 Yang G.X., Li Y.J., Tong L.L., Wang Z.P., Duan, F.H., Xu, Q., Li, H., 2019. An overview of oceanic
1165 island basalts in accretionary complexes and seamounts accretion in the western Central Asian
1166 Orogenic Belt. *Journal of Asian Earth Sciences* 179, 385-398.

1167 Wan, B., Wang, X., Liu, X., Cai, K., Xiao, W., Mitchell, R.N., 2020. Long-lived seamount subduction
1168 in ancient orogens: Evidence from the Paleozoic South Tianshan. *Geology*.
1169 <https://doi.org/10.1130/G48547.1>

1170 White, W.M., 2010. Oceanic Island Basalts and Mantle Plumes: The Geochemical
1171 Perspective. *Annual Review of Earth and Planetary Sciences* 38, 133–160,
1172 <https://doi.org/10.1146/annurev-earth-040809-152450>.
1173 Winchester, J.A., Floyd, P.A., 1977. Geochemical discrimination of different magma series
1174 and their differentiation products using immobile elements. *Chemical Geology* 20, 325-
1175 343.
1176 Workman, R.K., Hart, S.R., 2005. Major and trace element composition of the depleted
1177 MORB mantle (DMM). *Earth and Planetary Science Letters* 231, 53-72.

1178
1179

1180

1181

1182

1183

1184

1185 **Table captions**

1186

1187 **Table 1.** Major (wt.%) and trace (ppm) element composition of representative volcanic
1188 and metavolcanic rocks from the western part of the Durkan Complex. Abbreviations: bas:
1189 basalt; bas and: basaltic andesite; tra: trachyte; a-rhy: alkali-rhyolite; XRF: X-ray
1190 fluorescence spectrometry; ICP-MS: inductively coupled plasma-mass spectrometry; n.d.:
1191 not detected. $Mg\# = 100 \times MgO / (MgO + FeO)$. $Fe_2O_3 = 0.15 \times FeO$. Normalizing values
1192 for REE ratios from [Sun and McDonough \(1989\)](#). Asterisks indicate samples whose XRF
1193 composition is taken from [Barbero et al. \(2021\)](#).

1194

1195 **Table 2.** Representative analyses of clinopyroxene from basaltic and metabasaltic
1196 rocks from the western part of the Durkan Complex. Atoms per formula units (a.p.f.u.) are
1197 calculated on the bases of four cations. The compositions of Fe³⁺ and Fe²⁺ were calculated
1198 from the measured total FeO according to [Droop \(1987\)](#); $Mg\# = Mg / (Mg + Fe^{2+})$.
1199 Abbreviations, Wo: wollastonite; En: enstatite; Fs: ferrosilite; Acm: Acmite.
1200 Abbreviations, c: core; ec: external part of the core; r: rim.

1201

1202 **Figure caption**

1203

1204 **Figure 1.** a) Simplified tectonic sketch map of the Iranian-Afghan-Pakistani area
1205 (modified from [Khan et al., 2007](#); [Bagheri and Stampfli, 2008](#); [Allahyari et al., 2014](#);
1206 [Mohammadi et al., 2016](#); [Pirnia et al., 2020](#); [Barbero et al., 2020b](#)); b) structural sketch
1207 map showing the different tectono-stratigraphic domains of the Makran Accretionary
1208 Wedge (modified from [Burg et al., 2013](#)); c) simplified geological-structural map of the
1209 North Makran Domain showing the different tectonic units (modified from [Eftekhar-](#)
1210 [Nezhad et al. 1979](#); [Burg, 2018](#); [Samimi Namin, 1982, 1983](#); [Barbero et al., 2020b](#)).

1211

1212 **Figure 2.** Simplified geological map of the western part of the Durkan Complex
1213 (based on [Samimi Namin, 1982](#) and modified according to our original fieldwork and
1214 photointerpretation with satellite images). The locations of the sampled areas are also
1215 shown.

1216

1217 **Figure 3.** a) Schematic stratigraphic column and ages for the three different types of
1218 successions in the western part of the Durkan Complex; b) vesicle volume % vs. depth of
1219 eruption for basalts from the different successions. The different curves indicate the depth-

1220 vesicles percent for tholeiitic (solid line, from [Moore and Schilling, 1973](#)) and alkaline
1221 (dashed line, from [Moore, 1970](#)) volcanic rocks. Modified from [Barbero et al., \(2021\)](#).

1222
1223

1224 **Figure 4.** Nb/Y vs. Zr/Ti discrimination diagram of [Winchester and Floyd \(1977\)](#)
1225 modified by [Pearce \(1996\)](#) for volcanic and metavolcanic rocks from the western part of
1226 the Durkan Complex.

1227

1228 **Figure 5.** N-MORB normalized incompatible element patterns (left column) and
1229 Chondrite-normalized rare earth element patterns (right column) for volcanic and
1230 metavolcanic rocks from the part of the Durkan Complex. Normalizing values are from
1231 [Sun and McDonough \(1989\)](#). Compositions of average plume-influenced mid-ocean ridge
1232 basalt (P-MORB) from the Southwest Indian Ridge and typical alkaline oceanic within-
1233 plate basalt (OIB) are from [Janney et al. \(2005\)](#) and [Sun and McDonough \(1989\)](#),
1234 respectively.

1235

1236 **Figure 6.** Chondrite-normalized $(Sm/Yb)_N$ vs. $(La/Yb)_N$ (a), $(Sm/Yb)_N$ vs. $(Sm/Dy)_N$
1237 (b), and $(La/Yb)_N$ vs. Yb_N (c) diagrams for the volcanic and metavolcanic rocks of the
1238 western part of the Durkan Complex. Normalizing values are from [Sun and McDonough](#)
1239 [\(1989\)](#).

1240

1241 **Figure 7.** N-MORB normalized Th vs. Nb discrimination diagram of [Saccani \(2015\)](#)
1242 for volcanic and metavolcanic rocks from the western part of the Durkan Complex.
1243 Vectors indicate the trends of compositional variations due to the main petrogenetic
1244 processes. Abbreviations, AFC: assimilation-fractional crystallization; OIB-CE: ocean

1245 island-type (plume-type) component enrichment; FC: fractional crystallization; MORB:
1246 mid-ocean ridge basalt; N-: normal type; E-: enriched type; P-: plume type; D-: depleted
1247 type; IAT: island arc tholeiite; CAB: calc-alkaline basalt; AB: alkaline oceanic within-
1248 plate basalt; MTB: medium titanium basalt. Normalizing values, as well as the composition
1249 of typical N-MORB (white star), E-MORB (grey star), and OIB (black star) are from [Sun
1250 and McDonough \(1989\)](#).

1251
1252 **Figure 8.** Diagram showing the variation of TiO_2 , CaO , and Na_2O contents vs. Mg\#
1253 for clinopyroxenes from the basaltic and metabasaltic rocks of the western part of the
1254 Durkan Complex. Arrows represent the average trends of variation for clinopyroxene from
1255 the different geochemical groups of rocks.

1256
1257 **Figure 9.** a) Ti vs. $(\text{Ca} + \text{Na})$ and b) $(\text{Ti} + \text{Cr})$ vs. Ca discrimination diagrams of
1258 [Leterrier et al. \(1982\)](#) showing the compositions of clinopyroxenes from the volcanic and
1259 metavolcanic rocks from the western the part of the Durkan Complex.

1260
1261 **Figure 10.** Compositions of clinopyroxenes from the basaltic and metabasaltic rocks
1262 from the western the part of the Durkan Complex plotted in the $\text{TiO}_2\text{-Na}_2\text{O-SiO}_2/100$
1263 diagram for discriminating clinopyroxenes in basalts from different oceanic settings
1264 ([Beccaluva et al., 1989](#)). Abbreviations, E-MORB: enriched mid-ocean ridge basalt; N-
1265 MORB: normal mid-ocean ridge basalt; WOPB: within oceanic plate basalts; ICB: Iceland
1266 basalts; and SSZ: supra-subduction zone basalts.

1267
1268 **Figure 11.** Variation of TiO_2 (a), CaO (b), and Al_2O_3 (c) contents in clinopyroxenes
1269 from basaltic and metabasaltic rocks from the western the part of the Durkan Complex vs.

1270 the Nb/Y ratios of their hosting rocks. Only clinopyroxene with Mg# in the range 0.74 –
1271 0.80 are plotted to allow comparison between the different chemical groups.

1272
1273 **Figure 12.** a) Nb vs. Zr and b) Zr/Y vs. Zr/Nb diagrams for volcanic and metavolcanic
1274 rocks from the western part of the Durkan Complex. N-MORB, E-MORB and OIB end-
1275 members are from [Sun and McDonough \(1989\)](#). Fields showing the compositional
1276 variation of different types of basalts from subduction-unrelated ophiolites and modern
1277 oceanic setting are shown for comparison in Panel b) (data from [Saccani et al., 2013](#), [Le](#)
1278 [Roex et al., 1983](#); [Hanan et al., 2000](#); [Chauvet et al., 2011](#)). The dashed line in b)
1279 represents the mixing curve calculated using OIB and N-MORB end-members (from [Le](#)
1280 [Roex et al. 1983](#)).

1281
1282 **Figure 13.** a) Nb/Yb vs. TiO₂/Yb diagram showing the isobaric melting curves for
1283 theoretical mantle sources S1 and S2 calculated for different pressures according to [Pearce](#)
1284 [\(2008\)](#); b) Nb/Yb vs. Th batch melting curve for the theoretical mantle source S1 and S2
1285 calculated for both spinel- and garnet-facies conditions. The dashed line represents the
1286 mixing line of various melt fractions from garnet- and spinel-facies mantle. S1 and S2
1287 represent theoretical mantle sources calculated by assuming different degrees of
1288 enrichment by an OIB-type chemical component ([Lustrino et al., 2002](#)) of a sub-oceanic
1289 slightly depleted lherzolite residual after small volume of MORB melt extraction
1290 (lherzolite ZB2, [Barbero et al., 2020c](#)). Depleted MORB mantle (DMM) and primitive
1291 mantle (PM) compositions are also shown in [Figure 13a](#) (data from [Workman and Hart,](#)
1292 [2005](#) and [Sun and McDonough, 1989](#), respectively). Input parameters (source modes,
1293 melting proportions, and partition coefficients, source compositions) for the model in
1294 [Figure 13b](#) are given in [Supplementary Table S2](#). Volcanic and metavolcanic rocks from

1295 the western part of the Durkan Complex are plotted in both diagrams. The relatively less
1296 fractionated basalts of each rock type are shown with large symbols, whereas other
1297 samples are shown with small, grey symbols.

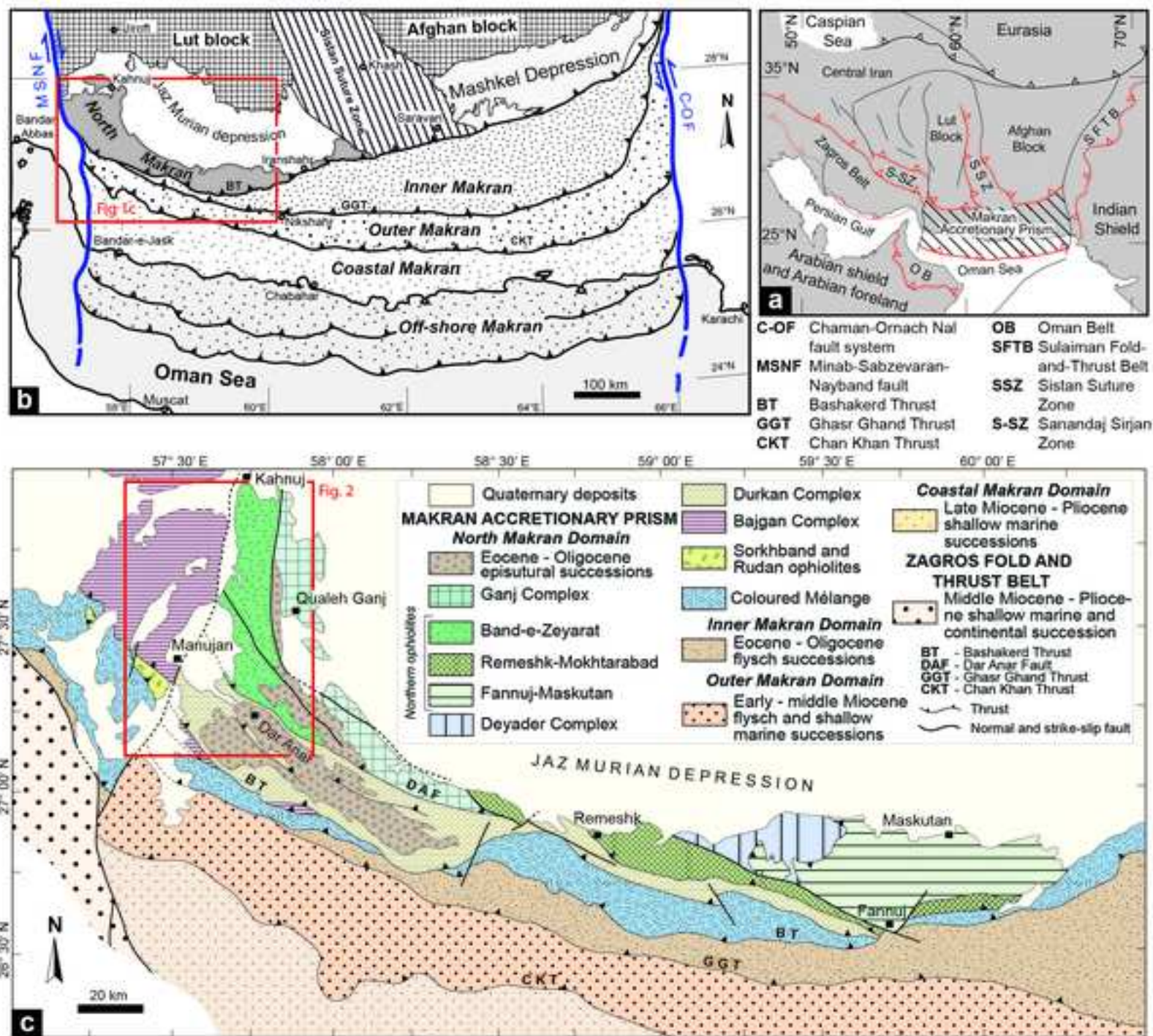
1298

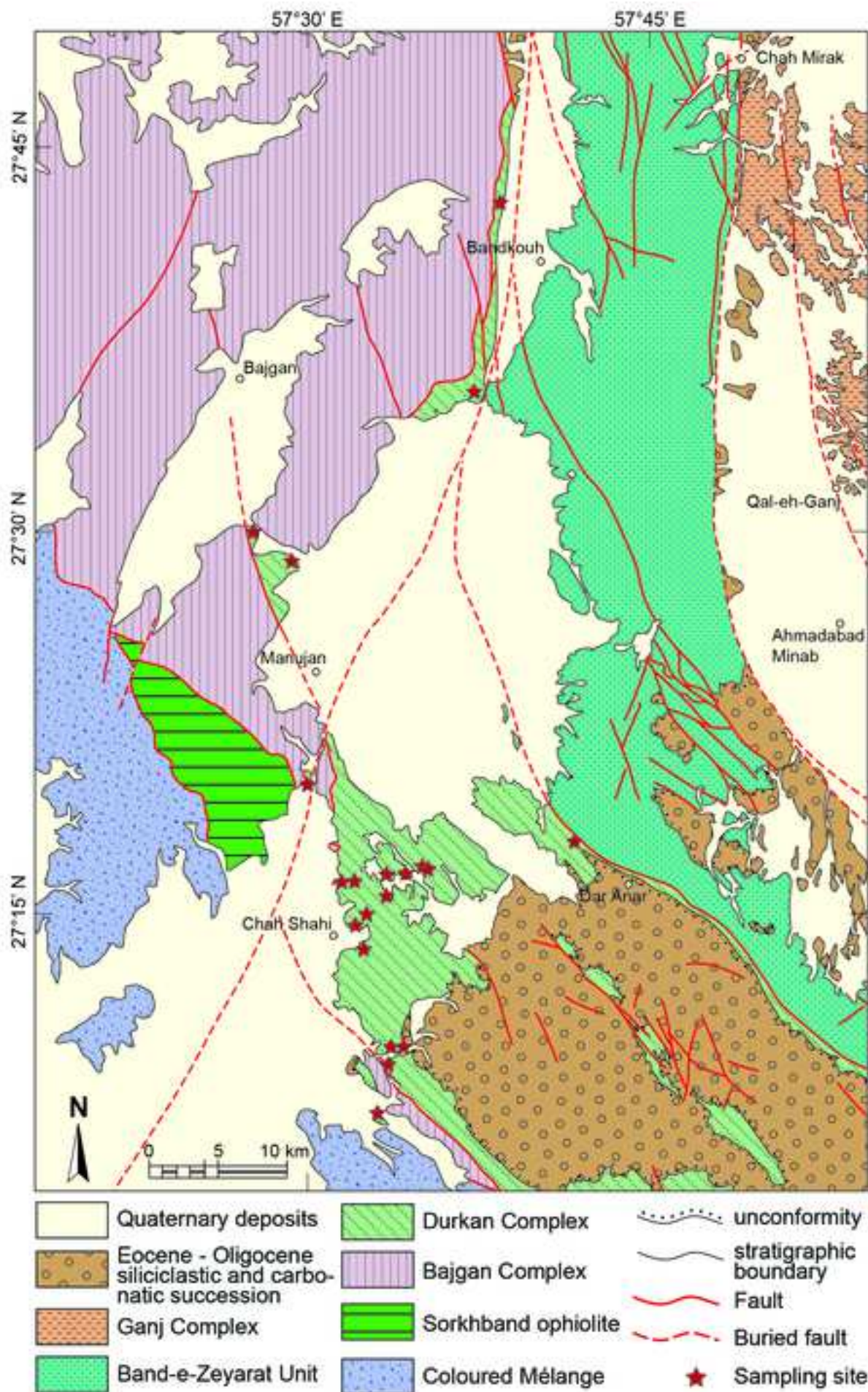
1299 **Figure 14.** Calculated chondrite-normalized (Sun and McDonough, 1989) rare earth
1300 element (REE) liquid composition for parental melts derived from mantle sources S1 and
1301 S2, assuming various degrees of non-modal batch partial melting in the spinel- and garnet-
1302 facies mantle, as well as different proportions of melt fractions from garnet- and spinel-
1303 facies mantle. S1 and S2 represent theoretical mantle sources calculated by assuming
1304 different degrees of enrichment by an OIB-type chemical component (Lustrino et al., 2002)
1305 of a sub-oceanic slightly depleted lherzolite residual after small volume of MORB melt
1306 extraction (lherzolite ZB2, Barbero et al., 2020c). Abbreviations: EM: enriched mantle
1307 source (from Lustrino et al., 2002); DMM: depleted MORB mantle (Workman and Hart,
1308 2005). Input parameters for the REE models (source modes, melting proportions, and
1309 partition coefficients), as well as compositions of the different mantle sources are shown in
1310 Supplementary Table S2. The comparison between the composition of the relatively less
1311 fractionated basalts of Group 1, Group 2a, and Group 2b and the calculated melts are
1312 shown in panels a), b), c), respectively. Representative examples of the mixing of various
1313 melt fractions from garnet- and spinel-facies mantle are shown in a1).

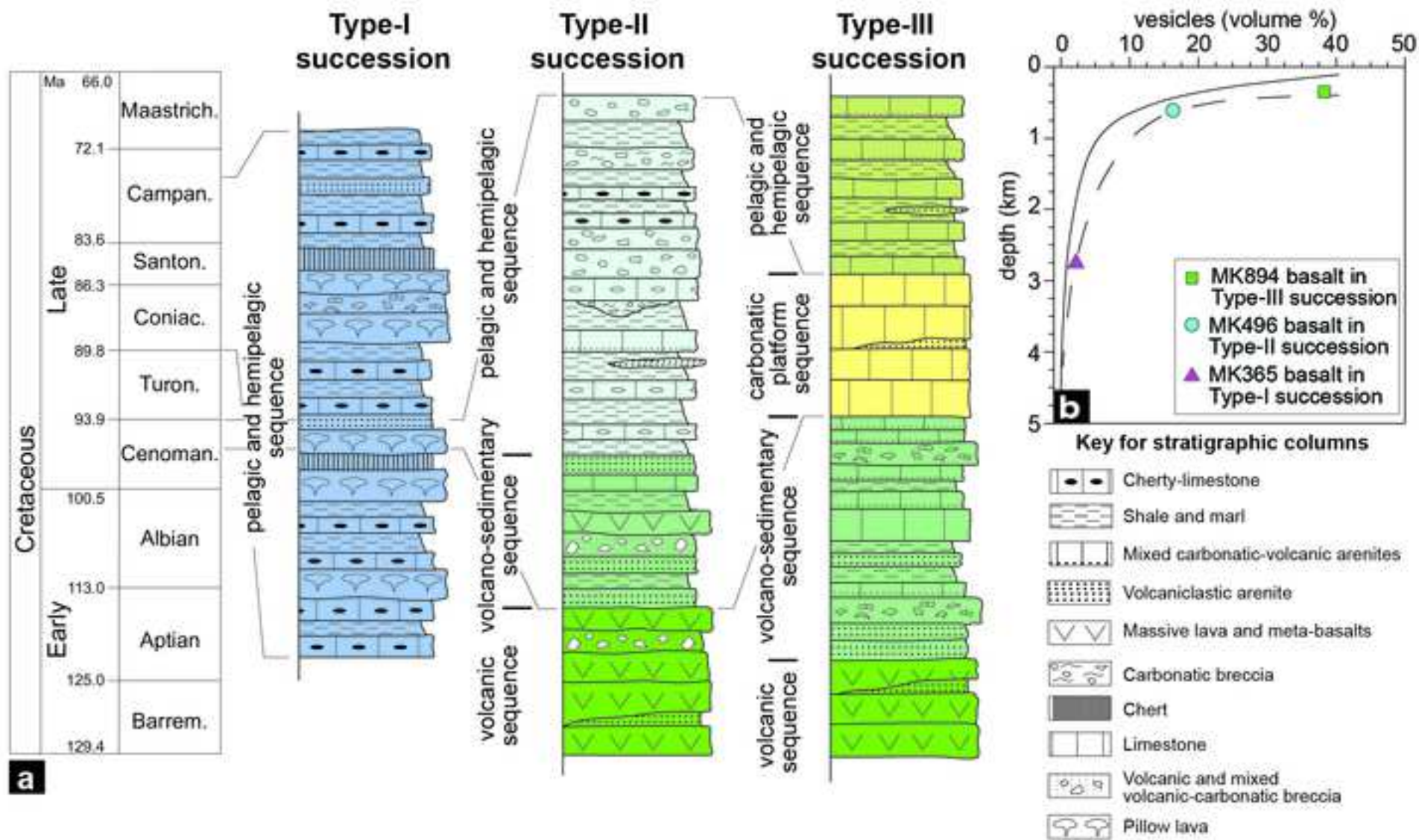
1314

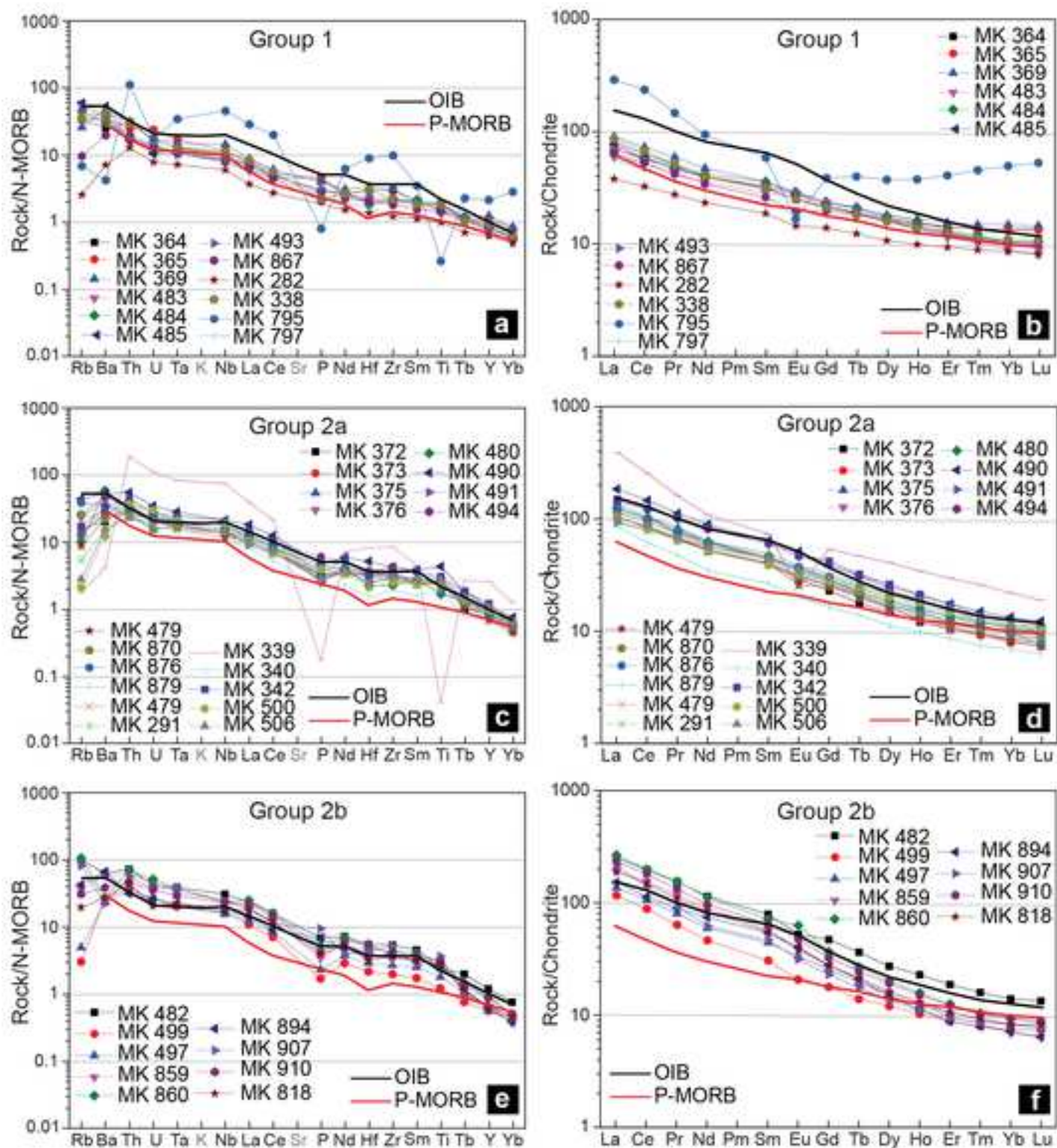
1315 **Figure 15.** Conceptual cartoon showing the petrogenetic processes operating during
1316 the shallow-water (a) and deep-water (b) stages of growth of the Durkan seamounts. The
1317 depositional positions of the different types of successions within the seamount chain is
1318 modified from Barbero et al. (2021). Abbreviations, MORB: mid-oceanic ridge basalt;
1319 OIB: ocean island basalt; S1 and S2: enriched mantle sources derived from different

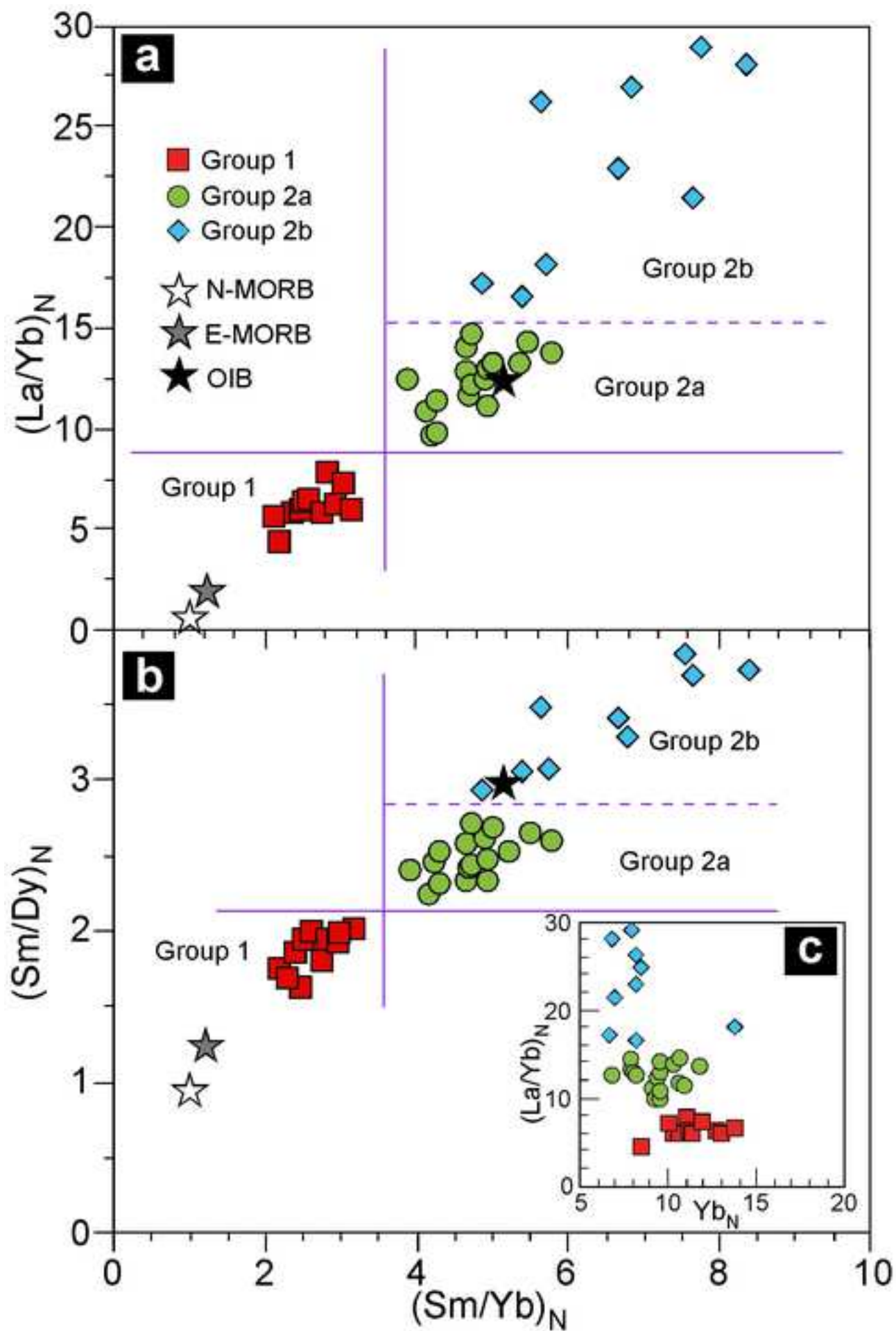
1320 degrees of enrichment by an OIB-type chemical component of a sub-oceanic slightly
1321 depleted lherzolite residual after small volume of MORB melt extraction; spl: spinel; gt:
1322 garnet.

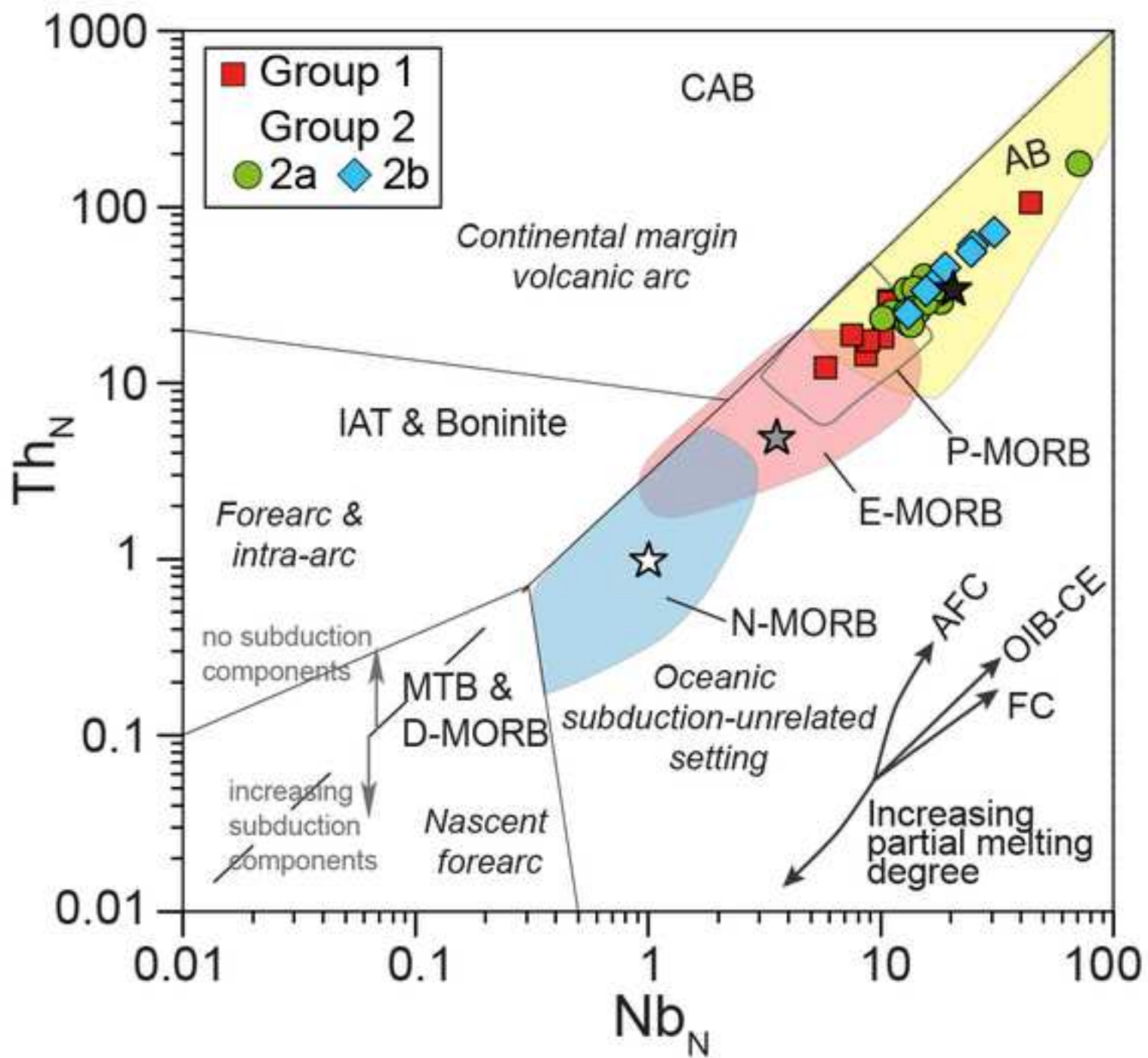


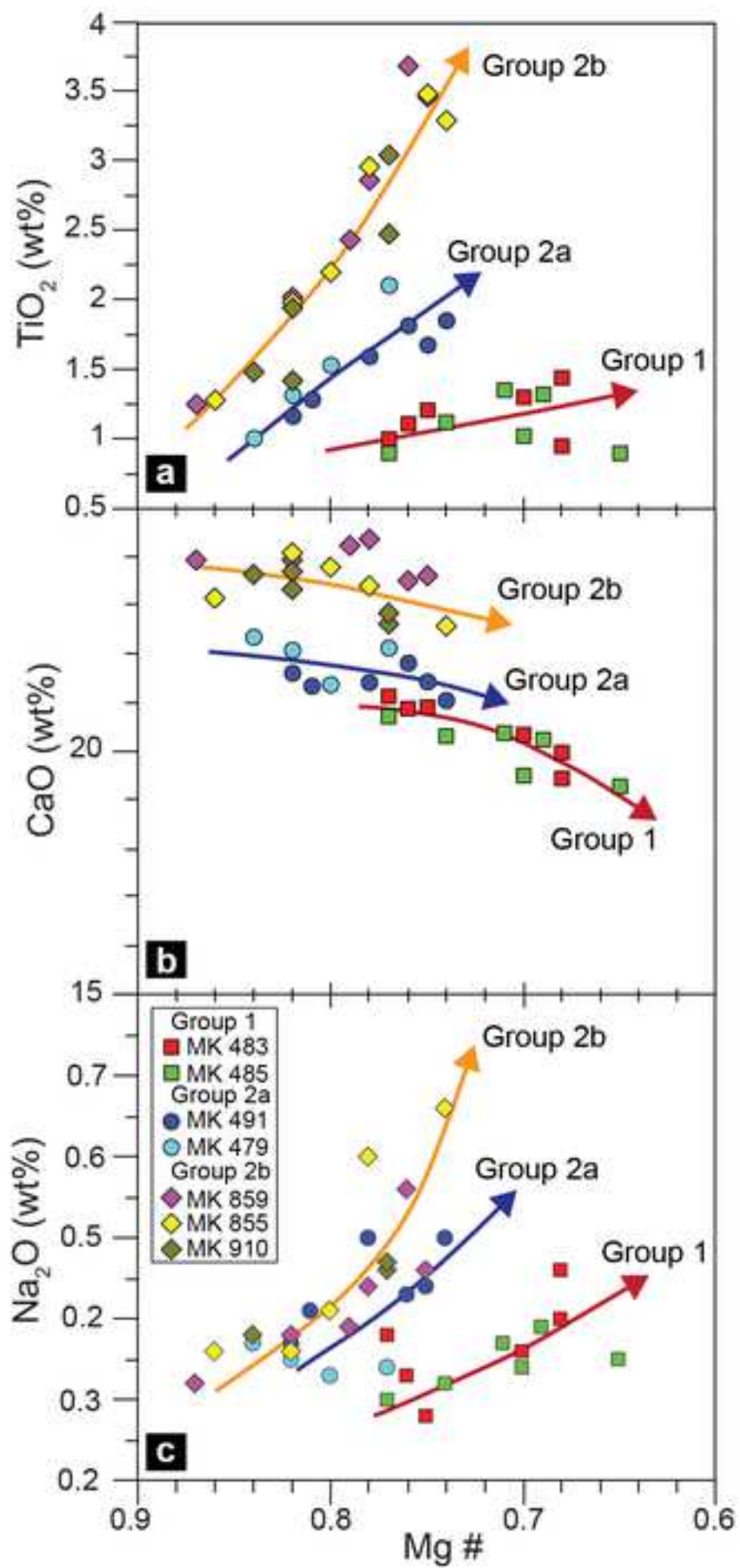


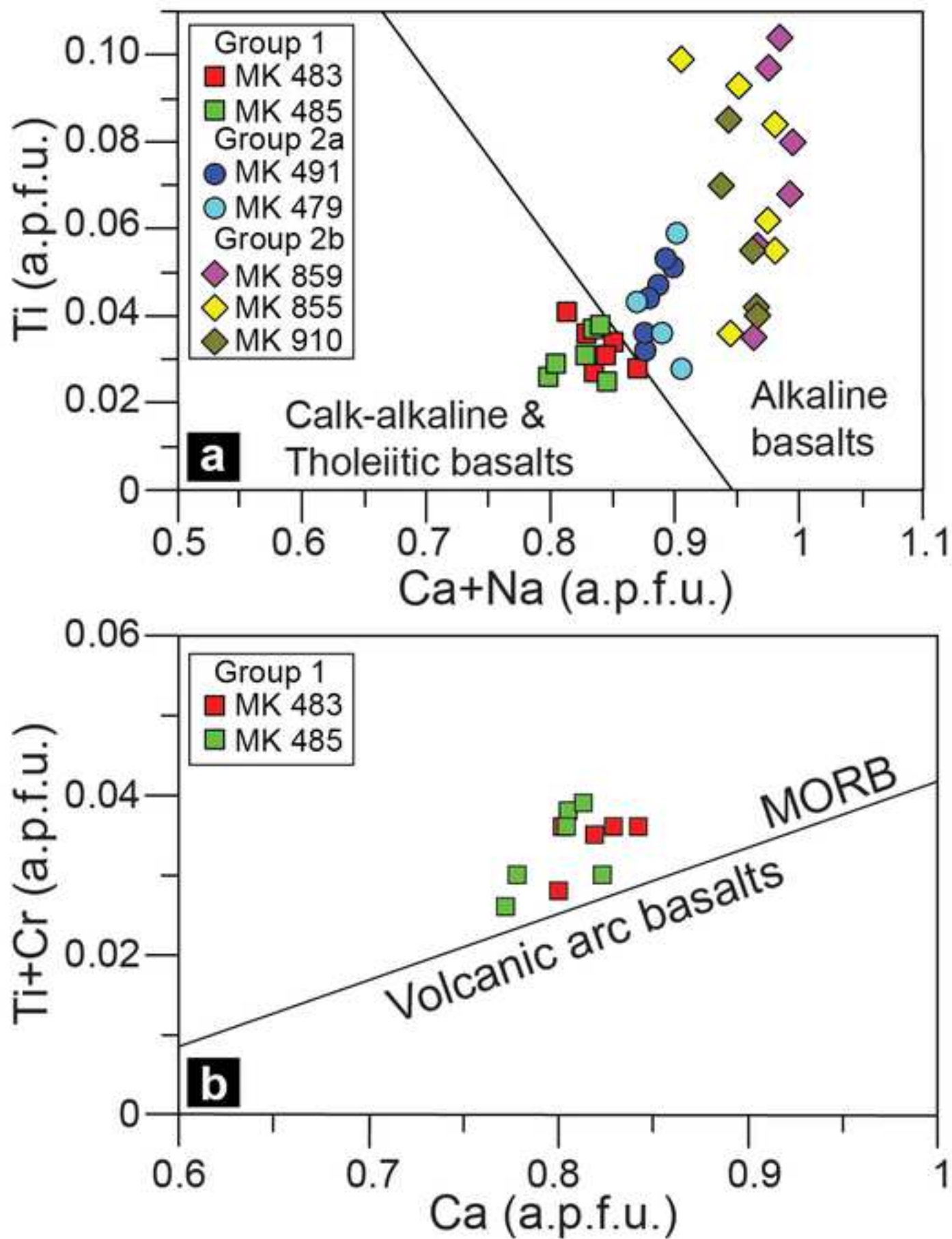


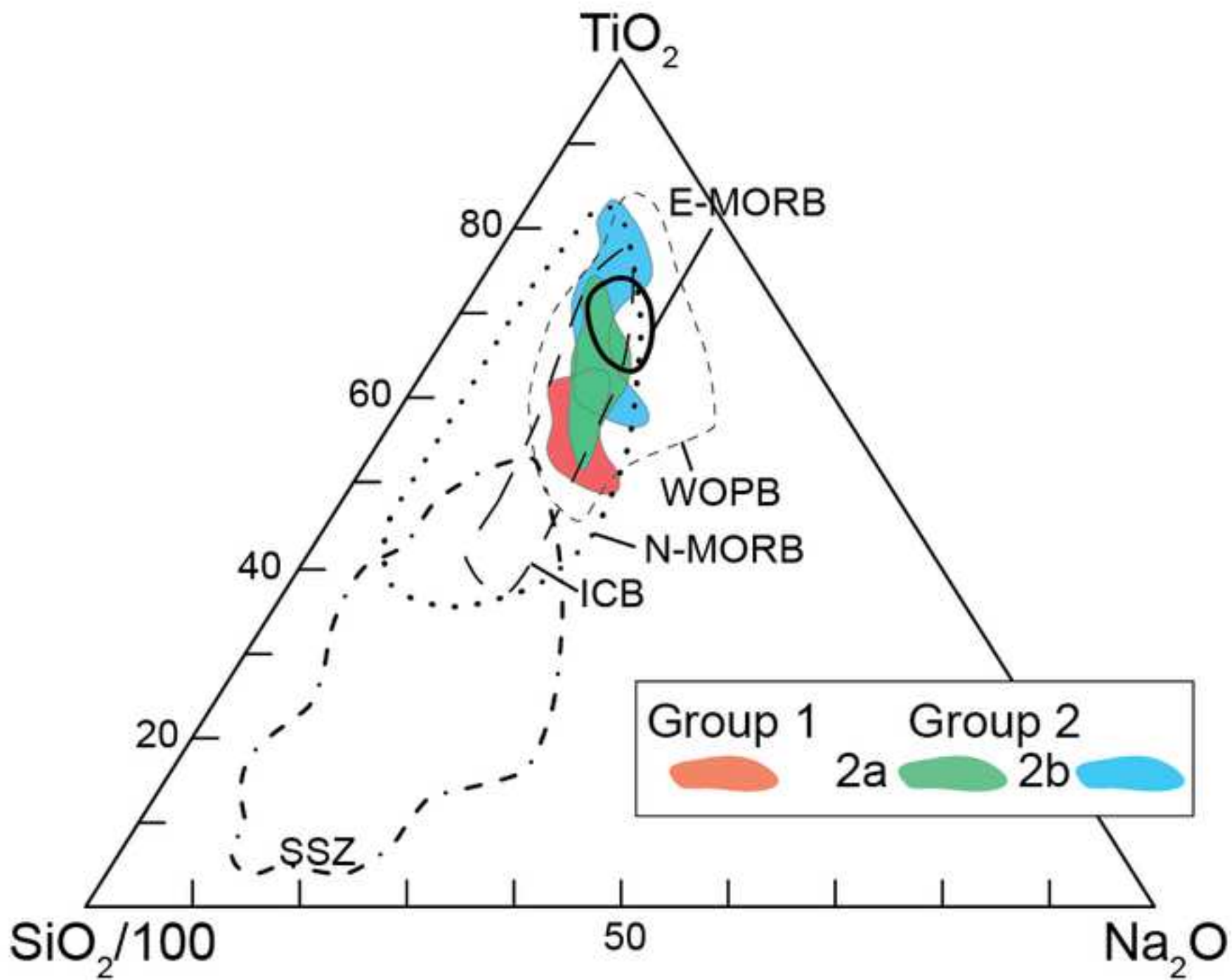


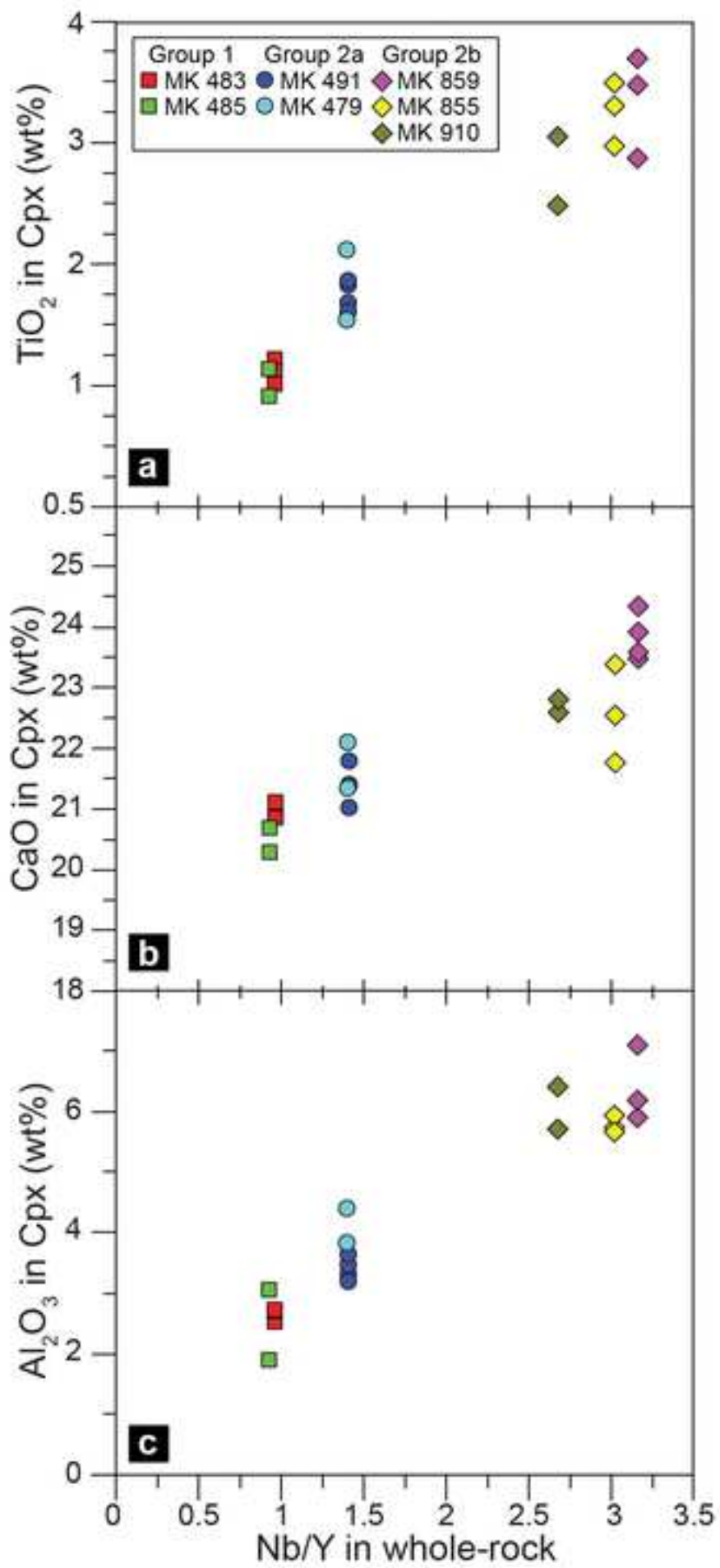


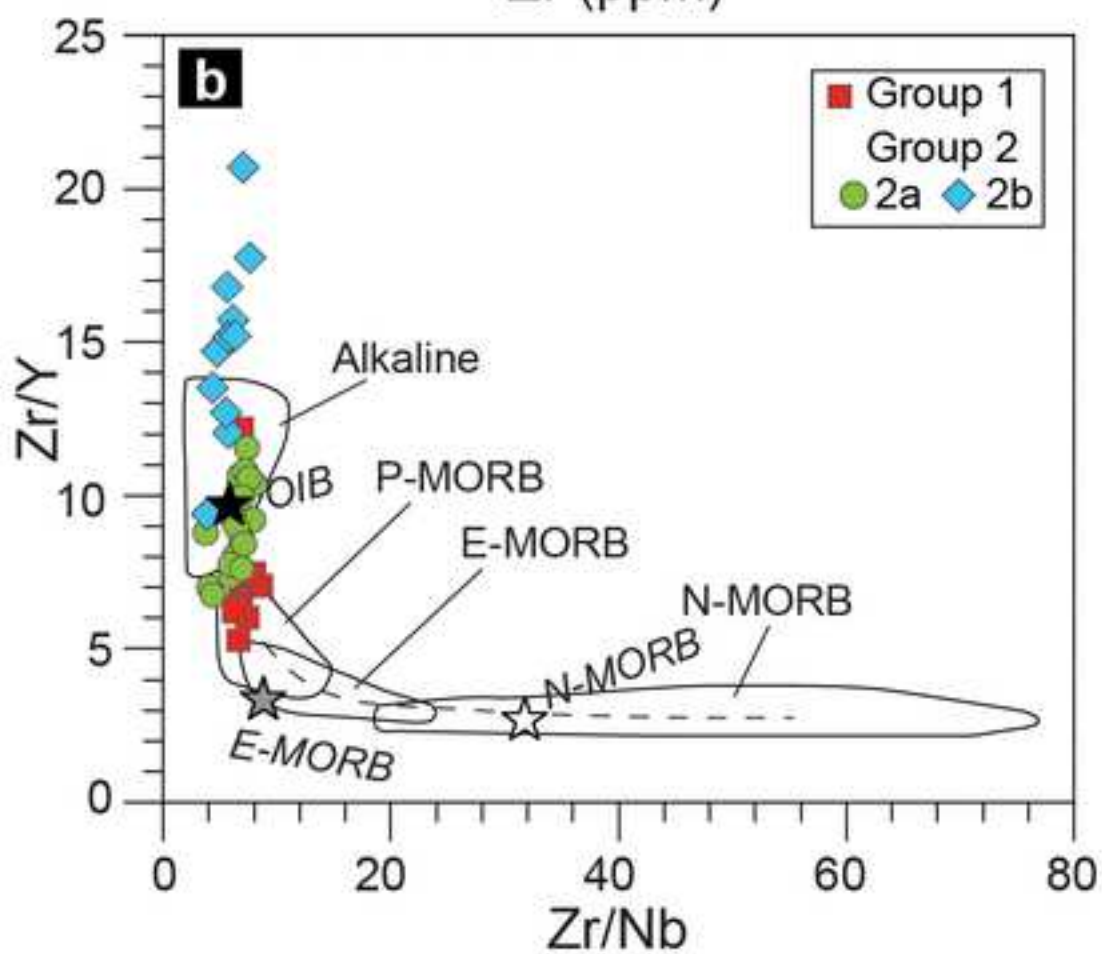
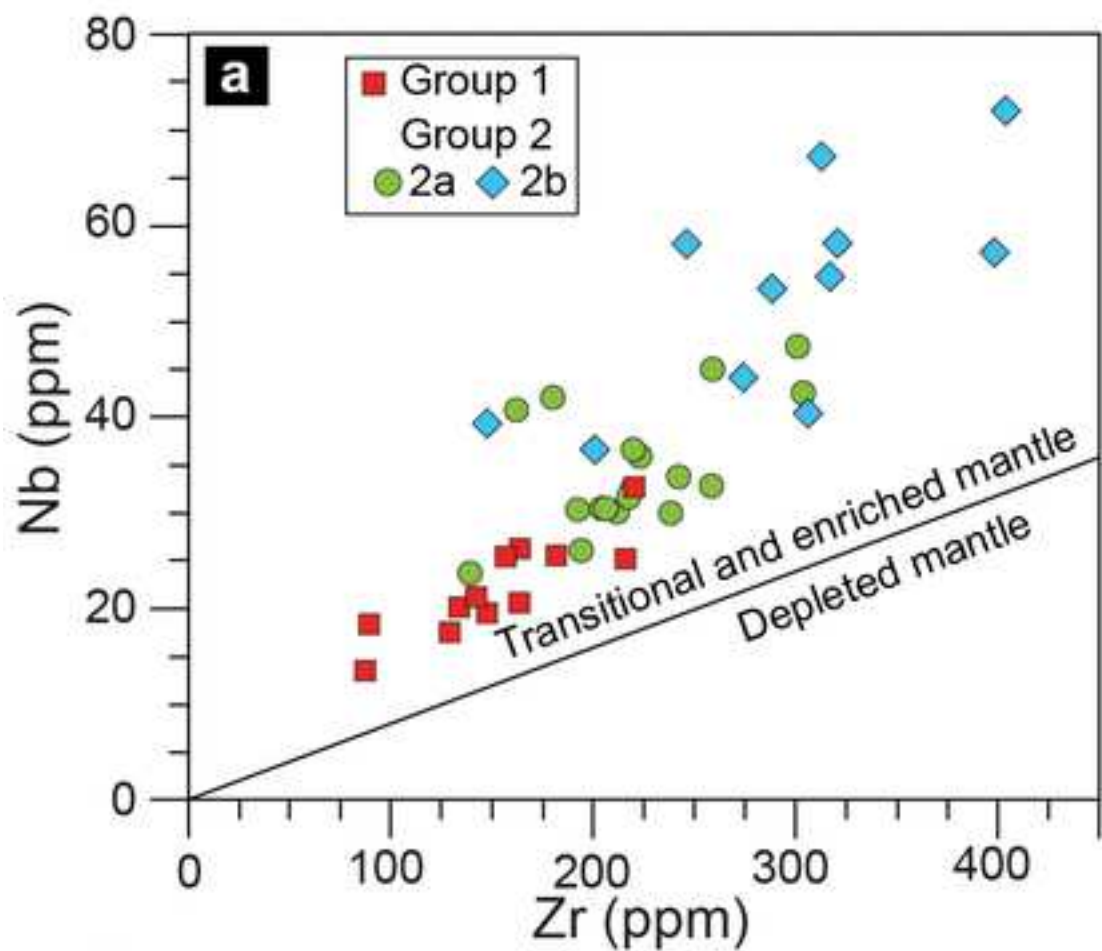


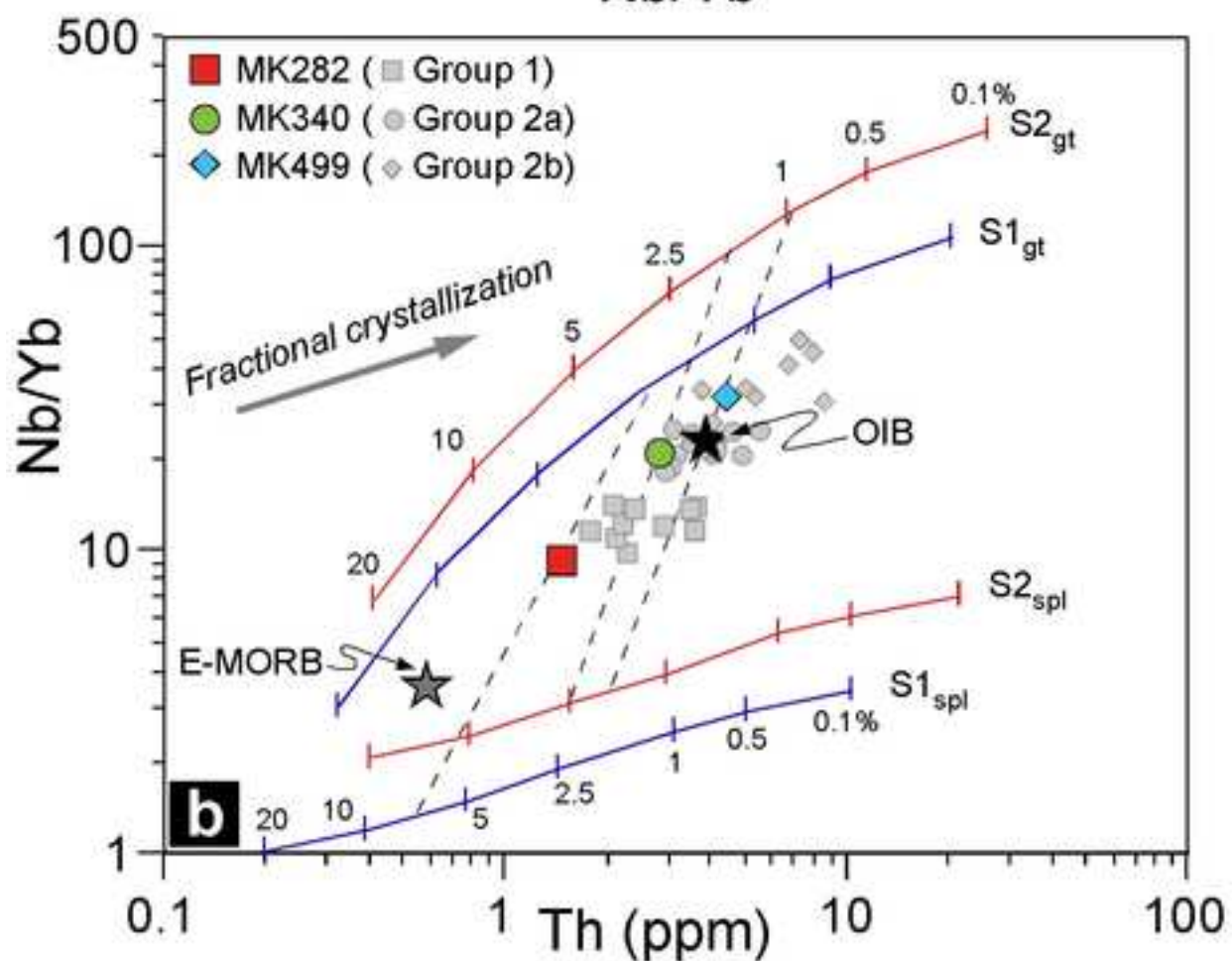
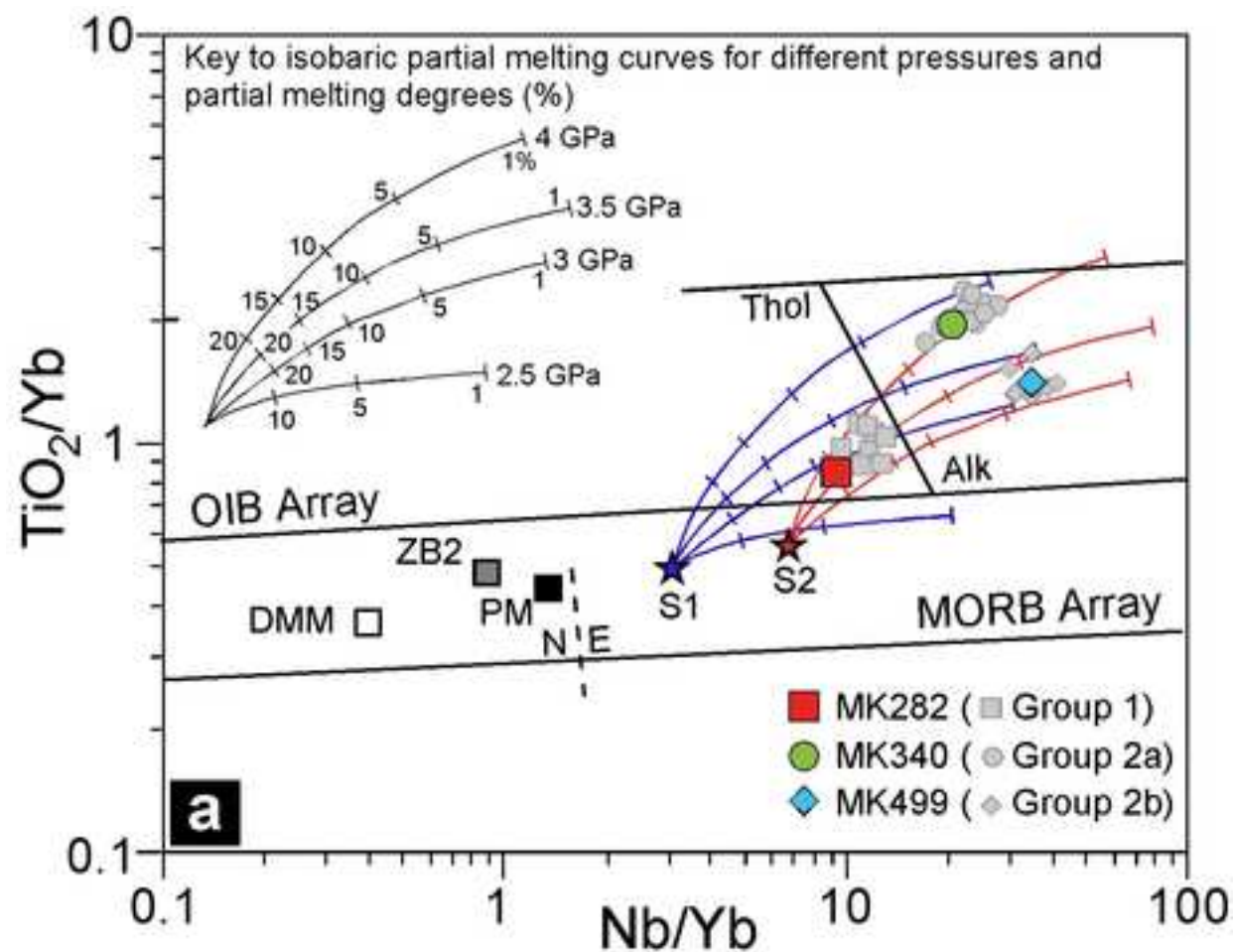


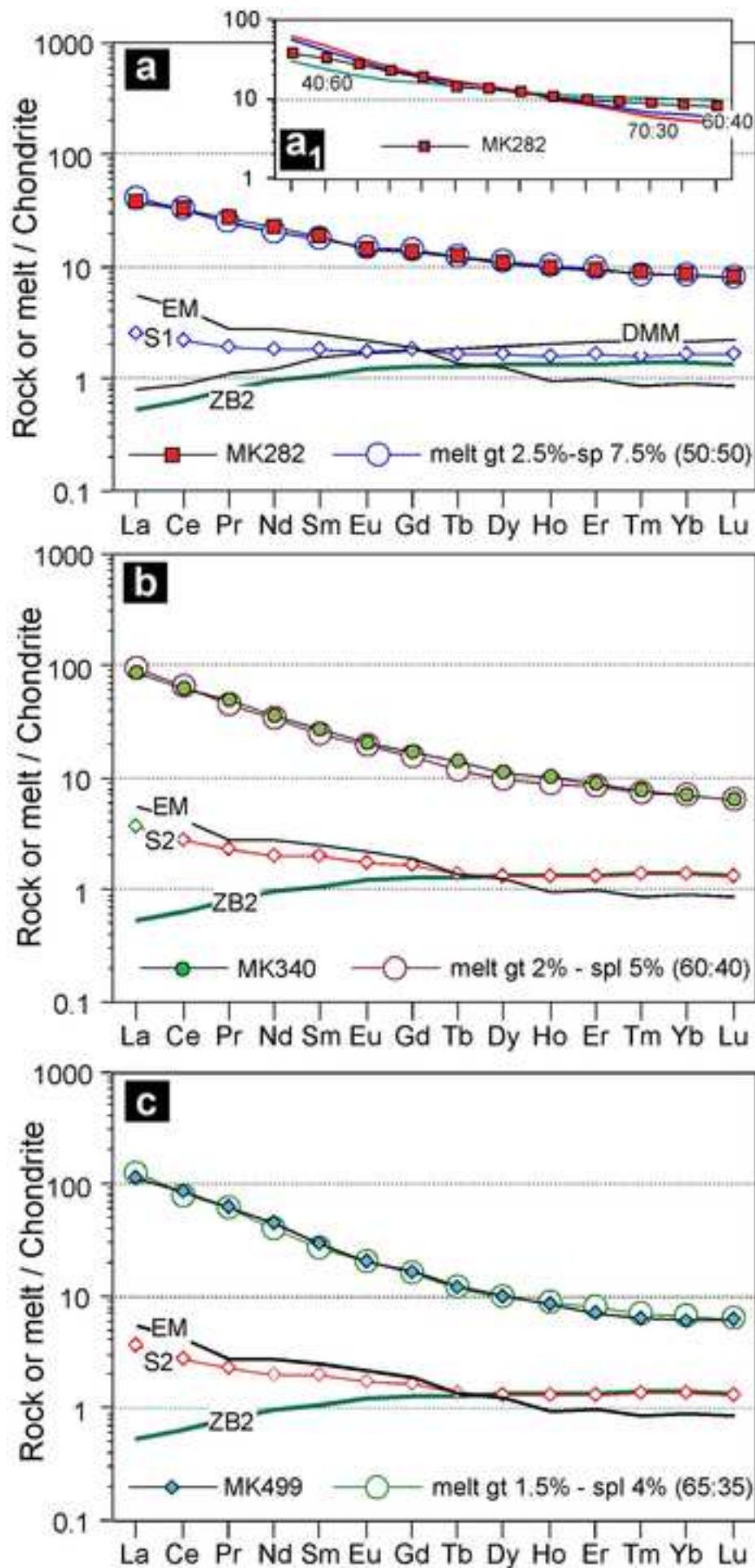


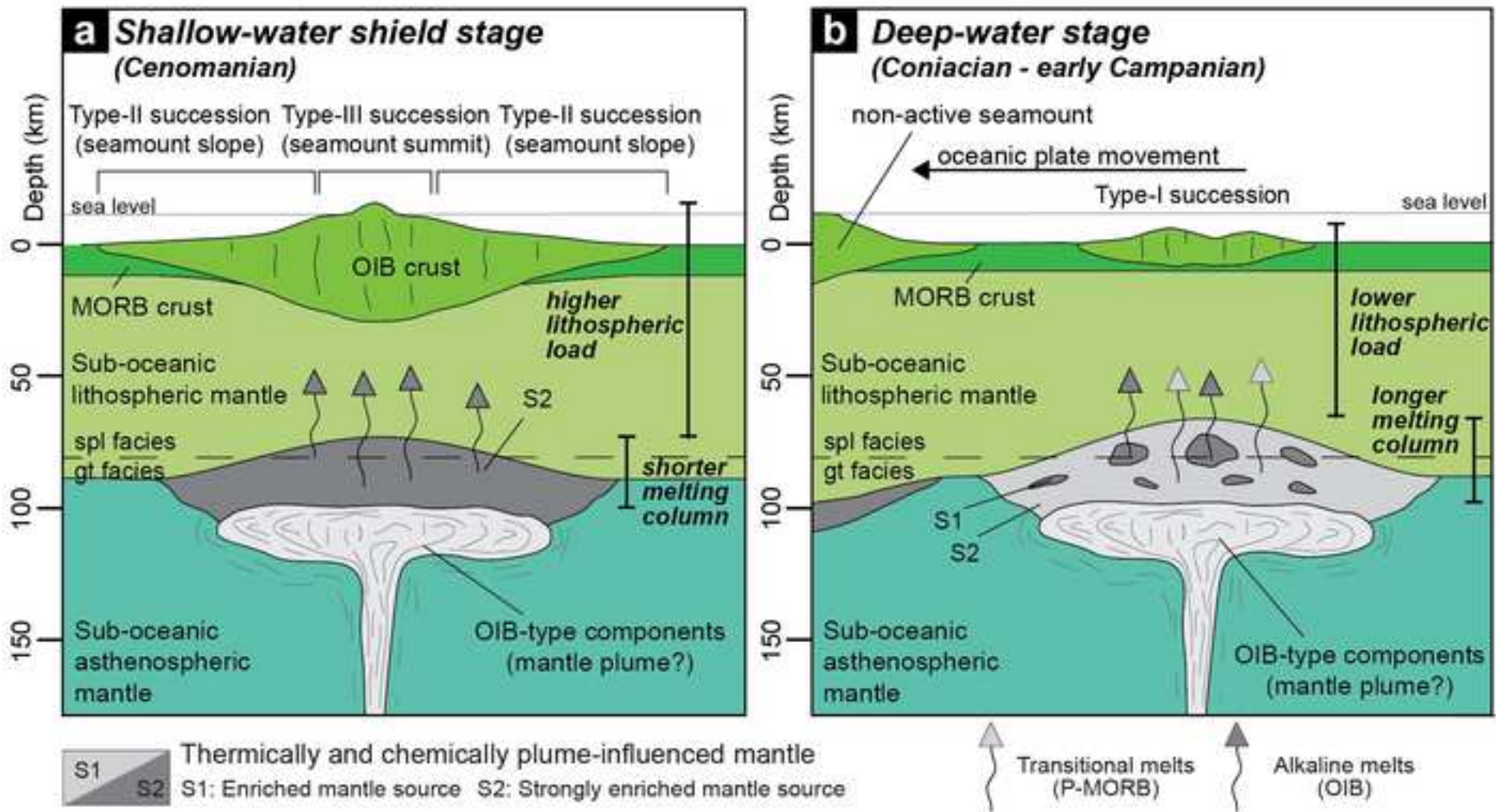


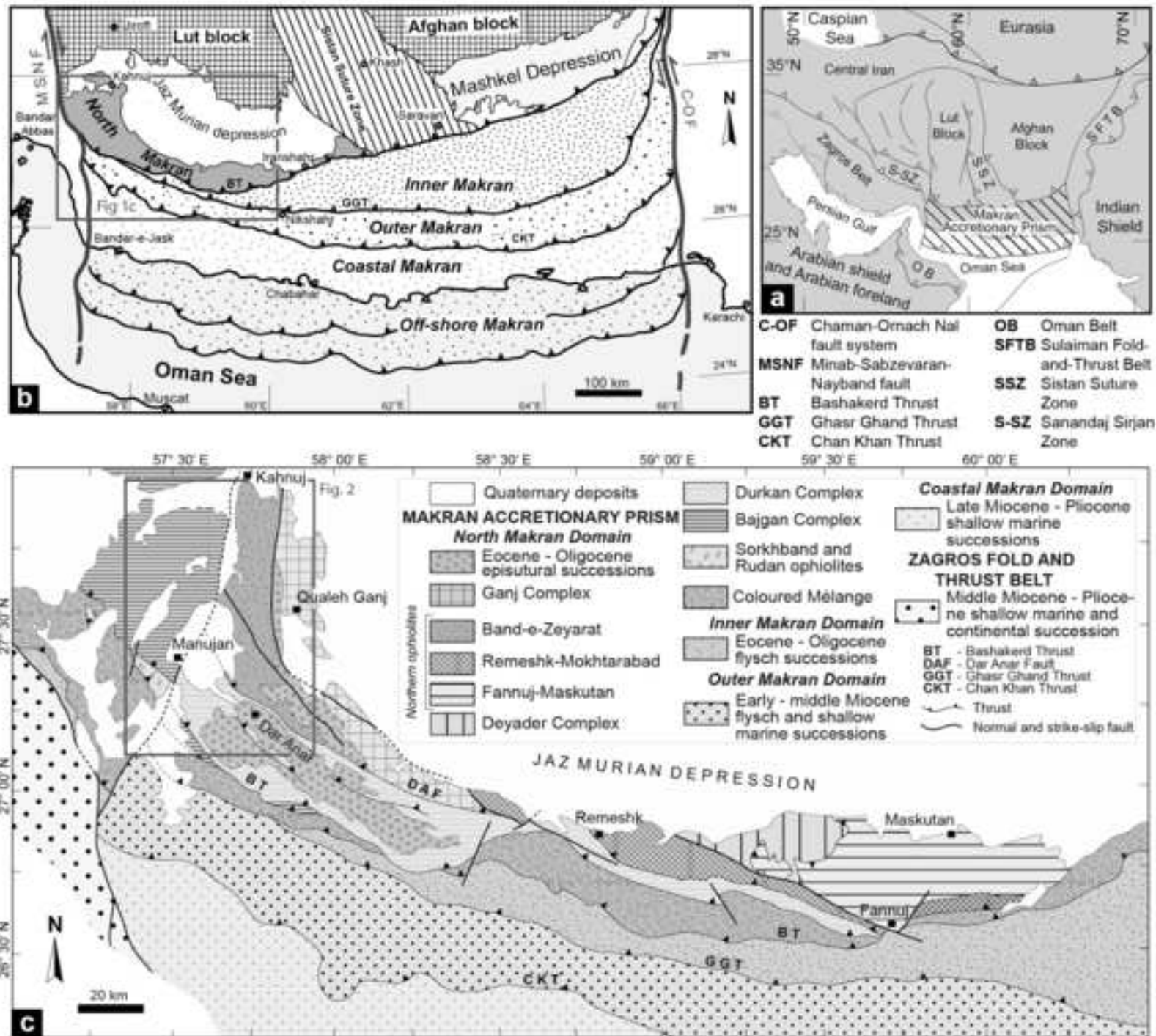


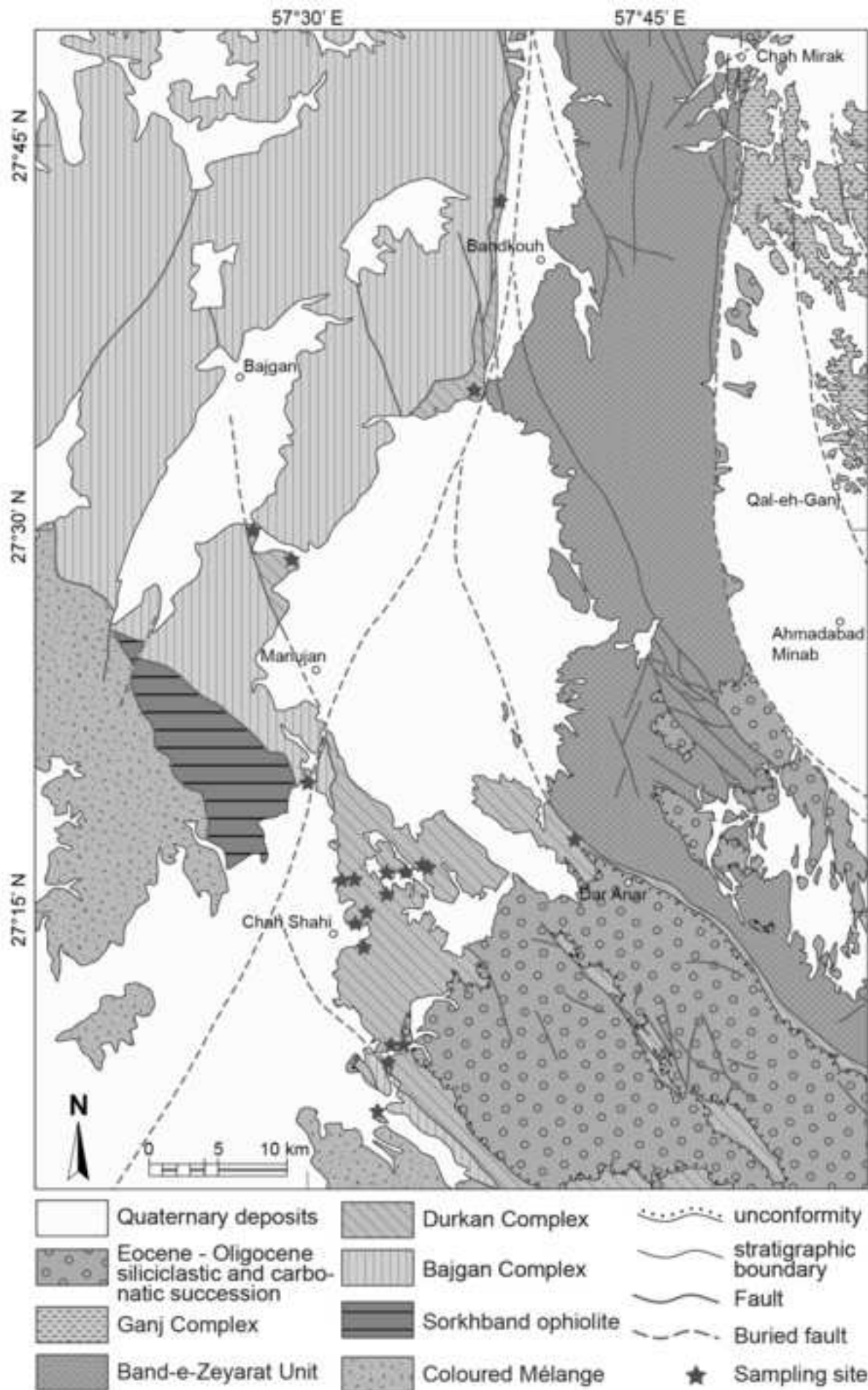


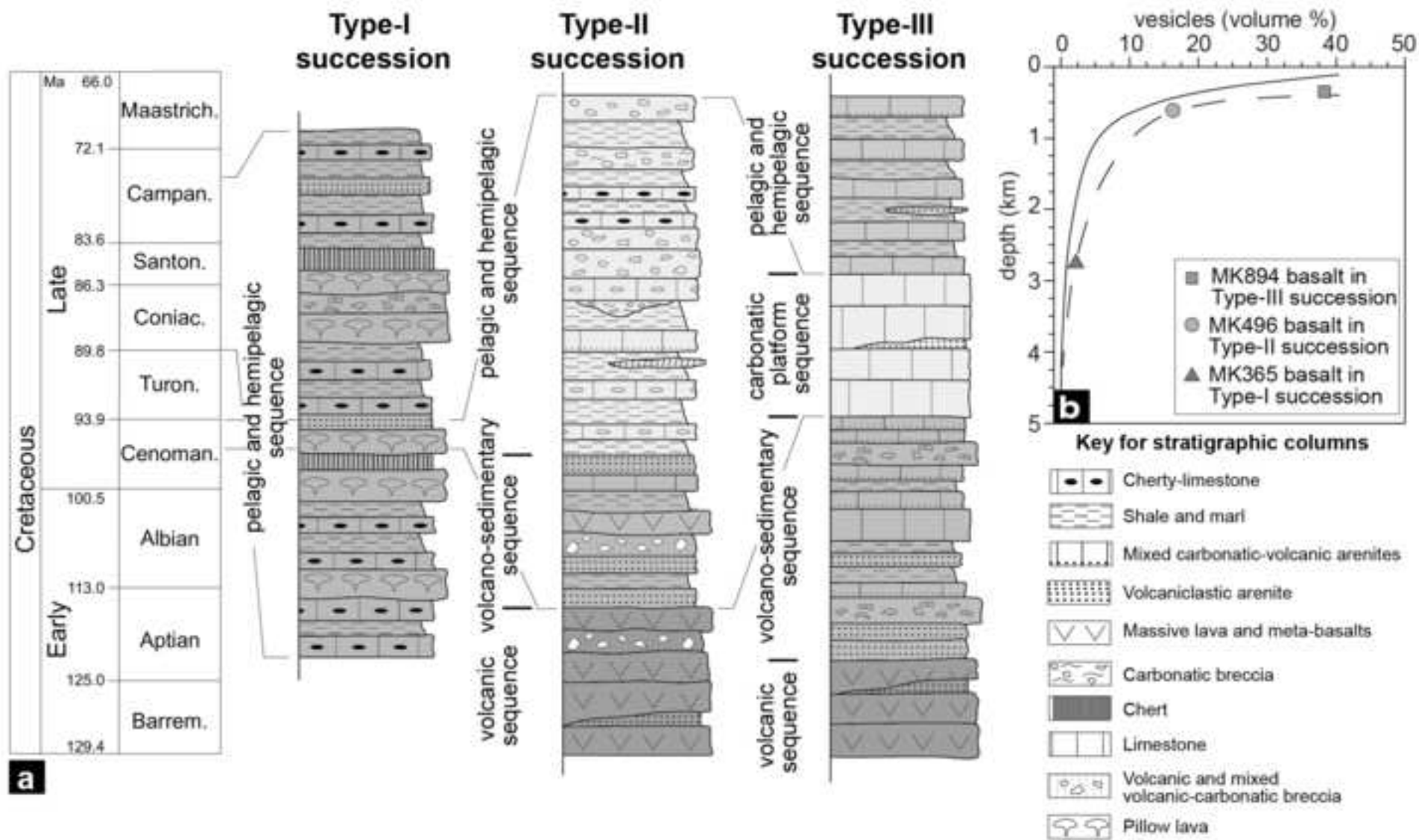


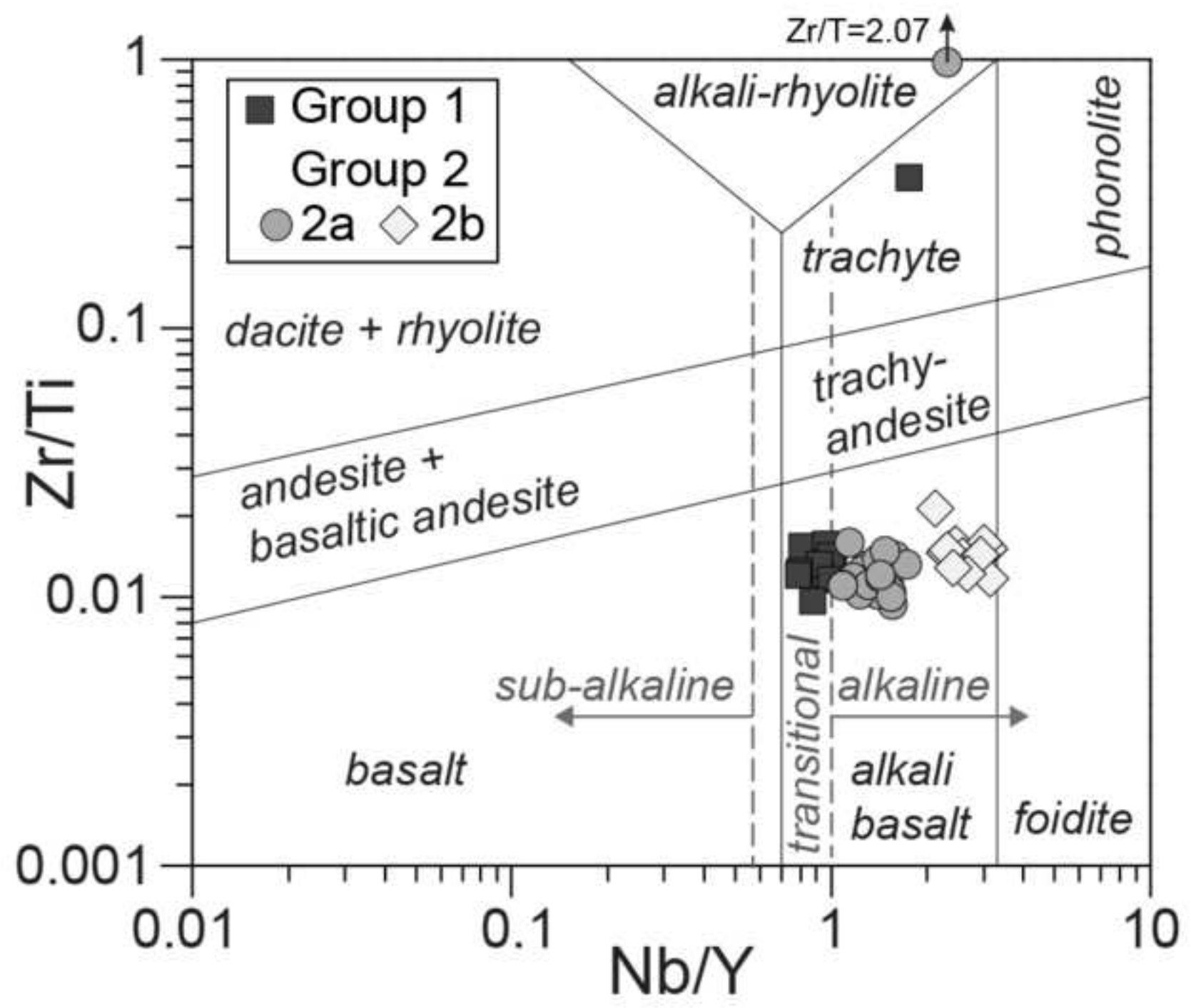


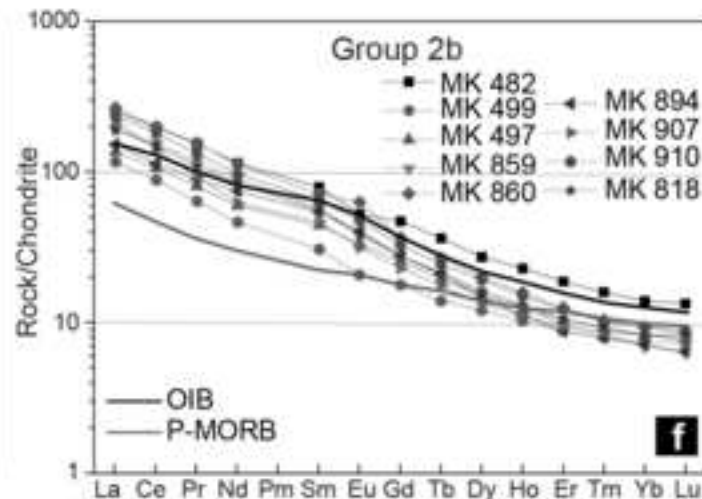
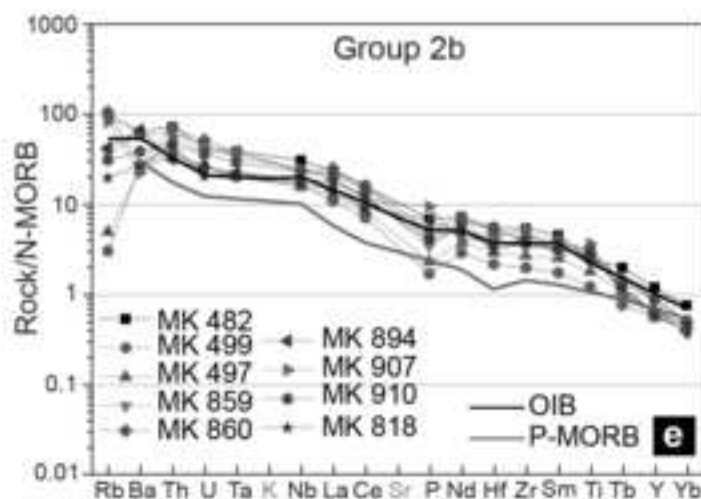
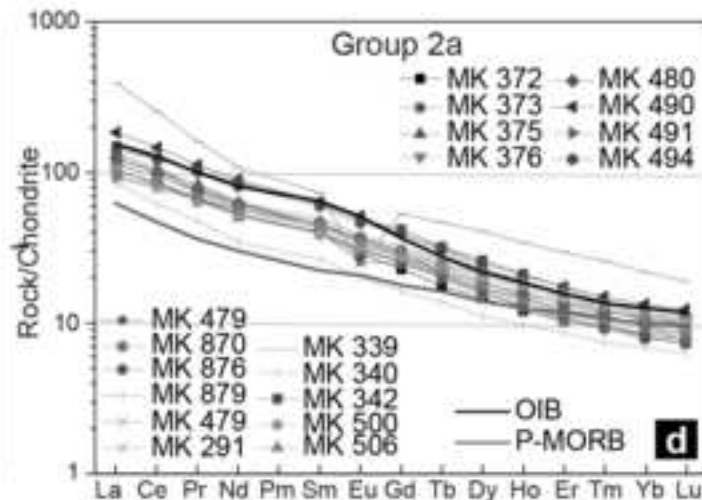
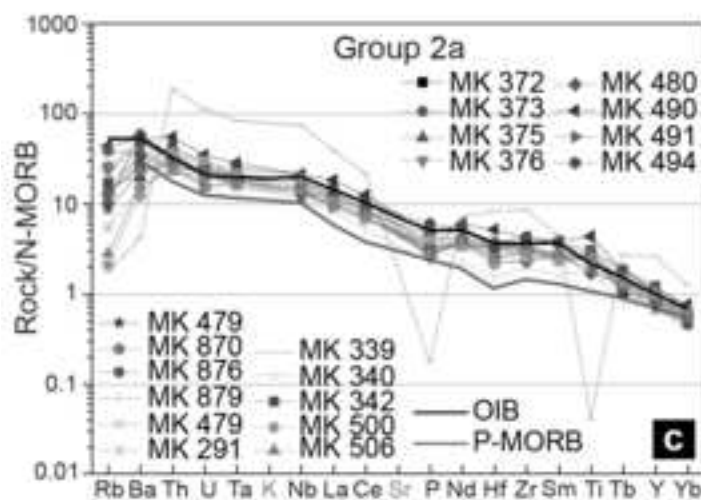
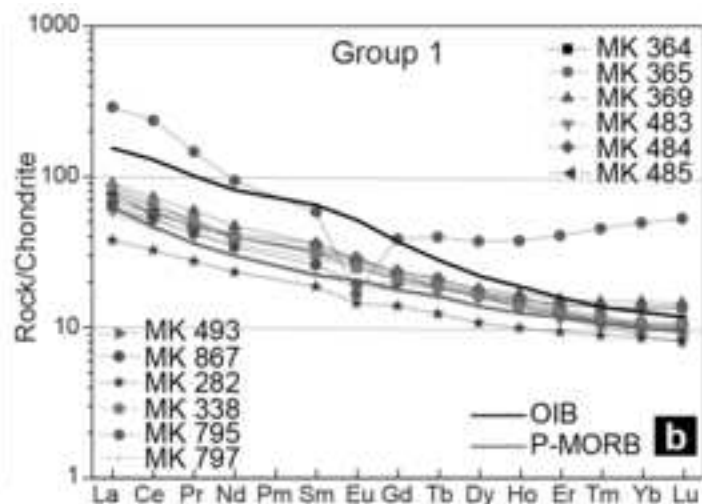
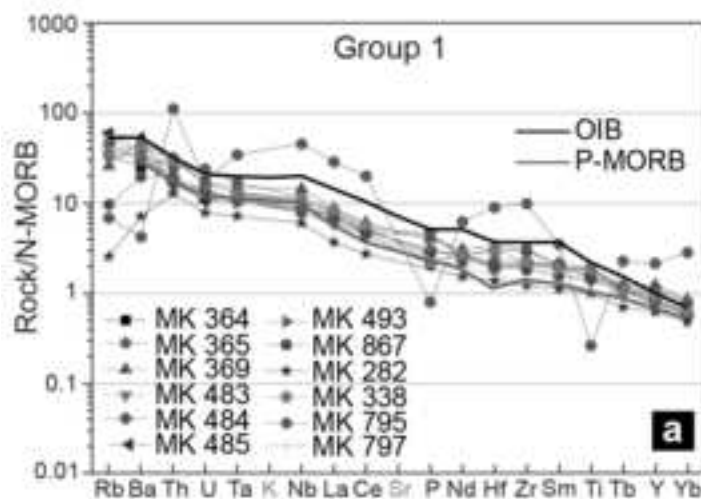


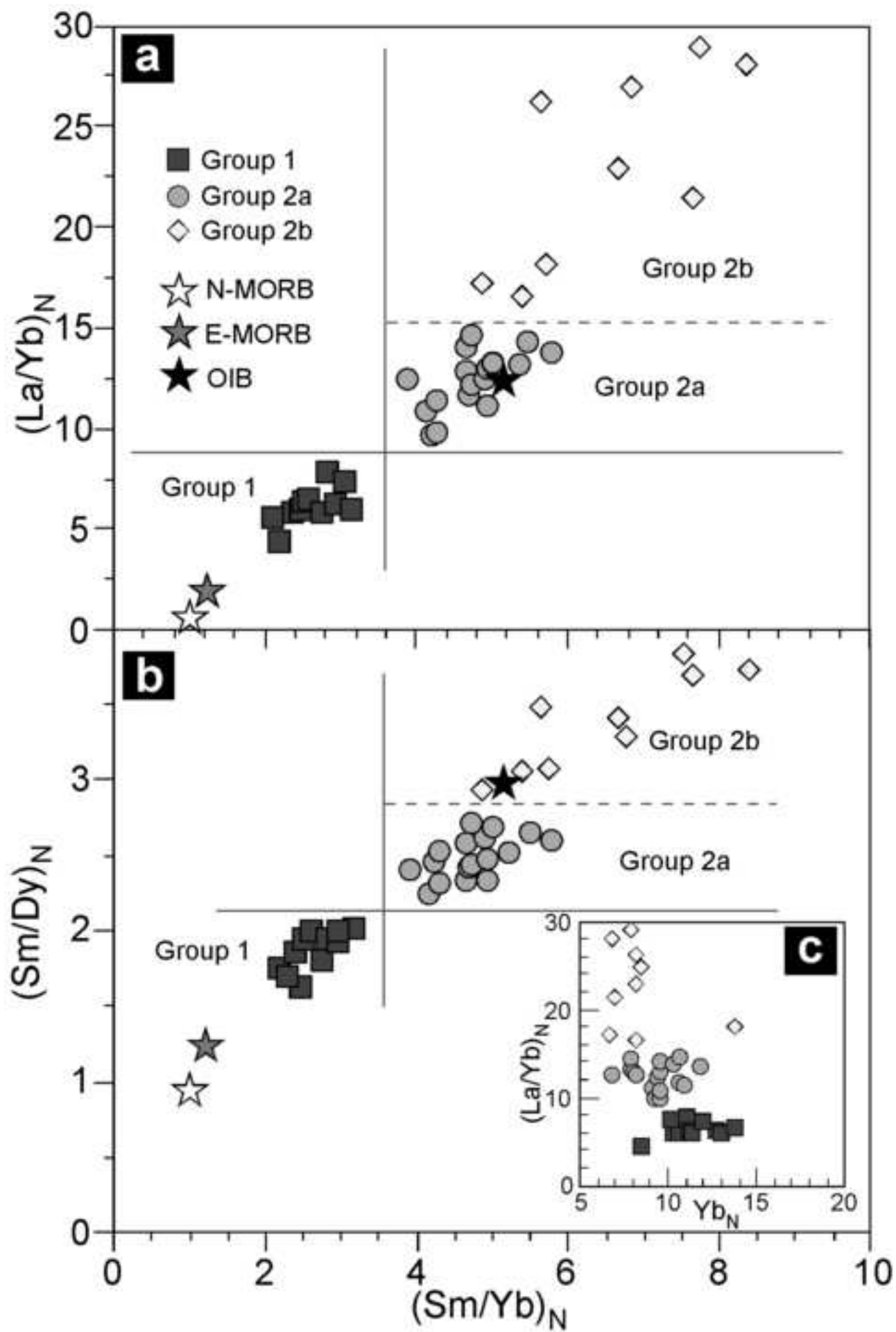


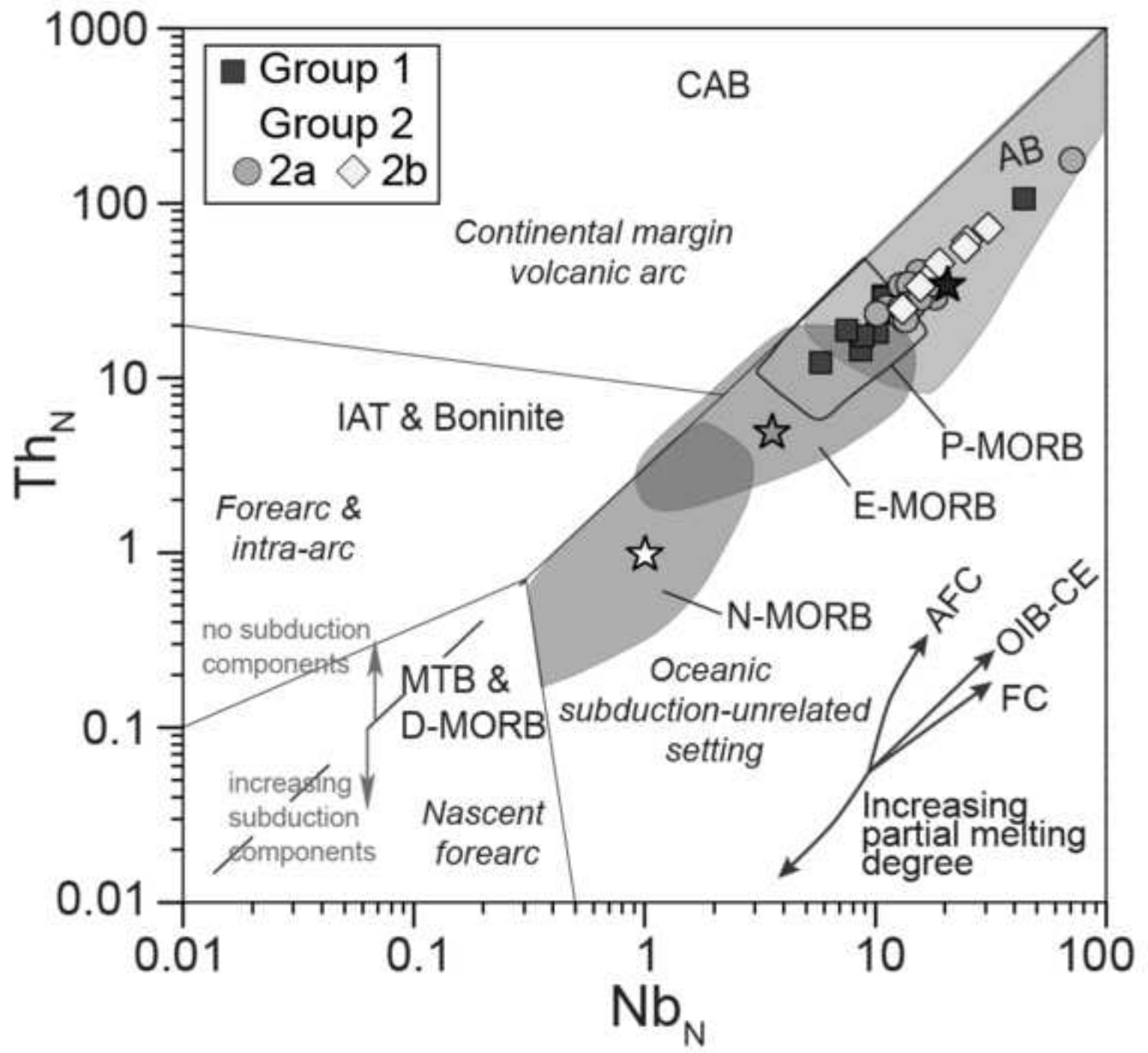


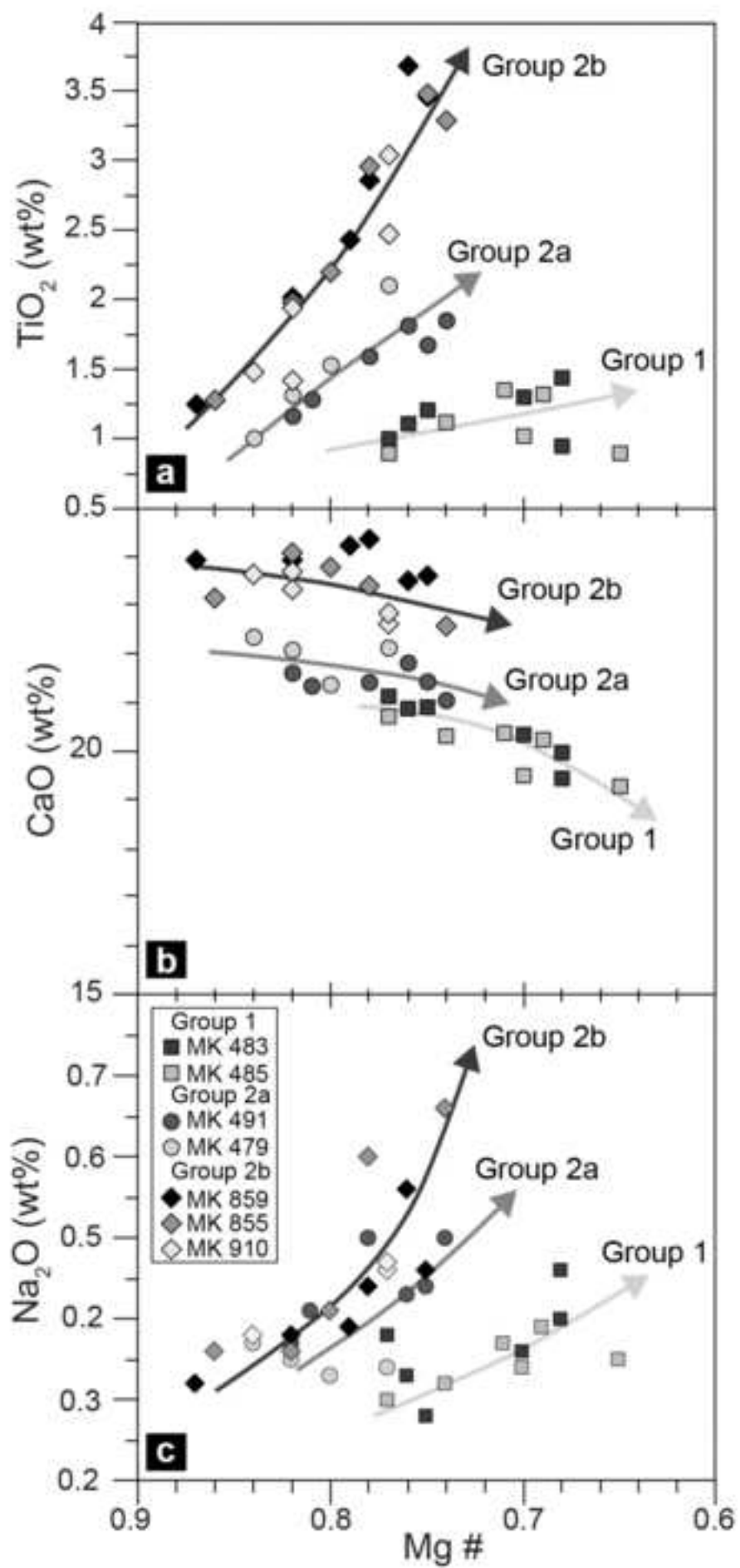


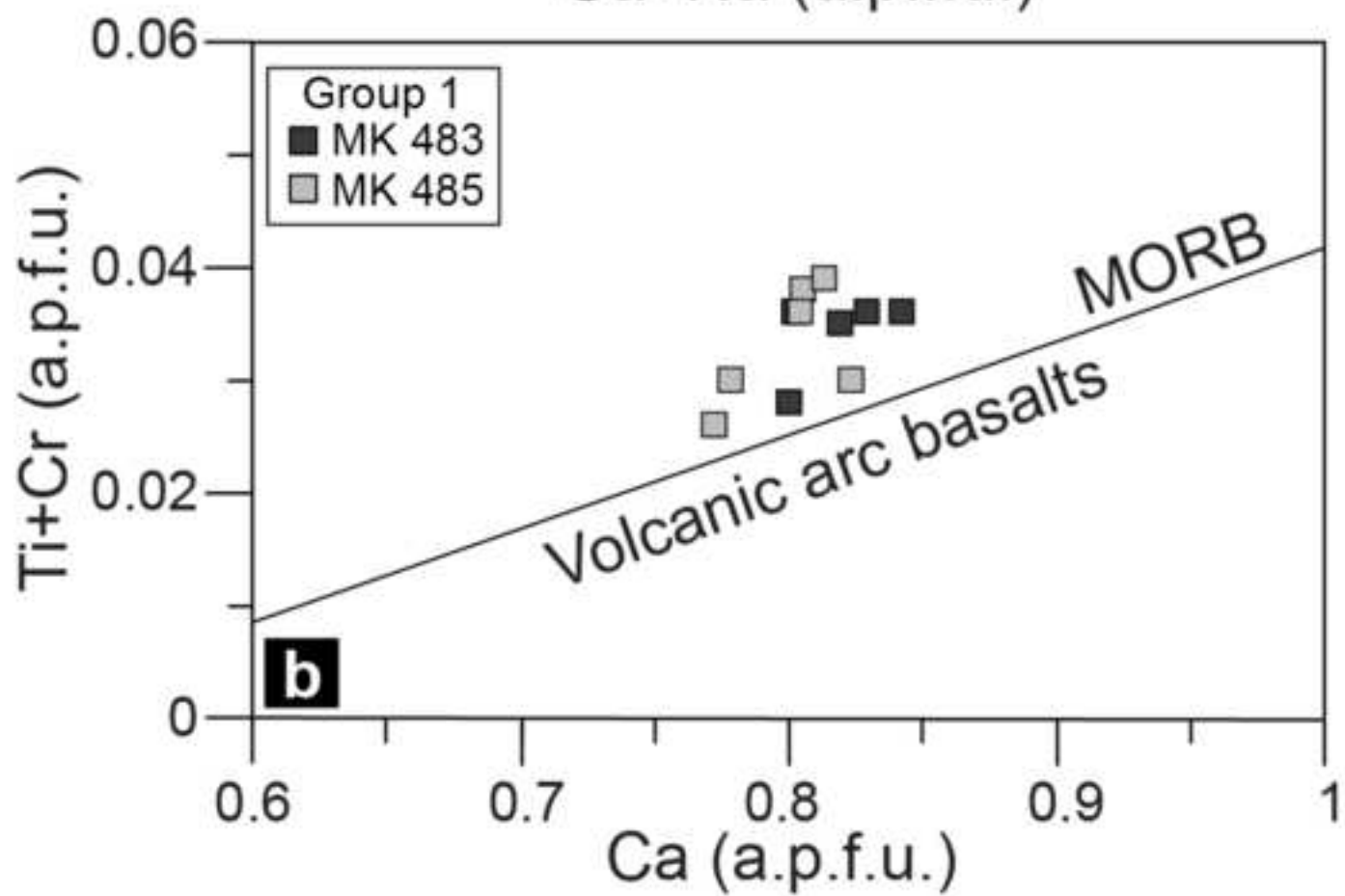
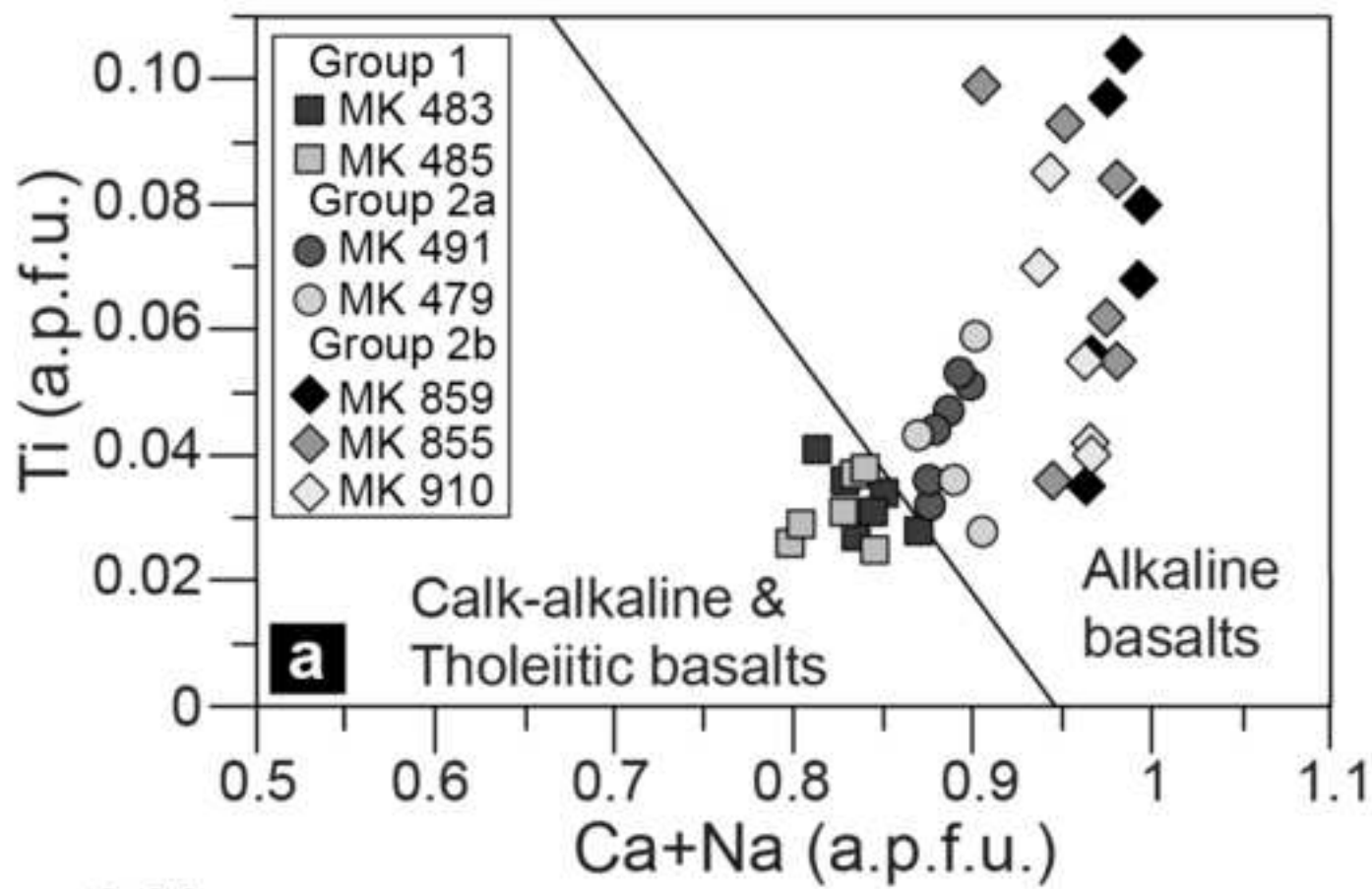


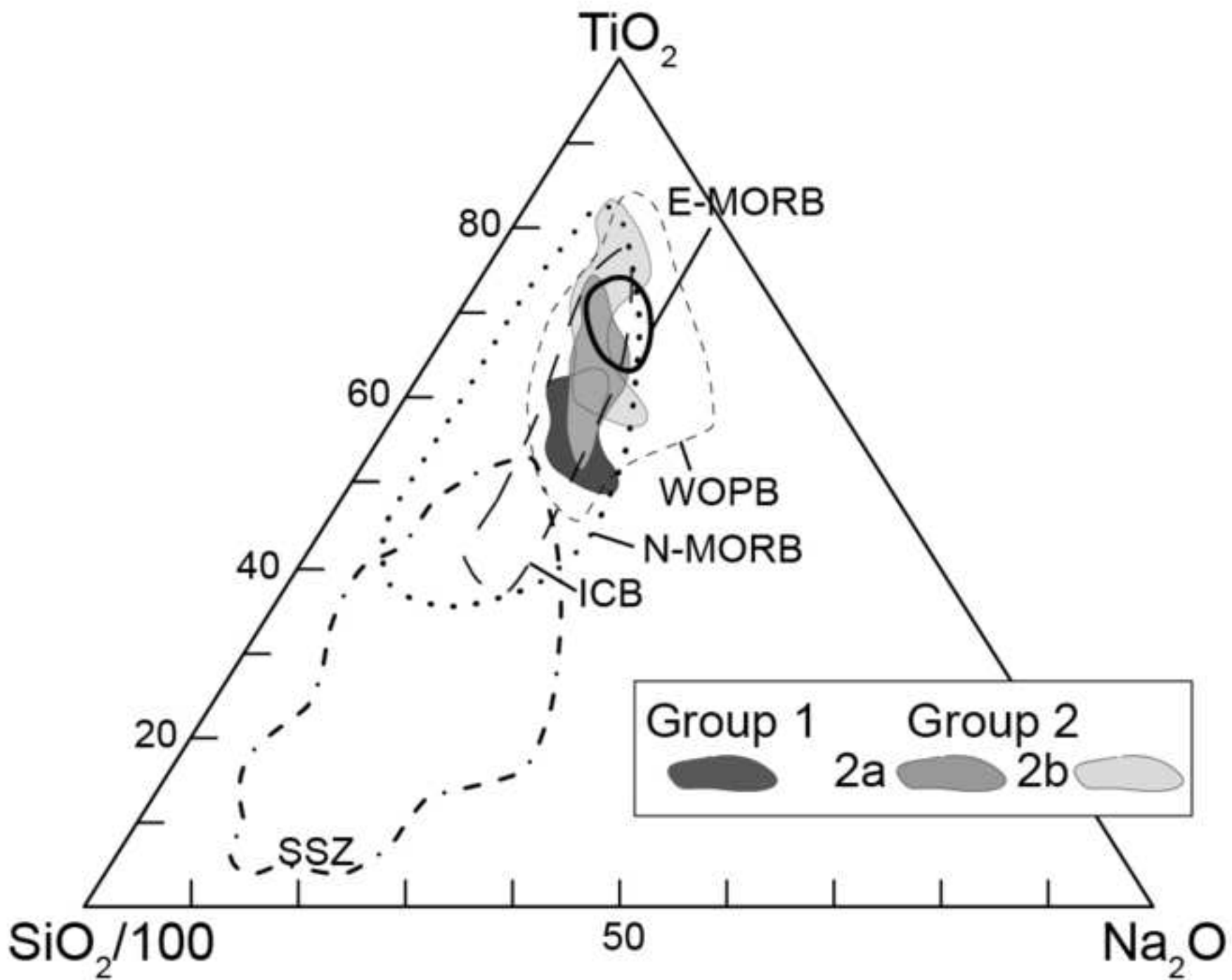


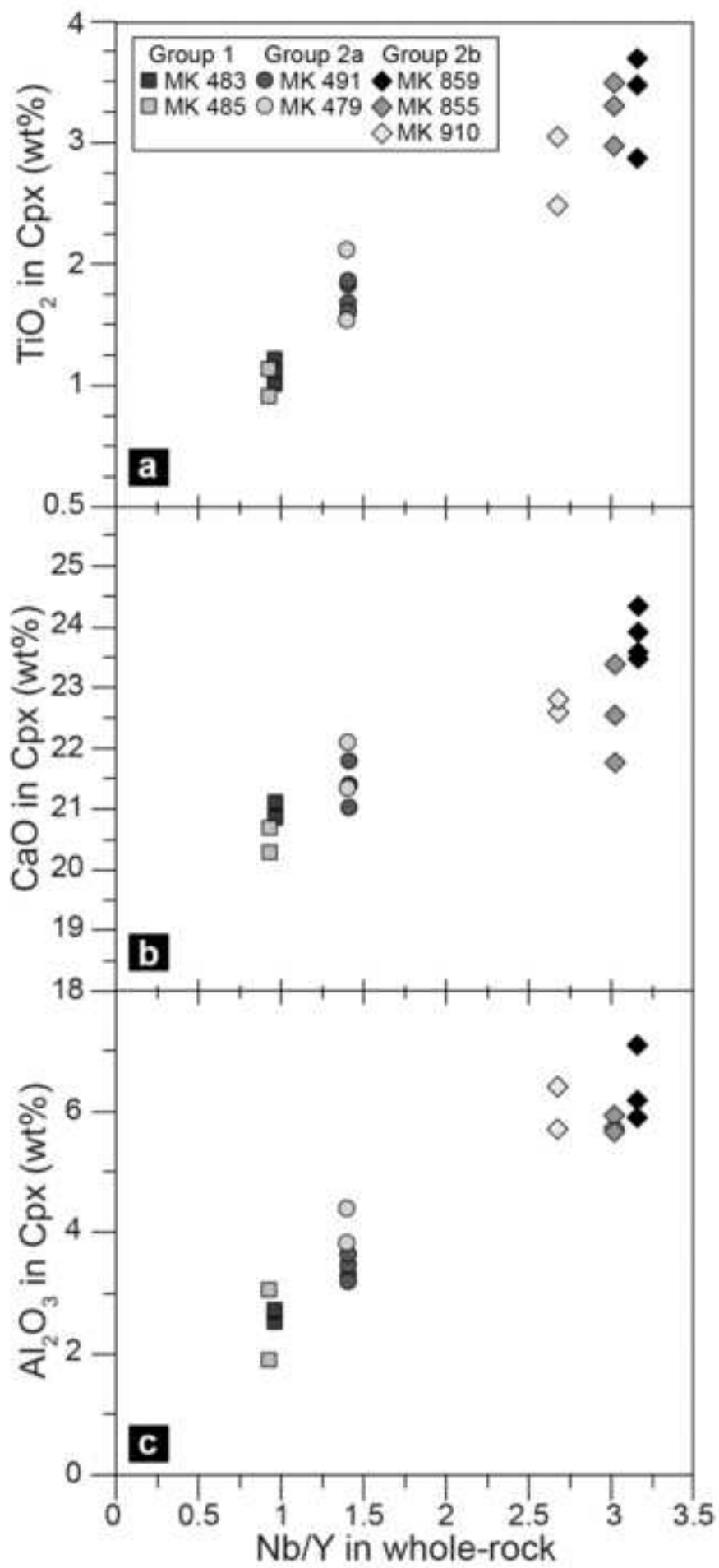


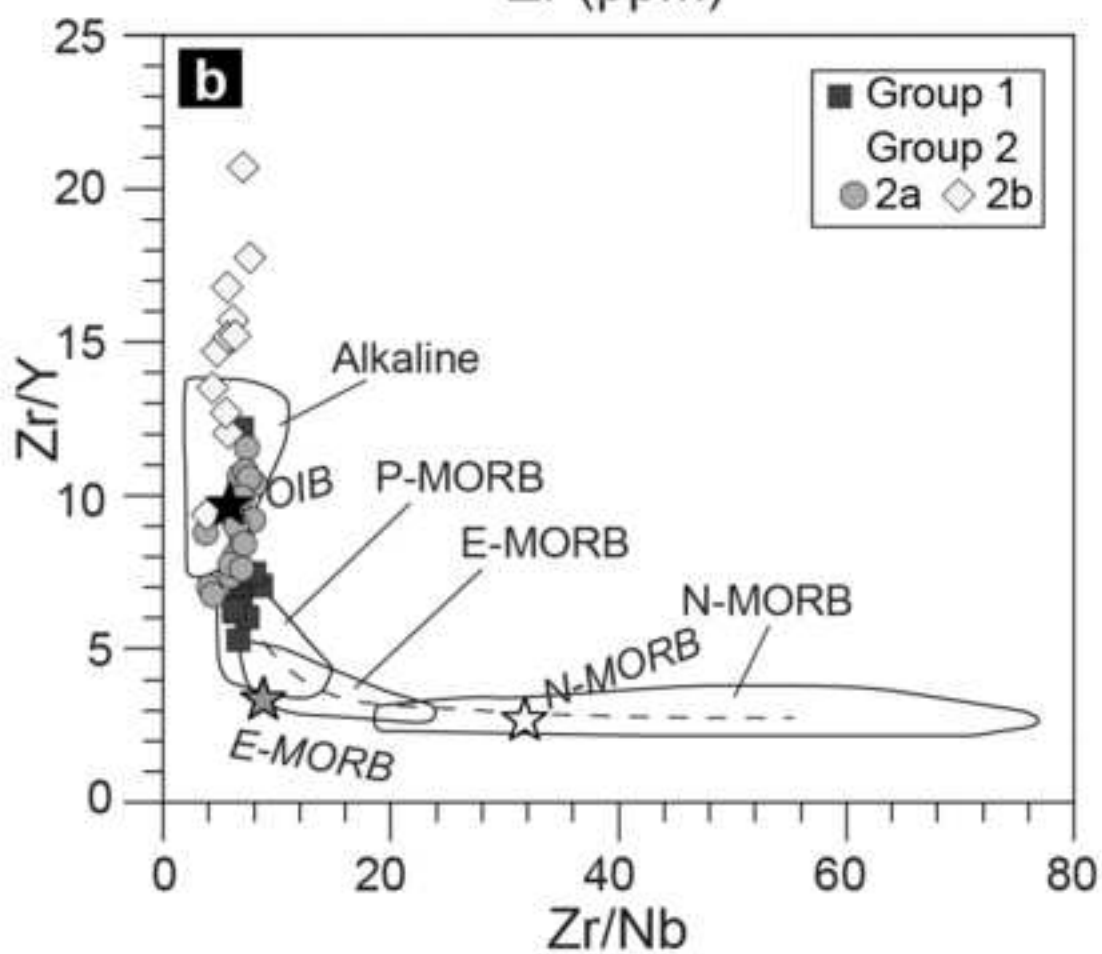
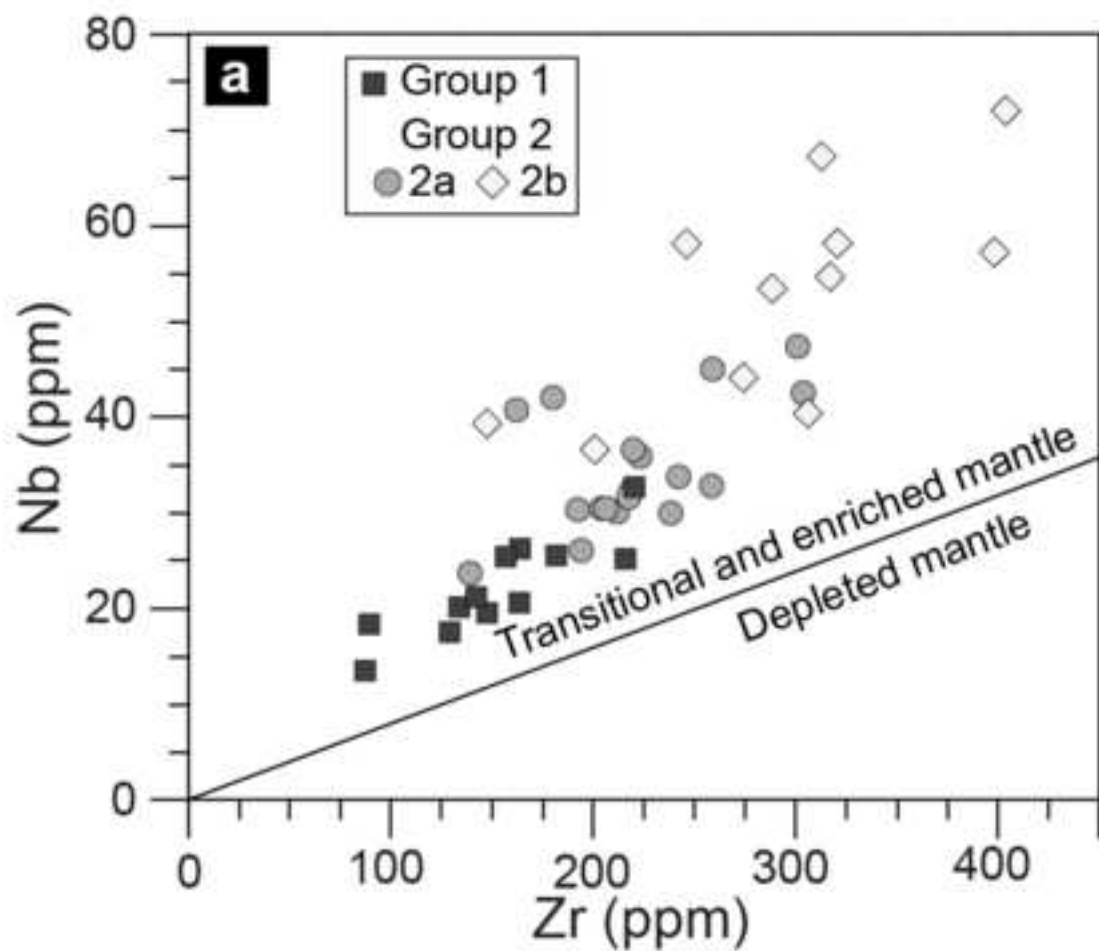


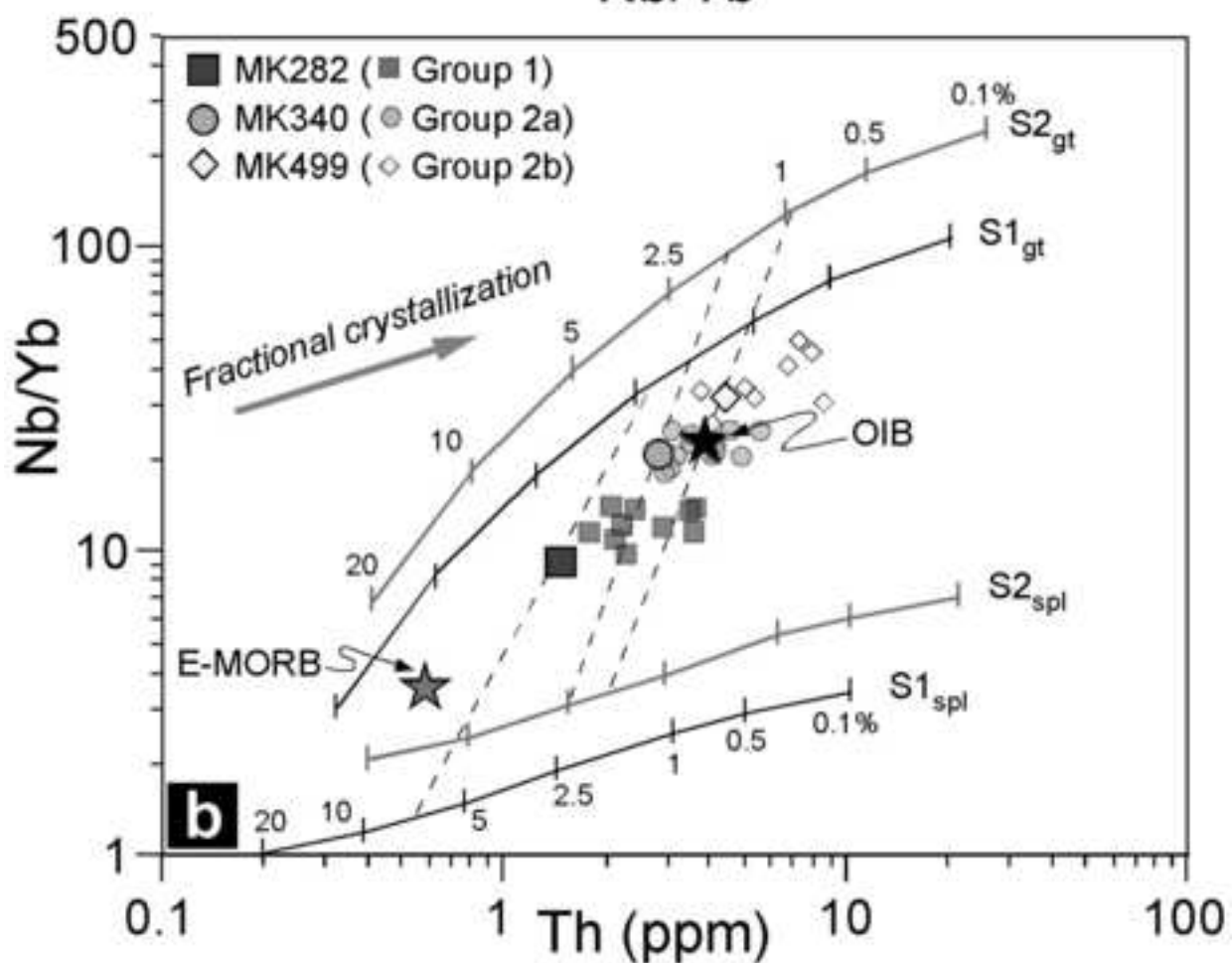
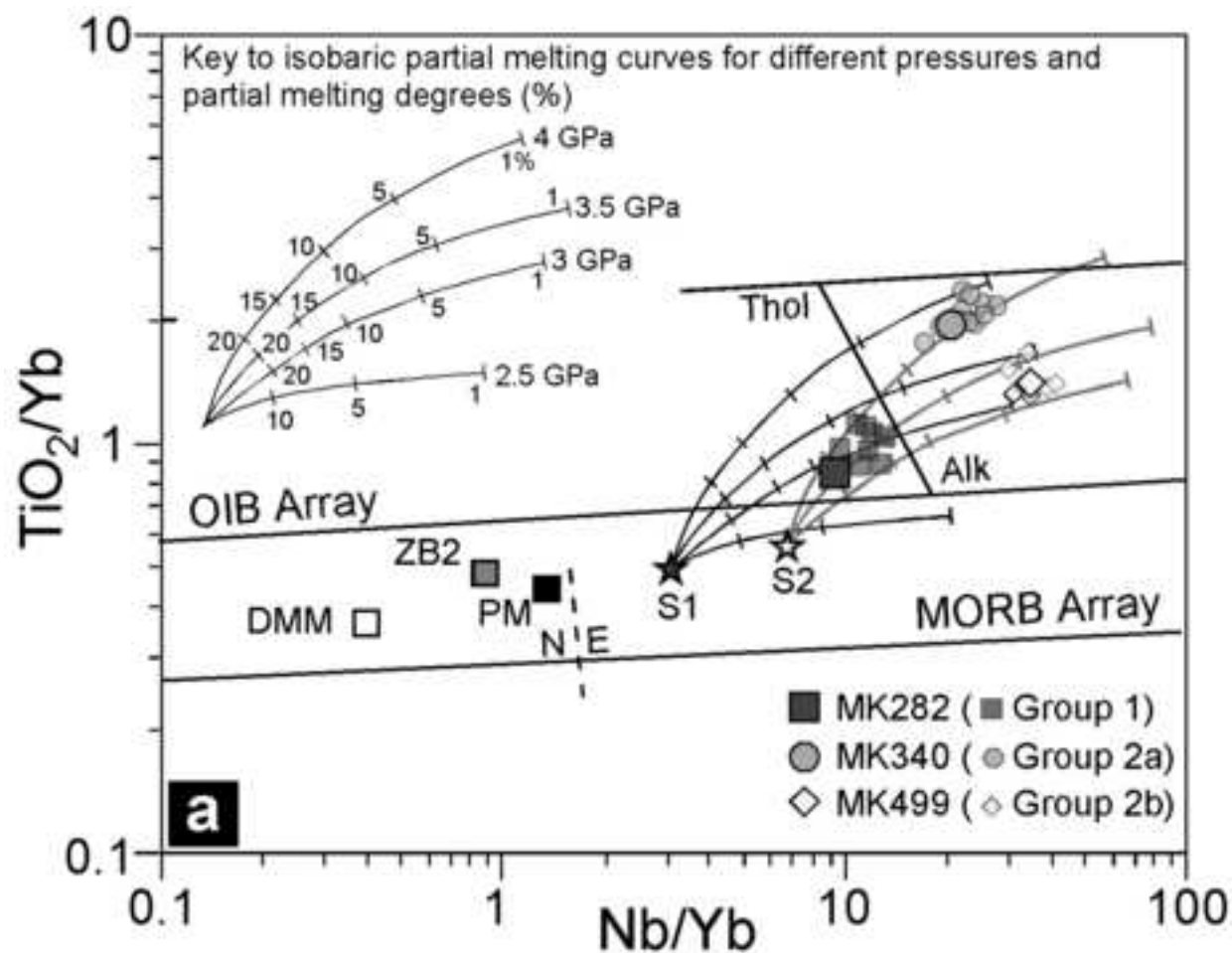


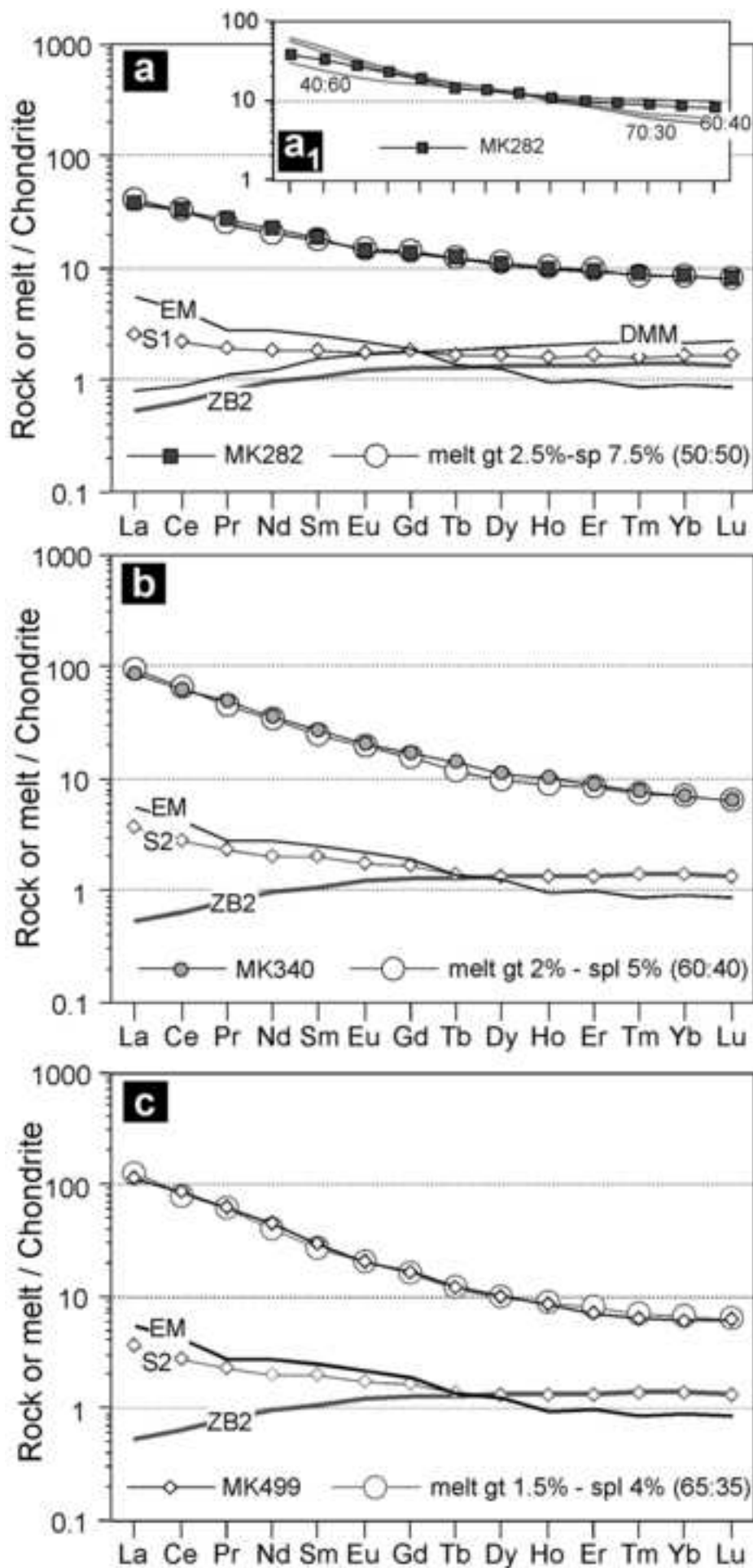












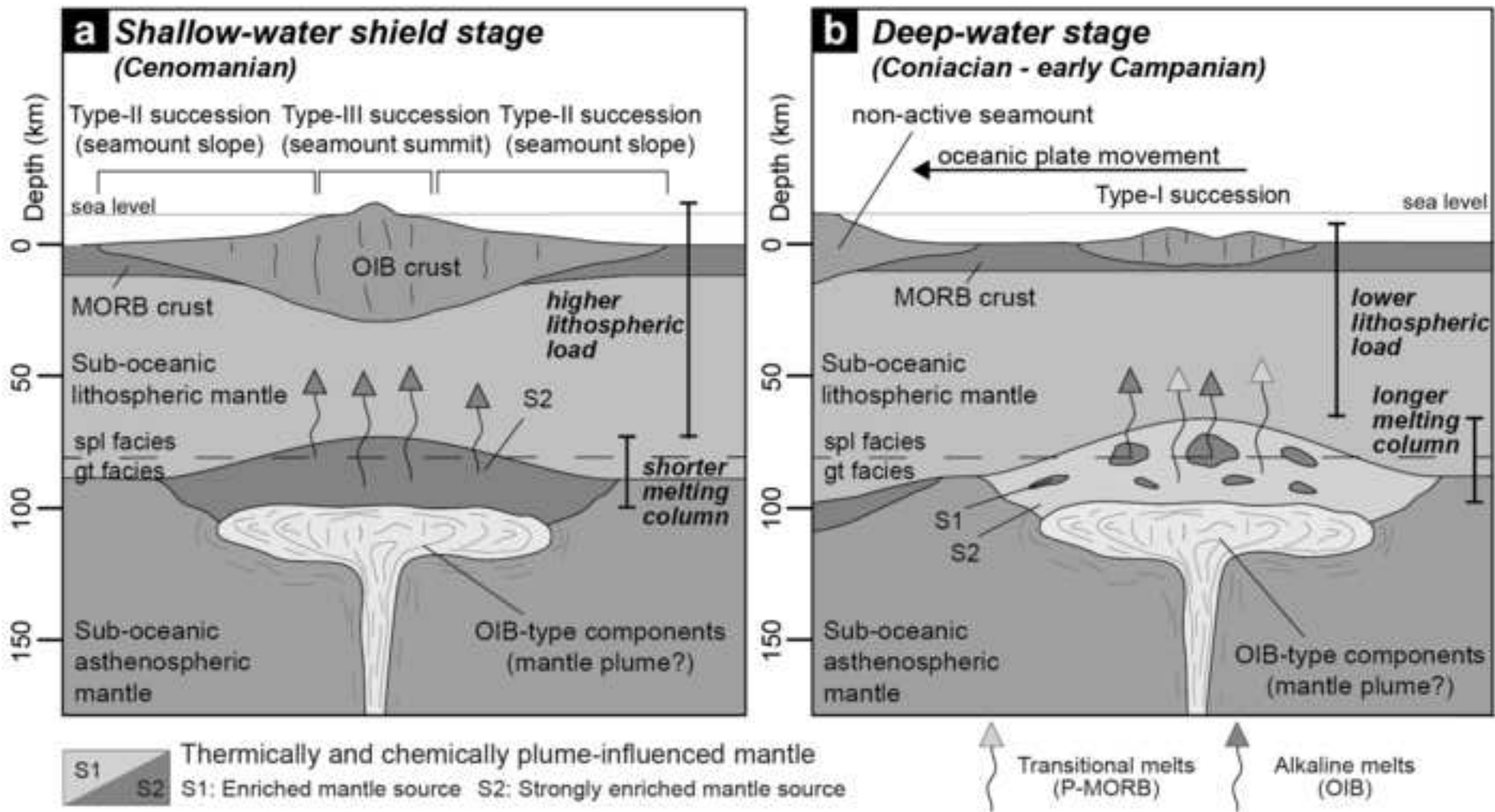


Table 1 (1/4)

Table 1 (1/4)												Table 1 (2/4)	
Rock Group	Group 1 (P-MORB)											Rock Group	Group 1 (
Sample	MK364	MK365*	MK369	MK370*	MK483	MK484	MK485	MK493*	MK867	MK282	MK338	Sample	MK795
Rock	bas and	bas	bas	bas	bas	Fe-bas	bas	bas	bas	meta-bas	Fe-bas	Rock	tra
Texture	aphiric	aphiric	aphiric	aphiric	doleritic	doleritic	doleritic	doleritic	aphiric	foliated	foliated	Texture	aphiric
Succession type	Type-I	Type-I	Type-I	Type-I	Type-II	Type-II	Type-II	Type-II	Type-II	Type-I	Type-II	Succession type	Type-I
<i>XRF analyses:</i>													
SiO ₂	53.3	51.4	43.3	51.8	47.2	44.6	47.2	47.6	49.5	52.3	50.9	SiO ₂	66.9
TiO ₂	2.29	2.27	2.19	2.27	1.64	1.68	1.90	2.01	1.69	1.20	2.24	TiO ₂	0.32
Al ₂ O ₃	16.5	14.8	15.9	16.4	15.6	16.3	17.2	16.7	14.9	12.2	13.3	Al ₂ O ₃	14.7
Fe ₂ O ₃	1.17	1.24	1.36	1.27	1.57	1.68	1.55	1.46	1.57	1.04	1.70	Fe ₂ O ₃	0.75
FeO	7.82	8.28	9.06	8.44	10.46	11.19	10.33	9.75	10.47	6.93	11.30	FeO	5.02
MnO	0.05	0.09	0.21	0.17	0.16	0.17	0.15	0.16	0.16	0.15	0.17	MnO	0.05
MgO	4.93	5.11	10.53	5.03	7.00	8.34	5.30	5.50	9.89	11.90	6.87	MgO	0.02
CaO	4.19	6.70	6.77	5.21	8.67	7.77	8.27	9.04	4.38	9.53	7.17	CaO	1.39
Na ₂ O	5.32	5.78	2.20	4.05	3.04	2.71	3.21	2.70	3.88	2.28	3.65	Na ₂ O	9.74
K ₂ O	0.97	0.81	1.28	1.40	1.59	1.11	1.54	1.28	0.18	0.09	0.97	K ₂ O	0.06
P ₂ O ₅	0.51	0.47	0.43	0.43	0.28	0.31	0.32	0.34	0.23	0.25	0.25	P ₂ O ₅	0.09
LOI	2.54	2.69	6.57	3.43	2.99	3.6	2.99	3.03	2.92	2.31	1.67	LOI	0.57
Total	99.53	99.66	99.86	99.94	100.18	99.48	100.04	99.56	99.75	99.92	100.17	Total	99.62
Mg#	52.9	52.4	67.4	51.5	54.4	57.0	47.8	50.1	62.7	75.4	52.0	Mg#	0.7
Zn	202	170	120	118	102	114	107	106	104	60	112	Zn	133
Cu	72	59	60	75	123	125	125	125	113	75	105	Cu	3
Sc	29	26	35	30	26	25	21	24	34	34	45	Sc	n.d.
Ga	17	17	22	19	20	19	23	21	16	12	19	Ga	37
Ni	56	47	214	101	66	55	30	32	84	108	28	Ni	n.d.
Co	57	60.5	71	53	45	42	38	42	57	31	45	Co	n.d.
Cr	160	143	353	259	153	112	58	51	378	456	79	Cr	3
V	239	230	244	273	244	245	236	227	227	247	292	V	21
Ba	155	219	290	186	231	184	323	227	120	44	261	Ba	26
Pb	12	8	6	7	8	9	8	9	18	10	10	Pb	26
<i>ICP-MS analyses:</i>													
Rb	18.5	18.6	14.0	27	31.7	24.4	32.0	27.1	5.21	1.39	19.9	Rb	3.72
Sr	817	669	417	419	258	492	500	499	105	329	278	Sr	80.5
Y	30.9	26.9	33.5	25	20.8	23.8	21.9	22.2	21.9	17.0	25.4	Y	58.0
Zr	216	164	220	182	134	149	148	164	130	88.0	157	Zr	701
La	19.1	18.2	21.4	20	14.2	16.2	19.5	16.6	15.1	8.95	20.5	La	68.9
Ce	38.7	34.5	44.4	48	31.6	35.8	18.1	34.3	32.4	19.8	41.3	Ce	146
Pr	4.84	4.48	5.63		4.03	4.65	35.5	4.52	3.98	2.60	4.90	Pr	13.9
Nd	18.6	18.2	21.9	21	16.7	19.5	4.41	18.5	15.9	10.8	18.8	Nd	44.0
Sm	4.84	4.74	5.48		4.33	5.48	18.3	5.03	3.97	2.85	4.76	Sm	8.91
Eu	1.43	1.46	1.61		1.49	1.67	4.86	1.68	1.12	0.834	1.46	Eu	0.97
Gd	4.41	4.52	4.86		4.37	4.81	1.59	4.81	4.05	2.83	4.31	Gd	7.96
Tb	0.695	0.738	0.778		0.703	0.792	4.63	0.766	0.671	0.458	0.681	Tb	1.49
Dy	4.13	4.25	4.57		3.97	4.50	0.701	4.32	4.06	2.71	4.06	Dy	9.45
Ho	0.854	0.870	0.941		0.771	0.866	4.10	0.827	0.812	0.556	0.785	Ho	2.13
Er	2.32	2.36	2.55		1.98	2.19	0.760	2.06	2.11	1.54	2.05	Er	6.71
Tm	0.333	0.342	0.366		0.281	0.303	2.02	0.305	0.288	0.224	0.289	Tm	1.16
Yb	2.16	2.22	2.35		1.75	1.93	0.278	1.90	1.79	1.44	1.87	Yb	8.39
Lu	0.319	0.317	0.345		0.257	0.279	1.76	0.273	0.258	0.204	0.274	Lu	1.33
Nb	25.1	26.2	32.6	25	20.1	23.8	0.246	20.6	17.5	13.5	25.4	Nb	103
Hf	5.93	3.93	6.68	4	4.29	3.68	4.27	4.72	3.97	2.74	6.12	Hf	17.9
Ta	1.67	1.98	1.92		1.42	1.53	1.34	1.29	1.37	0.916	1.62	Ta	4.41
Th	3.58	3.60	3.66	3	1.97	2.21	1.96	2.12	2.28	1.49	3.48	Th	12.8
U	0.748	1.08	0.783		0.641	0.489	0.479	0.593	0.613	0.356	0.764	U	0.809
Nb/Y	0.81	0.98	0.97	1.00	0.97	1.00	0.89	0.93	0.80	0.80	1.00	Nb/Y	1.77
Zr/Y	6.98	6.11	6.57	7.34	6.46	6.26	6.75	7.39	5.93	5.19	6.20	Zr/Y	12.10
Ti/V	59	61	58	52	42	43	50	55	46	30	47	Ti/V	95
(La/Sm) _N	2.55	2.48	2.52		2.12	1.91	2.40	2.12	2.45	2.03	2.78	(La/Sm) _N	4.99
(Sm/Yb) _N	2.49	2.37	2.59		2.75	3.16	3.06	2.94	2.46	2.19	2.83	(Sm/Yb) _N	1.18
(La/Yb) _N	6.35	5.90	6.53		5.83	6.03	7.36	6.25	6.04	4.44	7.86	(La/Yb) _N	5.89
(Sm/Dy) _N	1.95	1.85	1.99		1.81	2.02	1.97	1.93	1.62	1.75	1.95	(Sm/Dy) _N	1.57

P-MORB)	Group 2a (Alkaline)							
	MK372 bas aphiric Type-I	MK373* bas aphiric Type-I	MK375 Fe-bas aphiric Type-I	MK376 Fe-bas aphiric Type-I	MK490 Fe-bas doleritic Type-II	MK870 Fe-bas porphyritic Type-II	MK876 Fe-bas porphyritic Type-II	MK879 Fe-bas doleritic Type-II
51.1	47.6	48.2	46.3	46.2	45.1	46.5	45.6	47.9
1.23	2.96	2.72	3.09	3.00	5.13	2.60	3.21	2.65
13.9	14.2	14.3	14.5	15.0	13.9	12.6	15.9	13.2
1.12	1.51	1.39	1.71	1.58	2.02	1.72	1.70	1.68
7.48	10.04	9.30	11.43	10.54	13.44	11.47	11.33	11.22
0.20	0.19	0.13	0.13	0.15	0.14	0.14	0.15	0.13
9.07	5.89	6.35	5.31	6.84	6.12	8.54	10.59	8.57
9.20	10.45	8.47	9.82	8.20	8.27	8.60	3.24	7.92
3.05	3.09	3.55	2.42	2.56	1.83	2.10	2.04	2.30
1.08	0.65	0.38	0.56	1.34	0.89	0.24	1.54	0.94
0.24	0.33	0.35	0.35	0.33	0.51	0.48	0.48	0.42
1.98	2.80	4.27	4.10	3.88	2.04	4.91	4.13	3.05
99.66	99.65	99.45	99.69	99.60	99.39	99.87	99.96	99.98
68.4	51.1	54.9	45.3	53.6	44.8	57.0	62.5	57.7
52	97	105	113	119	148	79	113	54
74	38	93	59	112	158	65	24	9
31	24	23	31	32	34	29	23	27
14	20	16	27	23	25	23	24	24
95	82	51	76	91	99	45	21	39
23	48	42	40	52	55	49	54	44
301	110	92	93	101	46	25	29	26
257	302	268	357	348	518	284	291	297
203	122	161	156	255	315	134	212	232
8	7	8	7	8	6	10	7	9
19.0	8.76	7.16	6.94	12.4	23.3	13.8	20.6	19.7
275	422	318	270	170	716	705	114	1016
20.8	23.1	21.2	27.9	24.0	30.5	28.4	23.9	23.9
89.8	238	242	223	219	301	259	220	204
18.3	24.7	26.6	31.6	24.2	47.3	27.3	28.9	29.3
13.3	51.0	58.0	64.1	50.9	43.6	57	61.3	61.6
27.4	6.35	6.92	7.83	6.56	89.4	7.17	7.31	7.95
3.51	23.9	26.2	29.0	24.8	10.6	27.4	28.1	29.7
13.8	6.00	6.58	6.78	6.12	41.7	6.82	6.76	7.60
3.50	1.69	1.75	1.95	1.77	9.73	2.14	2.14	2.22
1.07	4.68	5.37	5.69	5.16	2.96	5.95	6.24	6.60
3.59	0.658	0.785	0.820	0.738	7.96	0.841	0.903	0.981
0.583	3.70	4.11	4.35	3.89	1.17	4.63	4.80	5.20
3.50	0.679	0.720	0.814	0.720	6.35	0.852	0.905	0.964
0.706	1.69	1.73	2.00	1.73	1.16	2.01	2.17	2.30
1.94	0.226	0.232	0.266	0.234	2.87	0.280	0.287	0.311
0.281	1.33	1.33	1.62	1.39	0.379	1.60	1.61	1.80
1.77	0.188	0.183	0.230	0.193	2.25	0.224	0.193	0.250
0.255	29.9	33.6	35.8	32.4	0.310	32.7	36.5	30.3
3.22	6.38	6.71	7.14	6.56	10.2	6.83	6.28	7.20
1.38	2.16	2.21	2.52	2.33	3.56	2.12	2.53	2.22
2.16	4.11	3.11	4.89	4.15	6.26	3.20	3.49	2.69
0.668	0.980	0.981	1.28	1.19	1.55	0.685	1.07	0.752
0.88	1.30	1.59	1.28	1.35	1.55	1.15	1.52	1.27
4.32	10.3	11.4	7.98	9.12	9.87	9.09	9.18	8.53
29	61	64	54	54	61	58	69	55
2.46	2.66	2.61	3.01	2.55	2.89	2.58	2.76	2.49
2.20	4.68	5.48	4.36	4.59	4.81	4.72	4.66	4.69
5.42	12.42	14.28	13.13	11.72	13.92	12.20	12.86	11.69
1.66	2.69	2.66	2.58	2.61	2.54	2.44	2.34	2.42

Table 1 (3/4)

Rock Group	Group 2a (Alkaline)											Rock Group	Sample Rock Texture Succession type	
	MK491* Fe-bas doleritic Type-II	MK480 bas doleritic Type-II	MK494 Fe-bas doleritic Type-II	MK479 bas aphiric Type-III	MK291 meta-Fe-bas foliated Type-II	MK339 meta-a-rhy foliated Type-II	MK340 meta-bas foliated Type-II	MK342 meta-Fe-bas foliated Type-II	MK500 Fe-bas aphiric Type-II	MK506 Fe-bas aphiric Type-II	MK507 bas aphiric Type-II			
<i>XRF analyses:</i>													<i>XRF analyses:</i>	
SiO ₂	44.3	52.8	46.9	51.7	46.4	66.8	41.9	45.4	42.0	46.4	45.7	SiO ₂	48.6	
TiO ₂	2.25	2.04	3.34	3.06	2.91	0.05	2.03	3.65	2.60	3.15	2.75	TiO ₂	3.06	
Al ₂ O ₃	14.3	14.5	13.7	13.9	14.5	15.2	13.4	13.3	14.1	13.6	14.8	Al ₂ O ₃	15.8	
Fe ₂ O ₃	1.74	1.15	1.80	1.42	1.73	0.57	1.38	2.23	1.66	1.80	1.56	Fe ₂ O ₃	1.43	
FeO	11.60	7.65	12.03	9.49	11.54	3.77	9.17	14.86	11.06	12.02	10.38	FeO	9.52	
MnO	0.14	0.12	0.13	0.14	0.19	0.04	0.13	0.21	0.18	0.16	0.18	MnO	0.13	
MgO	14.08	7.05	7.99	7.30	7.84	3.37	12.49	6.63	6.04	10.52	7.43	MgO	6.74	
CaO	5.75	8.08	7.38	5.61	8.31	0.24	6.68	7.78	9.75	5.69	8.47	CaO	5.15	
Na ₂ O	1.67	5.31	2.28	2.93	3.24	8.76	1.67	2.14	2.57	2.55	2.90	Na ₂ O	2.05	
K ₂ O	0.44	0.38	1.03	0.29	0.02	0.10	0.66	0.22	n.d.	0.03	0.03	K ₂ O	3.08	
P ₂ O ₅	0.30	0.28	0.66	0.35	0.32	0.02	0.23	0.38	0.40	0.30	0.30	P ₂ O ₅	0.78	
LOI	3.13	1.30	2.37	3.51	2.96	1.18	9.97	2.76	9.13	3.47	5.21	LOI	3.05	
Total	99.76	100.61	99.56	99.71	99.92	100.07	99.70	99.51	99.55	99.70	99.68	Total	99.44	
Mg#	68.4	62.2	54.2	57.8	54.8	61.4	70.8	44.3	49.3	60.9	56.1	Mg#	55.8	
Zn	122	39	137	126	141	208	86	167	110	110	119	Zn	113	
Cu	116	56	91	44	110	5	147	121	71	93	101	Cu	61	
Sc	27	22	23	27	33	n.d.	47	42	24	33	23	Sc	19	
Ga	18	12	22	15	24	33	17	24	20	19	19	Ga	27	
Ni	356	26	46	70	48	n.d.	97	36	59	38	45	Ni	71	
Co	67	30	55	32	35	n.d.	51	50	53	36	39	Co	33	
Cr	412	237	19	193	94	40	152	54	65	38	94	Cr	68	
V	294	265	310	267	315	42	312	376	318	325	277	V	290	
Ba	204	351	293	135	91	26	202	198	74	95	90	Ba	395	
Pb	9	10	7	7	8	5	9	8	9	9	10	Pb	8	
<i>ICP-MS analyses:</i>													<i>(XRF) ICP-MS analyses:</i>	
Rb	7.00	5.46	13.8	4.69	2.92	0.955	14.3	9.19	1.13	1.51	2	Rb	55.8	
Sr	826	405	866	106	612	17.3	171	610	1010	595	588	Sr	581	
Y	21.5	23.4	28.4	18.5	25.5	69.9	19.1	33.0	27.0	26.9	21	Y	33.8	
Zr	192	162	303	194	212	609	139	259	180	218	206	Zr	403	
La	22.1	29.3	33.7	24.7	21.7	93.2	20.2	44.9	24.9	24.0	18	La	59.2	
Ce	49.5	62.2	74.7	51.3	47.9	155	37.4	35.4	49.9	53.0	51	Ce	119	
Pr	6.16	7.32	9.60	6.40	6.13	15.3	4.50	75.3	6.08	6.41		Pr	14.5	
Nd	24.7	29.3	37.7	24.4	24.0	50.3	16.1	9.67	24.4	26.2	20	Nd	53.0	
Sm	6.17	7.13	9.13	6.10	6.10	11.2	4.06	39.7	5.91	6.85		Sm	12.0	
Eu	1.75	2.06	2.68	1.48	1.78	1.40	1.16	9.44	1.86	2.00		Eu	3.02	
Gd	5.18	5.78	8.02	5.08	5.39	11.0	3.33	2.83	5.30	5.71		Gd	9.60	
Tb	0.775	0.841	1.15	0.746	0.803	1.74	0.512	8.62	0.814	0.863		Tb	1.35	
Dy	4.18	4.68	5.84	4.10	4.38	10.3	2.80	1.20	4.51	4.88		Dy	6.85	
Ho	0.815	0.874	1.06	0.728	0.782	1.93	0.546	6.63	0.853	0.908		Ho	1.28	
Er	2.00	2.22	2.46	1.81	1.90	4.88	1.41	1.20	2.13	2.28		Er	3.07	
Tm	0.278	0.299	0.309	0.241	0.258	0.654	0.188	2.85	0.277	0.283		Tm	0.402	
Yb	1.63	1.85	1.75	1.37	1.58	3.70	1.16	0.347	1.63	1.55		Yb	2.34	
Lu	0.225	0.257	0.249	0.188	0.210	0.477	0.158	1.98	0.230	0.229		Lu	0.336	
Nb	30.2	40.6	42.4	26.0	30.0	165	23.6	0.268	41.9	31.5	30	Nb	71.8	
Hf	5.09	4.45	7.29	6.12	5.45	16.2	3.00	6.28	4.18	4.72	7	Hf	11.4	
Ta	2.24	2.71	2.94	2.02	1.98	10.5	1.42	3.08	2.69	2.24		Ta	5.13	
Th	2.95	3.87	3.54	3.06	3.05	21.4	2.84	5.00	4.20	2.62	3	Th	8.74	
U	0.697	0.990	1.07	0.993	0.932	5.01	0.663	1.24	1.33	0.869		U	2.00	
Nb/Y	1.41	1.74	1.49	1.40	1.18	2.37	1.24	1.36	1.55	1.17	1.44	Nb/Y	2.13	
Zr/Y	8.94	6.95	10.7	10.5	8.33	8.71	7.31	7.83	6.69	7.53	9.83	Zr/Y	11.9	
Ti/V	48	46	67	71	57	7	43	60	54	61	63	Ti/V	66	
(La/Sm) _N	2.31	2.66	2.38	2.62	2.30	5.39	3.21	2.42	2.64	2.26		(La/Sm) _N	3.17	
(Sm/Yb) _N	4.21	4.28	5.79	4.95	4.28	3.35	3.89	5.30	4.14	4.92		(Sm/Yb) _N	5.72	
(La/Yb) _N	9.74	11.4	13.8	12.9	9.84	18.08	12.5	12.84	10.92	11.11		(La/Yb) _N	18.16	
(Sm/Dy) _N	2.45	2.53	2.60	2.47	2.31	1.80	2.40	2.37	2.24	2.33		(Sm/Dy) _N	3.07	


Group 2b (Alkaline)									
MK496*	MK497*	MK499	MK855*	MK859*	MK860	MK894*	MK907*	MK910	MK818
bas	bas	bas	bas	Fe-bas	Fe-bas	bas	bas	meta-bas	bas
porphyritic	porphyritic	porphyritic	porphyritic	porphyritic	porphyritic	aphiric	aphiric	foliated	aphiric
Type-II	Type-II	Type-II	Type-II	Type-II	Type-II	Type-III	Type-III	Type-III	Type-III
46.7	50.8	48.4	45.1	42.1	45.4	51.8	51.8	53.5	53.1
3.41	2.25	1.55	3.28	3.41	3.77	3.41	4.61	3.98	3.54
15.2	14.2	14.9	12.8	13.1	13.8	14.8	14.2	13.0	12.8
1.36	1.15	1.22	1.49	1.69	1.72	1.33	1.39	1.32	1.29
9.09	7.65	8.11	9.92	11.26	11.48	8.86	9.28	8.83	8.60
0.17	0.14	0.15	0.14	0.16	0.18	0.19	0.32	0.13	0.14
9.88	7.35	13.61	8.39	11.82	9.19	4.06	3.39	5.03	6.22
8.63	9.51	7.09	11.97	10.17	8.22	8.72	6.08	8.05	8.33
2.79	4.74	2.81	1.75	0.91	1.59	4.75	5.50	3.78	3.51
0.25	0.12	0.11	1.79	1.80	2.10	0.54	1.08	0.76	0.66
0.55	0.27	0.20	0.54	0.40	0.60	0.79	1.10	0.49	0.46
1.62	1.93	2.06	2.66	3.14	1.76	0.43	1.11	1.10	1.04
99.65	100.11	100.25	99.87	99.97	99.85	99.62	99.89	99.96	99.63
66.0	63.2	74.9	60.1	65.2	58.8	45.0	39.4	50.4	56.3
72	39	64	60	90	66	104	97	63	42
102	74	89	125	108	44	10	33	55	32
20	22	25	24	34	30	12	12	27	27
11	10	10	16	19	16	16	13	14	15
66	40	285	53	134	113	n.d.	33	28	15
40	37	49	48	63	45	27	37	37	14
85	246	959	42	280	270	5	4	97	56
336	303	228	406	373	408	190	424	311	267
610	153	170	267	370	172	421	142	244	173
7	10	8	7	9	9	12	10	11	12
(XRF)			(XRF)						
6	2.80	1.70	36	20.7	59.4	23.8	45.9	17.4	11.0
570	204	138	584	591	208	198	128	1458	1123
21	15.9	15.9	19	18.3	26.0	17.3	19.3	24.7	18.1
313	201	148	320	246	317	306	398	288	274
59	31.9	27.1	45.0	45.5	54.5	35.8	50.7	53.3	44.6
129	64.4	53.6	119	94.4	62.8	68.9	84.8	55.1	90.6
	7.58	6.18		11.0	121	8.41	8.72	110	10.3
31	27.5	22.0	39	41.8	14.7	34.3	28.8	12.6	39.2
	6.69	4.93		8.75	51.6	8.24	7.05	44.9	8.37
	1.92	1.29		2.26	10.9	2.33	1.81	9.83	2.19
	5.21	3.62		5.61	3.62	5.65	4.68	2.74	5.62
	0.722	0.516		0.765	7.46	0.774	0.651	6.63	0.796
	3.73	2.78		3.90	0.992	3.70	3.37	0.903	4.08
	0.681	0.546		0.711	5.07	0.624	0.620	4.81	0.733
	1.73	1.38		1.57	0.886	1.44	1.55	0.839	1.73
	0.230	0.184		0.212	2.05	0.200	0.218	2.00	0.235
	1.38	1.13		1.16	0.262	1.20	1.39	0.254	1.40
	0.193	0.168		0.159	1.55	0.161	0.200	1.58	0.208
67	36.5	39.2	58	57.9	0.215	40.3	57.1	0.225	44.0
8	6.00	4.48	8	8.66	10.1	7.33	8.71	11.5	6.50
	2.76	2.66		4.39	4.97	2.93	5.03	3.88	3.01
6	4.05	4.46	5	7.33	8.37	3.77	6.75	5.56	5.50
	1.31	1.23		2.17	2.42	1.20	1.76	1.69	0.969
3.13	2.29	2.47	3.02	3.16	2.10	2.33	2.96	2.16	2.43
14.6	12.6	9.30	16.7	13.4	12.20	17.7	20.6	11.67	15.1
62	45	41	50	57	57	51	66	78	81
	3.08	3.81		3.35	3.74	2.81	4.64	3.62	3.44
	5.39	4.15		8.37	7.77	7.66	5.65	6.91	6.66
	16.61	15.81		28.07	29.04	21.50	26.24	25.03	22.92
	3.06	2.94		3.73	3.56	3.70	3.48	3.39	3.40

Table 2 (1/2)

Rock Group	Group 1 (P-MORB)												Group 2a (alkaline)							
	MK483-basalt						MK485-basalt						MK491-ferrobasalt				MK479-basalt			
Sample-rock	2-1 r	2-10 c	3-2	4-4	5-3 r	5-8 c	2-2 c	2-6 r	1-2	4-2	5-7	6-2	1-3	3-1 c	3-7 r	5-3 c	6-1 c	6-4 r	3-3	4-3
Mineral-site Note																				
SiO ₂	50.50	49.84	50.94	48.59	49.94	48.85	50.00	50.08	49.64	49.02	49.77	50.00	50.27	49.33	48.76	49.80	49.86	47.62	49.26	49.99
TiO ₂	1.22	0.96	1.12	1.45	1.31	1.01	0.91	1.03	1.33	1.36	1.13	0.91	1.17	1.68	1.82	1.29	1.60	1.86	1.54	1.32
Al ₂ O ₃	2.53	2.40	2.70	2.51	2.53	2.73	1.44	1.74	2.63	2.83	3.06	1.90	2.98	3.30	3.19	2.93	3.46	3.63	3.82	3.47
Cr ₂ O ₃	0.07	0.05	0.13	0.04	0.00	0.25	0.00	0.05	0.02	0.04	0.16	0.15	0.38	0.27	0.19	0.40	0.41	0.28	0.26	0.36
FeO	9.02	11.67	9.01	12.28	11.35	8.42	13.82	11.58	11.57	10.78	9.49	8.72	6.46	8.56	8.51	6.77	7.79	8.60	6.98	6.49
MnO	0.12	0.31	0.14	0.21	0.28	0.23	0.30	0.21	0.25	0.19	0.19	0.15	0.06	0.16	0.13	0.19	0.12	0.15	0.07	0.16
MgO	15.34	14.08	15.58	14.44	14.95	15.89	14.26	15.29	14.41	14.83	15.51	16.32	16.46	14.51	14.94	16.09	15.27	14.04	15.88	16.22
CaO	20.89	19.96	20.86	19.42	20.32	21.11	19.26	19.48	20.22	20.36	20.29	20.69	21.58	21.40	21.79	21.32	21.39	21.02	21.34	22.05
Na ₂ O	0.28	0.46	0.33	0.40	0.36	0.38	0.35	0.34	0.39	0.37	0.32	0.30	0.37	0.44	0.43	0.41	0.50	0.50	0.33	0.35
K ₂ O	0.00	0.00	0.01	0.00	0.02	0.01	0.01	0.00	0.01	0.02	0.03	0.04	0.00	0.00	0.00	0.00	0.00	0.01	0.02	0.01
Total	99.95	99.73	100.81	99.33	101.07	98.88	100.36	99.80	100.46	99.80	99.94	99.17	99.71	99.65	99.76	99.18	100.42	97.70	99.50	100.43
<i>A.p.f.u.</i>																				
Si	1.873	1.868	1.871	1.830	1.842	1.821	1.873	1.870	1.846	1.828	1.844	1.859	1.849	1.837	1.811	1.845	1.834	1.809	1.821	1.828
Ti	0.034	0.027	0.031	0.041	0.036	0.028	0.026	0.029	0.037	0.038	0.031	0.025	0.032	0.047	0.051	0.036	0.044	0.053	0.043	0.036
Al	0.110	0.106	0.117	0.111	0.110	0.120	0.064	0.076	0.115	0.125	0.134	0.083	0.129	0.145	0.140	0.128	0.150	0.163	0.166	0.150
Cr	0.002	0.001	0.004	0.001	0.000	0.007	0.000	0.001	0.001	0.001	0.005	0.004	0.011	0.008	0.005	0.012	0.012	0.008	0.008	0.010
Fe ³⁺	0.095	0.136	0.100	0.175	0.159	0.202	0.165	0.150	0.145	0.170	0.135	0.166	0.124	0.112	0.163	0.128	0.117	0.141	0.124	0.138
Fe ²⁺	0.185	0.230	0.176	0.212	0.191	0.060	0.268	0.212	0.215	0.166	0.159	0.105	0.074	0.155	0.101	0.081	0.123	0.132	0.092	0.061
Mn	0.004	0.010	0.004	0.007	0.009	0.007	0.009	0.007	0.008	0.006	0.006	0.005	0.002	0.005	0.004	0.006	0.004	0.005	0.002	0.005
Mg	0.848	0.787	0.853	0.810	0.822	0.883	0.796	0.851	0.799	0.824	0.857	0.905	0.902	0.806	0.827	0.889	0.837	0.796	0.875	0.884
Ca	0.830	0.801	0.820	0.783	0.803	0.843	0.773	0.779	0.806	0.814	0.805	0.824	0.850	0.854	0.867	0.846	0.843	0.856	0.845	0.864
Na	0.020	0.034	0.023	0.029	0.026	0.027	0.025	0.025	0.028	0.027	0.023	0.021	0.026	0.032	0.031	0.029	0.036	0.037	0.024	0.025
K	0.000	0.000	0.000	0.000	0.001	0.000	0.001	0.000	0.000	0.001	0.001	0.002	0.000	0.000	0.000	0.000	0.000	0.000	0.001	0.000
Total	4.000	4.000	4.000	4.000	4.000	4.000	4.000	4.000	4.000	4.000	4.000	4.000	4.000	4.000	4.000	4.000	4.000	4.000	4.000	4.000
Al (IV)	0.110	0.106	0.117	0.111	0.110	0.120	0.064	0.076	0.115	0.125	0.134	0.083	0.129	0.145	0.140	0.128	0.150	0.163	0.166	0.150
Al (VI)	0.000	0.000	0.000	0.000	0.000	0.000	0.000	0.000	0.000	0.000	0.000	0.000	0.000	0.000	0.000	0.000	0.000	0.000	0.000	0.000
Wo (%)	42.0	40.3	41.6	39.0	40.1	41.8	38.1	38.6	40.4	40.7	40.7	40.8	43.0	43.6	43.6	42.9	43.1	43.6	43.1	43.8
En (%)	42.9	39.6	43.2	40.3	41.1	43.8	39.3	42.2	40.1	41.2	43.3	44.8	45.6	41.1	41.6	45.0	42.8	40.6	44.7	44.8
Fs (%)	9.6	13.7	10.1	17.6	16.0	20.2	16.6	15.1	14.6	17.1	13.6	16.7	12.5	11.3	16.4	12.9	11.7	14.2	12.4	13.8
Acm (%)	1.0	1.7	1.2	1.5	1.3	1.4	1.2	1.2	1.4	1.3	1.1	1.1	1.3	1.6	1.6	1.5	1.8	1.9	1.2	1.3
Mg#	0.75	0.68	0.76	0.68	0.70	0.77	0.65	0.70	0.69	0.71	0.74	0.77	0.82	0.75	0.76	0.81	0.78	0.74	0.80	0.82

Table 2 (2/2)

Rock Group	Group 2a (alkaline)		Group 2b (alkaline)																	
rock	MK479-basalt		MK859-ferrobasalt						MK855-basalt						MK910-meta basalt					
Mineral-site Note	5-3	12-3	1-10 c	1-14 r1 profile core-rim		1-7 r2	1-13 r3	4-2	5-1	1-5 c	1-12 r	2-6 c	2-10 r	4-4 r	4-9 c	1-3 c	1-4 ec	1-6 r	3-2	7-3
SiO ₂	50.01	48.03	50.11	44.68	49.14	46.32	46.20	45.83	48.33	45.80	45.55	45.78	49.73	48.15	47.66	46.06	45.40	48.72	49.02	
TiO ₂	1.01	2.11	1.26	3.69	2.03	2.44	2.87	3.47	1.99	3.30	2.97	3.49	1.29	2.21	1.95	2.48	3.05	1.49	1.43	
Al ₂ O ₃	2.66	4.39	2.88	7.08	3.75	5.59	5.89	6.17	4.13	5.72	5.92	5.65	2.92	5.13	4.38	5.70	6.39	3.54	3.30	
Cr ₂ O ₃	0.67	0.12	0.98	0.00	0.37	0.42	0.31	0.01	0.20	0.07	0.03	0.09	0.56	0.28	0.30	0.29	0.16	1.00	0.56	
FeO	5.75	7.78	4.25	7.12	5.83	6.49	6.72	7.57	5.87	8.08	6.81	8.18	4.79	6.19	6.02	7.30	7.46	5.18	5.74	
MnO	0.13	0.10	0.10	0.07	0.08	0.07	0.12	0.09	0.08	0.09	0.06	0.11	0.01	0.07	0.00	0.12	0.08	0.09	0.15	
MgO	16.68	14.91	16.02	12.52	15.09	13.67	13.52	12.75	14.60	13.16	13.55	13.60	16.02	13.61	14.89	14.05	13.71	15.17	15.03	
CaO	22.32	22.09	23.91	23.48	23.91	24.20	24.34	23.58	24.06	22.55	23.38	21.76	23.12	23.76	23.67	22.59	22.81	23.61	23.30	
Na ₂ O	0.37	0.34	0.32	0.56	0.38	0.39	0.44	0.46	0.36	0.66	0.60	0.39	0.36	0.41	0.28	0.46	0.47	0.38	0.55	
K ₂ O	0.01	0.00	0.00	0.00	0.00	0.00	0.00	0.00	0.00	0.00	0.00	0.02	0.00	0.00	0.01	0.00	0.01	0.02	0.02	
Total	99.62	99.87	99.82	99.20	100.57	99.57	100.40	99.95	99.61	99.43	98.85	99.07	98.79	99.81	99.15	99.04	99.53	99.20	99.10	
<i>A.p.f.u.</i>																				
Si	1.837	1.779	1.839	1.675	1.801	1.722	1.706	1.708	1.789	1.713	1.704	1.720	1.843	1.786	1.771	1.720	1.690	1.806	1.819	
Ti	0.028	0.059	0.035	0.104	0.056	0.068	0.080	0.097	0.055	0.093	0.084	0.099	0.036	0.062	0.055	0.070	0.085	0.042	0.040	
Al	0.115	0.191	0.125	0.313	0.162	0.245	0.256	0.271	0.180	0.252	0.261	0.250	0.127	0.224	0.192	0.251	0.280	0.155	0.144	
Cr	0.020	0.003	0.028	0.000	0.011	0.012	0.009	0.000	0.006	0.002	0.001	0.003	0.016	0.008	0.009	0.009	0.005	0.029	0.016	
Fe ³⁺	0.161	0.155	0.121	0.171	0.141	0.192	0.196	0.150	0.151	0.183	0.206	0.138	0.125	0.102	0.170	0.195	0.198	0.148	0.163	
Fe ²⁺	0.016	0.086	0.009	0.052	0.037	0.010	0.011	0.085	0.031	0.070	0.007	0.119	0.024	0.090	0.017	0.033	0.034	0.013	0.015	
Mn	0.004	0.003	0.003	0.002	0.002	0.002	0.004	0.003	0.002	0.003	0.002	0.004	0.000	0.002	0.000	0.004	0.003	0.003	0.005	
Mg	0.914	0.823	0.877	0.700	0.824	0.757	0.744	0.709	0.806	0.733	0.756	0.762	0.885	0.753	0.825	0.782	0.761	0.839	0.831	
Ca	0.879	0.876	0.940	0.943	0.939	0.964	0.963	0.942	0.954	0.903	0.937	0.876	0.918	0.944	0.942	0.904	0.910	0.938	0.926	
Na	0.026	0.024	0.022	0.041	0.027	0.028	0.032	0.033	0.026	0.048	0.043	0.028	0.026	0.029	0.020	0.034	0.034	0.027	0.039	
K	0.000	0.000	0.000	0.000	0.000	0.000	0.000	0.000	0.000	0.000	0.000	0.001	0.000	0.000	0.000	0.000	0.000	0.001	0.001	
Total	4.000	4.000	4.000	4.000	4.000	4.000	4.000	4.000	4.000	4.000	4.000	4.000	4.000	4.000	4.000	4.000	4.000	4.000	4.000	
Al (IV)	0.115	0.191	0.125	0.313	0.162	0.245	0.256	0.271	0.180	0.252	0.261	0.250	0.127	0.214	0.192	0.251	0.280	0.155	0.144	
Al (VI)	0.000	0.000	0.000	0.000	0.000	0.000	0.000	0.000	0.000	0.000	0.000	0.000	0.000	0.010	0.000	0.000	0.000	0.000	0.000	
Wo (%)	44.0	44.6	47.7	49.5	47.7	49.4	49.5	49.1	48.5	46.6	48.1	45.6	46.4	49.2	47.7	46.4	47.0	47.7	46.9	
En (%)	45.8	41.9	44.5	36.7	41.9	38.8	38.2	36.9	41.0	37.9	38.8	39.6	44.8	39.2	41.8	40.2	39.3	42.7	42.1	
Fs (%)	16.1	15.5	12.1	17.1	14.1	19.2	19.6	15.1	15.1	18.4	20.6	13.9	12.5	10.2	17.0	19.5	19.8	14.8	16.3	
Acm (%)	1.3	1.2	1.1	2.1	1.4	1.5	1.6	1.7	1.3	2.5	2.2	1.5	1.3	1.5	1.0	1.7	1.7	1.4	2.0	
Mg#	0.84	0.77	0.87	0.76	0.82	0.79	0.78	0.75	0.82	0.74	0.78	0.75	0.86	0.80	0.82	0.77	0.77	0.84	0.82	



Click here to access/download

**Supplementary material/Appendix (Files for online
publication only)**

Fig_S1.jpg



Click here to access/download

**Supplementary material/Appendix (Files for online
publication only)**

Fig_S2.jpg



Click here to access/download

**Supplementary material/Appendix (Files for online
publication only)**

Supplementary_Fig_S3.pdf



Click here to access/download

**Supplementary material/Appendix (Files for online
publication only)**

Supplementary_Table_S01.xls



Click here to access/download

**Supplementary material/Appendix (Files for online
publication only)**

Supplementary_Table_S02.xls

Declaration of interests

The authors declare that they have no known competing financial interests or personal relationships that could have appeared to influence the work reported in this paper.

The authors declare the following financial interests/personal relationships which may be considered as potential competing interests:

On behalf of the co-authors
Emilio Saccani